CONTINUOUS BLOOD GLUCOSE MONITORING USING MACHINE LEARNING TECHNIQUES

A Thesis submitted to Gujarat Technological University

for the Award of

Doctor of Philosophy

in

Electronics and Communication Engineering

by

LAD KETAN KHANDUBHAI

[209999915002]

under supervision of

Dr. Maulin Mahesh Joshi

GUJARAT TECHNOLOGICAL UNIVERSITY
AHMEDABAD
[August - 2026]

DECLARATION

I declare that the thesis entitled **CONTINUOUS BLOOD GLUCOSE MONITORING USING MACHINE LEARNING TECHNIQUES** submitted by me for the degree of Doctor of Philosophy is the record of research work carried out by me during the period from **May 2021 to February 2026** under the supervision of **Dr. Maulin Mahesh Joshi** and this has not formed the basis for the award of any degree, diploma, associateship, fellowship, titles in this or any other University or other institution of higher learning.

I further declare that the material obtained from other sources has been duly acknowledged in the thesis. I shall be solely responsible for any plagiarism or other irregularities, if noticed in the thesis.

Signature of Research Scholar:  Date: 24/08/2026

Name of Research Scholar: **LAD KETAN KHANDUBHAI**

Place: **Ahmedabad**

CERTIFICATE

I certify that the work incorporated in the thesis **CONTINUOUS BLOOD GLUCOSE MONITORING USING MACHINE LEARNING TECHNIQUES** submitted by **LAD KETAN KHANDUBHAI** was carried out by the candidate under my supervision/guidance. To the best of my knowledge: (i) the candidate has not submitted the same research work to any other institution for any degree/diploma, Associateship, Fellowship or other similar titles (ii) the thesis submitted is a record of original research work done by the Research Scholar during the period of study under my supervision, and (iii) the thesis represents independent research work on the part of the Research Scholar.

Signature of the Research Supervisor: Date: 24/08/2026.

Name of Supervisor: **Dr. Maulin Mahesh Joshi**

Place: GTU

Course-work Completion Certificate

This is to certify that **LAD KETAN KHANDUBHAI** enrolment no. **209999915002** is a PhD scholar enrolled for PhD program in the branch **Electronics and Communication** of Gujarat Technological University, Ahmedabad.

(Please tick the relevant option(s))

☐ He has been exempted from the course-work (successfully completed during M. Phil Course)

☐ He has been exempted from Research Methodology Course only (successfully completed during M. Phil Course)

☑ He has successfully completed the PhD course work for the partial requirement for the award of PhD Degree. His performance in the course work is as follows-

Grade Obtained in Research Methodology (PHD2001)	Grade Obtained in Research and Publication Ethics (PHD2002)	Grade Obtained in Self-Study Course / Contact Program (PHD2003)
BC	AB	AA

Supervisor's Sign

(Dr. Maulin Mahesh Joshi)

Originality Report Certificate

It is certified that PhD Thesis titled **CONTINUOUS BLOOD GLUCOSE MONITORING USING MACHINE LEARNING TECHNIQUES** submitted by **LAD KETAN KHANDUBHAI** has been examined by us. We undertake the following:

a. Thesis has significant new work/knowledge as compared already published or are under consideration to be published elsewhere. No sentence, equation, diagram, table, paragraph or section has been copied verbatim from previous work unless it is placed under quotation marks and duly referenced.

b. The work presented is original and own work of the author (i.e. there is no plagiarism). No ideas, processes, results or words of others have been presented as Author own work.

c. There is no fabrication of data or results which have been compiled/analyzed.

d. There is no falsification by manipulating research materials, equipment or processes, or changing or omitting data or results such that the research is not accurately represented in the research record.

e. The thesis has been checked using https://www.turnitin.com/ (copy of originality report attached) and found within limits as per GTU Plagiarism Policy and instructions issued from time to time (i.e. permitted similarity index <=10%).

Signature of the Research Scholar: ..... Date: 24/08/2026

Name of the Research Scholar: **LAD KETAN KHANDUBHAI**

Place: **Ahmedabad**

Signature of the Research Supervisor: ..... Date: 24/08/2026

Name of the Research Supervisor: **Dr. Maulin Mahesh Joshi**

Place: **Surat**

Copy of Originality Report

Ketan Lad

Continuous Blood Glucose Monitoring using Machine Learning Techniques

Quick Submit

Quick Submit

Gujarat Technological University

Document Details

Submission ID
trn:oid:::1:3612332869

Submission Date
Jul 16, 2026, 10:31 PM GMT+5:30

Download Date
Jul 16, 2026, 10:44 PM GMT+5:30

File Name
209999915002_Ketan_Lad_thesis.docx

File Size
5.3 MB

120 Pages

29,251 Words

160,976 Characters

turnitin Page 1 of 134 - Cover Page Submission ID trn:oid:::1:3612332869

Copy of Originality Report

9% Overall Similarity

The combined total of all matches, including overlapping sources, for each database.

Exclusions

- 3 Excluded Sources
- 1 Excluded Match

Match Groups

- 290 Not Cited or Quoted 8%
  Matches with neither in-text citation nor quotation marks
- 2 Missing Quotations 0%
  Matches that are still very similar to source material
- 4 Missing Citation 0%
  Matches that have quotation marks, but no in-text citation
- 0 Cited and Quoted 0%
  Matches with in-text citation present, but no quotation marks

Top Sources

- 4% Internet sources
- 7% Publications
- 1% Submitted works (Student Papers)

Integrity Flags

1 Integrity Flag for Review

- Hidden Text
  46 suspect characters on 1 page
  Text is altered to blend into the white background of the document.

Our system's algorithms look deeply at a document for any inconsistencies that would set it apart from a normal submission. If we notice something strange, we flag it for you to review.

A Flag is not necessarily an indicator of a problem. However, we'd recommend you focus your attention there for further review.

PhD Thesis Non-Exclusive License to

GUJARAT TECHNOLOGICAL UNIVERSITY

In consideration of being a Research Scholar at Gujarat Technological University, and in the interests of the facilitation of research at the University and elsewhere, **I, LAD KETAN KHANDUBHAI** having **Enrolment No. 209999915002**, hereby grant a nonexclusive, royalty free and perpetual license to the University on the following terms:

a. The University is permitted to archive, reproduce and distribute my thesis, in whole or in part, and/or my abstract, in whole or in part (referred to collectively as the "Work") anywhere in the world, for non-commercial purposes, in all forms of media;
b. The University is permitted to authorize, sub-lease, sub-contract or procure any of the acts mentioned in paragraph (a);
c. The University is authorized to submit the Work at any National / International Library, under the authority of their "Thesis Non-Exclusive License";
d. The Universal Copyright Notice (©) shall appear on all copies made under the authority of this license;
e. I undertake to submit my thesis, through my university, to any Library and Archives. Any abstract submitted with the thesis will be considered to form part of the thesis.
f. I represent that my thesis is my original work, does not infringe any rights of others, including privacy rights, and that I have the right to make the grant conferred by this non-exclusive license.
g. If third party copyrighted material was included in my thesis for which, under the terms of the Copyright Act, written permission from the copyright owners is required, I have obtained such permission from the copyright owners to do the acts mentioned in paragraph (a) above for the full term of copyright protection.
h. I understand that the responsibility for the matter as mentioned in the paragraph (g) rests with the authors / me solely. In no case shall GTU have any liability for any acts / omissions / errors / copyright infringement from the publication of the said thesis or otherwise.
i. I retain copyright ownership and moral rights in my thesis, and may deal with the copyright in my thesis, in any way consistent with rights granted by me to my university in this non-exclusive license.

j. GTU logo shall not be used /printed in the book (in any manner whatsoever) being published or any promotional or marketing materials or any such similar documents.

k. The following statement shall be included appropriately and displayed prominently in the book or any material being published anywhere: "The content of the published work is part of the thesis submitted in partial fulfilment for the award of the degree of Ph.D. in **Electronics and Communication Engineering** of the Gujarat Technological University".

l. I further promise to inform any person to whom I may hereafter assign or license my copyright in my thesis of the rights granted by me to my university in this nonexclusive license. I shall keep GTU indemnified from any and all claims from the Publisher(s) or any third parties at all times resulting or arising from the publishing or use or intended use of the book / such similar document or its contents.

m. I am aware of and agree to accept the conditions and regulations of Ph.D. including all policy matters related to authorship and plagiarism.

Date: 24/08/2026

Place: **Ahmedabad**

Signature of the Research Scholar

Name of Research Scholar: **LAD KETAN KHANDUBHAI**

Recommended of the Research Supervisor: .....Recommended.....

Signature of the Research Supervisor

Thesis Approval Form

The viva-voce of the PhD Thesis submitted by **LAD KETAN KHANDUBHAI** (Enrollment No. 209999915002) entitled **CONTINUOUS BLOOD GLUCOSE MONITORING USING MACHINE LEARNING TECHNIQUES** was conducted on **24/08/2026, Monday** at Gujarat Technological University.

(Please tick any one of the following option)

☑ The performance of the candidate was satisfactory. We recommend that he be awarded the PhD degree.

☐ Any further modifications in research work recommended by the panel after 3 months from the date of first viva-voce upon request of the Supervisor or request of Independent Research Scholar after which viva-voce can be re-conducted by the same panel again.

(Briefly specify the modifications suggested by the panel)

☐ The performance of the candidate was unsatisfactory. We recommend that he should not be awarded the PhD degree.

(The panel must give justifications for rejecting the research work)

24/08/2026.

(Dr. Maulin Mahesh Joshi)
Name and Signature of Supervisor

24/8/2026

(Dr. Jignesh Sarvaiya)
External Examiner-1

(Dr. M. Ravikumar)
External Examiner-2

Abstract

More than 500 million individuals in the world have diabetes today, with an estimated number of 783 million by 2045. Monitoring of Blood Glucose (BG) is an essential activity, particularly in individuals with Type 1 diabetes (T1D), who need exogenous insulin to manage the condition. Frequent BG monitoring is possible with Continuous blood Glucose Monitoring; however, it relies on invasive blood sampling, which can be painful and prone to infection. The existing CGM systems use only the current BG level to compute insulin bolus doses, without accounting for variation in carbohydrate intake during meals. This condition, in most cases, causes T1D patients to have hypoglycaemic and hyperglycaemic episodes. Otherwise, uncontrolled elevated BG leads to severe complications, including eye disease, neuropathy, nephropathy, and cardiovascular disease. In general, good glycaemic control in the management of diabetes has been a great challenge. To address these issues, this study focuses on developing a non-invasive CGM device that measures BG, predicts future BG levels, and calculates insulin boluses based on these predictions to improve glycaemic control.

The proposed Continuous Blood Glucose Monitoring system involves a non-invasive, single-sensor device operating at 940 nm to obtain physiological signals and produce a structured dataset. The dataset is used with the Shapley additive explanations method to identify key features in the estimation of blood glucose. A distributed architecture provides lightweight machine learning-based continuous estimation of BG levels, and a forecasting architecture predicts future BG levels with a 60-minute horizon. Bolus insulin doses are calculated using the forecasted BG, carbohydrate intake, and subject-specific characteristics. Intermittent insulin boluses are tested across 10 virtual adult cohorts in the UVA/Padova T1D simulator under different meal and insulin conditions.

The analysis indicates that the proposed system estimates BG levels with a mean absolute difference (MAD) of 1.79 mg/dL and a RMSE of 6.08 mg/dL. In CGM, a deep learning-based hybrid architecture is also proposed for BG forecasting. This architecture demonstrates improved performance, achieving RMSE values of 3.42, 6.45, and 17.73 mg/dL for 15-, 30-, and 60-minute prediction horizons (PHs), respectively, and 12.57, 20.72, and 34.41 mg/dL for real cohorts. Additionally, the Mean Absolute Error (MAE) for

15-, 30-, and 60-minute PHs is 2.11, 4.47, and 11.78 mg/dL for virtual cohorts, respectively, and 7.9, 14.13, and 25.5 mg/dL for real cohorts. The proposed approach improves glycaemic stability, with 98.86% of time in the euglycemic range (70-180 mg/dL), and reduces the risk of hyperglycaemia and hypoglycaemia, as indicated by mean values of the High BG Index (HBGI) at 0.46, Low BG Index (LBGI) at 1.27, and BG Risk Index (BGRI) at 7.49. Control-Variability Grid Analysis (CVGA) confirms the clinical applicability, showing that all virtual patients' BG levels are within zones A and B.

The proposed Continuous Blood Glucose Monitoring system offers a convenient and non-invasive solution for managing T1D. This system enhances glycaemic control by using forecasting to make insulin dosing decisions. It holds significant potential for future use in intelligent, personalized diabetes care systems.

Keywords: Machine learning, Continuous glucose monitoring, Blood Glucose, non-invasive measurement, Multiple daily injection, Insulin bolus, Glycaemic control

Acknowledgement

This thesis would have been impossible without the support of many people. My sincere gratitude to them for their invaluable support; they deserve much more than this short note of appreciation. I want to thank Almighty God for giving me the strength and passion to do research.

I want to express my appreciation to my supervisor, **Dr Maulin Mahesh Joshi**, for his valuable guidance and encouragement throughout the research process. Thanks to his extensive technical support, I completed my research on time. Also, I would like to express my gratitude to **Dr Saurin Shah** and **Dr Hitesh Shah,** as my thesis Doctoral Progress Committee Members. Their constructive suggestions improved the thesis in many respects.

I also acknowledge the Honourable Vice Chancellor, Registrar, Controller of Examinations, Dean, PhD Section, and all staff members of the PhD Section of Gujarat Technological University (GTU) for their assistance and support. The authors would like to express their sincere gratitude to **Dr Anish Diwanji** for granting permission to conduct experimental work in his pathological laboratory, Shreenath Clinical Laboratory, Valsad. His support enabled us to deploy our non-invasive device and collect blood glucose (BG) readings, which were essential for this study.

I express my sincere gratitude to **Svaarogyam Medical Pvt Ltd**. and **Dr Amit Joshi** for providing a single-sensor, non-invasive device for BG data collection. I also thankful to **Dr Amit Joshi** for providing access to the UVA/Padova T1D Mellitus simulator for my research.

I am also thankful to **Dr Anita Bhatt and Dr Suresh L. Bharvad** for providing the technical guidance during my research. I thank all the staff members of L. D. College of Engineering, Ahmedabad, for their kind help and cooperation throughout my studies. Finally, I pay my deepest respects and love to **my parents**, my wife, **Bela Lad**, my daughter, **Yaami,** and my son**, Dhruvin**. I want to express my highest appreciation for their support and cooperation.

This thesis is dedicated to all good wishers who love me and help me reach an important stage in life. I will never let them down and wish them all the best in the future. As it is a prolonged journey, I may have forgotten a few names to consider, but they remain a core

part of this mammoth task, and I seek forgiveness for the same and offer my kind respects to every one of them. I thanks to all those who have supported and guided me throughout this journey.

Thank you all from the bottom of my heart.

LAD KETAN KHANDUBHAI
209999915002
Research Scholar, Gujarat Technological University

Table of Contents

List of Abbreviations

ADC	: Analog-to-Digital Converter
AHCL	: Advanced Hybrid CL
AI	: Artificial Intelligence
ANN	: Artificial Neural Network
AP	: Artificial Pancreas
ARIMA	: Autoregressive Integrated Moving Average
BG	: Blood Glucose
BGRI	: Blood Glucose Risk Index
CAI	: Current Acting Insulin
CEGA	: Clarke Error Grid analysis
CF	: Correction Factor
CGM	: Continuous Glucose Monitoring
CL	: Closed-Loop
CNN	: Convolutional Neural Network
CR	: Insulin-to-carbohydrate ratio
CRNN	: Convolutional Recurrent Neural Network
CVGA	: Control-Variability Grid Analysis
DCNN	: Dilated Convolutional Neural Network
DCRNet	: Deep Convolutional Recurrent Neural Network
DL	: Deep Learning
DT	: Decision Tree
FC	: Fully Connected
FCN	: Fully Connected Network
FDA	: Food and Drug Administration
FN	: False Negative
FP	: False Positive
GPU	: Graphics Processing Unit
GRU	: Gated Recurrent Unit
GUI	: Graphical User Interface

HBGI	: High Blood Glucose Index
IDF	: International Diabetes Federation
iGLU	: Intelligent Glucometer
IIB	: Intermittent Insulin Bolus
IoMT	: Internet of Medical Things
IQR	: Inter-quartile Range
IR	: Infrared
k-NN	: k-nearest neighbour
LBGI	: Low Blood Glucose Index
LIME	: Local Interpretable Model-agnostic Explanations
LLM	: Large Language Model
LSTM	: Long Short-Term Memory
MAD	: Mean Absolute Deviation
MAE	: Mean Absolute Error
mARD	: Mean Absolute Relative Deviation
MDI	: Multiple Daily Injection
ML	: Machine Learning
MLR	: Multi Linear Regression
MSE	: Mean Squared Error
NAS	: Neural Architecture Search
NIR	: Near-Infrared
PH	: Prediction Horizon
ReLU	: Rectified Linear Unit
RF	: Random Forest
RMSE	: Root Mean Square Error
RNNs	: Recurrent Neural Networks
SD	: Standard Deviation
SHAP	: Shapley Additive Explanations
SVM	: Support vector machine
SVR	: Support Vector Regression
T1D	: Type 1 Diabetes
T1DM	: T1D Mellitus
T2D	: Type 2 Diabetes

TAR	: Time Above Range
TBR	: Time Below Range
TIR	: Time in Range
TN	: True Negative
TP	: True Positive
UVA/Padova T1DM	: UVA/Padova T1D Mellitus
XAI	: Explainable AI

List of Symbols

k	Number of neighbours
d	Euclidean distance
$\boldsymbol{x}$	Vector of input feature
b_0	Bias
W	Weight vector
y_i	i^{th} data point target value
$\bar{y}$	Target values' mean
p_i	the i^{th} class probability
C	Regularization parameter
$\hat{y}$	Predicted output
f	Size of the kernel
g	Gram
w	Window size
$\emptyset(\cdot)$	ReLU activation function
R	The effective receptive field of each layer
r	Dilation rate
σ	Sigmoid
$\psi\,(\cdot)$	Linear activation function
Θ	Model parameters
g_t	Gradient at iteration t
η	Learning rate
CHO	Meal's carbohydrate content
G_T	Target BG level
G_t	Current BG level
BI_S	Bolus insulin

List of Figures

List of Tables

List of Appendices

Chapter 1
Introduction

1.1 Continuous Blood Glucose monitoring

Diabetes is a long-term disorder that occurs when the body fails to balance Blood Glucose (BG) levels. The pancreas secretes the hormone insulin, which is vital for regulating BG levels, which cells use as a source of energy. Abnormalities in insulin secretion create diabetes. Type 1 Diabetes (T1D) and Type 2 Diabetes (T2D) are the two broad types of diabetes. In T1D, the immune system of individuals attacks and destroys the insulin-producing cells of the pancreas. Consequently, such individuals generate low or no insulin. These people have to take insulin regularly to survive. Conversely, the pancreas of people with T2D does not produce sufficient insulin to maintain BG within the euglycemic range (70-180 mg/dL). T2D is more prevalent and usually develops in adulthood. T1D patients have serious difficulties, as they should inject insulin several times or use insulin pumps to measure their blood sugar level regularly, and sometimes consult medical specialists. Diabetes is a significant burden on the world and is expected to continue increasing over the next few decades [1].

Continuous Blood Glucose Monitoring aids in diabetes management by continuously tracking BG levels in real time throughout both day and night [2]. It is particularly useful for people with diabetes who use several insulin injections or insulin pumps daily, including people with T1D. It may also be beneficial to a few individuals with T2D. In CGM, BG levels can be measured by invasive or non-invasive methods. The invasive technique involves penetrating the skin or fingertip to test BG levels. The fact that the process of using CGM is uncomfortable and inconvenient is due to the necessity to conduct several BG readings daily. A more viable solution is provided by CGM sensors that non-invasively measure BG levels without puncturing the fingertips [3].

1.2 Motivation

The increasing burden of diabetes worldwide, together with the need for continuous and accurate BG monitoring, underscores the imperative to develop a CGM system. Even though CGM technologies have greatly enhanced diabetes management through real-time

glucose data, several challenges limit their utility and use among a broad audience. The existing systems are often associated with sensor noise, calibration requirements, low sensitivity to rapid glucose variations, and invasive or semi-invasive sensing methods, which may lead to discomfort and poor patient compliance. Also, most CGM-based decision-making methods currently in use are reactive and rely on current glucose levels rather than predictive insights. They therefore cannot effectively prevent impending hypoglycaemic or hyperglycaemic episodes. Non-invasive CGM devices have not yet reached clinical-level accuracy, despite their potential. These limitations, as well as the necessity to provide inexpensive, easy-to-use, and very accurate monitoring systems, drive further development of CGM systems. In particular, there is an urgent need to develop an advanced, credible, and predictive CGM system that enables proactive diabetes treatment, enhances patient comfort, and enables real-time monitoring.

1.3 Definition of the Problem

Although there have been tremendous technological improvements in diabetes management, the lack of reliable, comfortable, and smart CGM systems that are non-invasive and enable proactive glucose control remains a problem. CGM systems mostly use an invasive approach to estimate glucose levels and compute insulin doses based on those levels. It is a method that offers a few benefits for predicting future glucose changes, but it often makes insulin dosage decisions reactive. This results in delayed interventions, high glucose variability, and an elevated probability of hypo- and hyperglycaemic events. These restrictions reflect the necessity of a holistic CGM model that incorporates non-invasive, precise glucose measurements, short-term glucose projections, and optimal insulin-dose calculations to facilitate effective, timely control of glycaemic levels.

1.4 Objective and Scope of Work

1.4.1 Objectives

To effectively manage diabetes in individuals with T1D requires precise and continuous monitoring of BG levels to diminish the risk of severe hyperglycaemia and hypoglycaemia events. However, the effectiveness of existing CGMs is limited because they rely on an invasive approach for BG estimation and calculate insulin boluses based on current BG values. This limitation leads to decreasing patient compliance and therapeutic effectiveness. This research aims:

- To formulate a model for BG estimation using Machine Learning (ML) techniques that utilizes a non-invasive approach, is computationally efficient, and accurately measures BG levels in real time.
- To find the key input parameters the ML model uses to estimate BG levels.
- To develop a computationally efficient multivariate forecasting model that effectively forecasts the BG level with higher accuracy in real time.
- The research aims to accomplish subsequent precise objectives by developing this predictive capability:
    - Compute the optimal insulin bolus dosage using the developed system for T1D individuals.
    - Investigate a CGM system that proactively helps to design bolus insulin therapy to improve glycaemic control throughout the day.

1.4.2 Scope of work

The research aims to develop a new ML-based CGM and control system that effectively and non-invasively measures BG levels. The research is based on the development of a structured dataset from a single-sensor, non-invasive device operating at 940 nm. Another important aspect of the research is to identify valuable features for estimating BG. It also involves designing a computationally efficient, lightweight, and distributed ML model to estimate continuous BG levels.

Another part of the research will be the development of a short-term BG forecasting model that predicts glucose levels up to 60 minutes in advance. This model will aid in predicting future glucose trends. Using these predicted glucose values, a model for calculating insulin bolus doses is adopted to improve glucose management during meals under intermittent insulin therapy. Lastly, the proposed method is evaluated using various metrics to assess its efficiency in improving glycaemic control and minimizing glucose variability. The research does not consider fully automated, Closed-Loop (CL) insulin delivery devices and focuses on intermittent insulin therapy.

1.5 Original Contribution of the Thesis

- This thesis proposes a non-invasive CGM system that incorporates machine-learning-based BG measurement, BG forecasting, and intermittent insulin bolus

(IIB) calculation to improve glycaemic control relative to daily carbohydrate (CHO) variation across meals.

- This thesis introduces a non-invasive single-sensor instrument for continuous BG level measurement. To test the efficiency of this continuous BG measurement device, a new database was developed for this research using data from 784 individuals. Additionally, Shapley additive explanations are used to extract 13 significant features from the collected data, thereby enhancing BG estimation performance.
- This thesis presents a lightweight two-level distributed system based on a random forest model that calculates BG levels with higher accuracy. The proposed architecture achieves better performance in estimating BG levels than the state-of-the-art, with a Root Mean Square Error (RMSE) of 6.08 mg/dL, a Mean Absolute Deviation (MAD) of 1.79 mg/dL, and a mean Absolute Relative Deviation (mARD) of 1.5%. Also, the effectiveness of this architecture is proven by Clarke Error Grid Analysis (CEGA).
- In this thesis, a hybrid architecture, DCRNet, is proposed to forecast BG, combining a Dilated Convolutional Neural Network (DCNN) and a Long Short-Term Memory (LSTM) network. The DCNN is advantageous because it has a larger receptive field, which can improve its ability to capture multidimensional information in time-series data. At the same time, the LSTM efficiently captures long-term temporal relationships in multivariate time-series data. The effectiveness of the proposed hybrid architecture is assessed using a virtual dataset generated from 11 virtual T1D subjects in the UVA/Padova T1D Mellitus (UVA/Padova T1DM) simulator. This architecture uses time-series BG data and carbohydrate intake from 1,344 meal scenarios created by the UVA/Padova T1DM simulator. The effectiveness of the proposed architecture is also evaluated on the OhioT1DM dataset, which contains time-series data from 12 real subjects.
- In this thesis, a proposed IIB therapy utilizes forecasted glucose levels generated by a predictive model, replacing the conventional practice of using current BG values to calculate bolus insulin doses.
- The proposed IIB therapy surpasses the conventional Multiple Daily Injection (MDI) system and the Artificial Pancreas (AP) system, achieving a remarkable 99% of time with BG levels within 70-180 mg/dL across 10 virtual adult cohorts. This therapy also reduces the incidence of both hyperglycaemia and hypoglycaemia,

while enhancing overall glycaemic control throughout the day. The proposed therapy is safe and improves BG control, as the BG levels of all virtual patients fall within Zones A and B on the Control-Variability Grid Analysis (CVGA).

- The proposed CGM system offers optimal glycaemic control with just three insulin doses per day. This approach gives patients more freedom from being tethered to external devices or relying on an insulin pump, compared to traditional automated insulin delivery systems.

1.6 Thesis Organization

This thesis is divided into chapters, each discussing a detail of CGM, prediction, and insulin delivery using ML methods. The thesis is presented in the following way:

Chapter 2 reviews the existing literature on CGM and prediction. Recent CGM systems and a range of invasive and non-invasive methods for measuring BG are discussed. Explainable AI (XAI) techniques for feature importance analysis, hybrid forecasting models, and ML and Deep Learning (DL) approaches for glucose prediction are also discussed in the chapter.

Chapter 3 describes how a dataset can be generated for estimating BG levels using non-invasive sensors. It describes the use of a device containing three non-invasive sensors and a single-sensor data-gathering device. Moreover, the chapter describes the data preprocessing to remove outliers from the collected data.

Chapter 4 describes feature extraction and XAI methods for determining the most important features affecting BG prediction. It introduces a machine learning-based approach to BG measurement with a lightweight, distributed architecture that aims to improve robustness through data augmentation/normalization. Accuracy, F1-score, precision, recall, RMSE, mARD, and MAD are all utilized as performance metrics. It also includes CEGA and a comparison with current non-invasive methods.

Chapter 5 focuses on a DL method for predicting BG levels and details preprocessing steps such as segmentation and normalization. It discusses the datasets used, including clinical and in silico data, and introduces the DCRNet architecture, which integrates an LSTM network with a DCNN network. The model is tested using standard performance measures,

compared with state-of-the-art methods, and then evaluated further using statistical measures.

Chapter 6 describes an IIB therapy based on forecasting, intended to enhance glycaemic control in people with T1D. The proposed IIB therapy is evaluated using several simulated scenarios, along with an explanation of the mechanism for calculating an insulin bolus based on forecasted BG levels. Additionally, a Graphical User Interface (GUI) for calculating meal-based insulin boluses is provided. Several evaluation metrics, including Time in Range (TIR), Time Above Range (TAR), Time Below Range (TBR), High BG Index (HBGI), Low BG Index (LBGI), BG Risk Index (BGRI), and CVGA, are used to assess the efficacy of the proposed IIB therapy.

Chapter 7 presents the architecture and operation of the proposed CGM system. It describes the general structure, data-collection procedure, and system components used for glucose monitoring, prediction, and BG control. The advantages and usefulness of the proposed CGM system are also discussed in comparison with existing systems.

Chapter 8 concludes the major discoveries and contributions of the research presented in the thesis. It highlights the effectiveness of the proposed approaches for glucose monitoring, forecasting, and insulin therapy. The chapter concludes by discussing potential future research directions to improve the proposed CGM system.

Chapter 2
Literature Review

2.1 Introduction

Diabetes is a persistent metabolic illness that causes high BG levels, which may result from insufficient or absent insulin production. Figure 2.1 shows the global diabetes indices produced by the International Diabetes Federation (IDF).

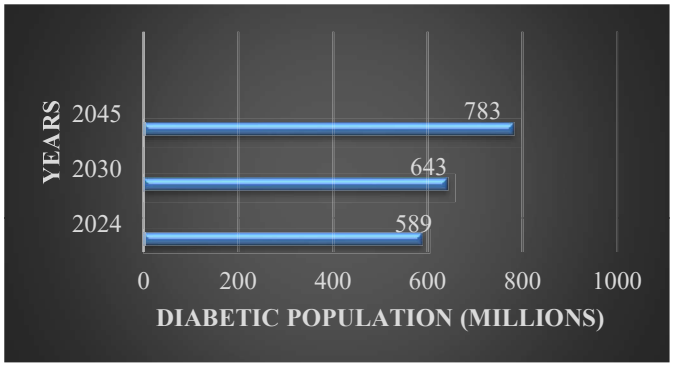

Figure 2.1: Global diabetes indices forecasted by IDF [1]

IDF estimates that 589 million people worldwide currently have diabetes. By 2030, there will be 643 million people with diabetes worldwide, and 783 million by 2045 [1]. In recent decades, diabetes cases have significantly increased worldwide, and it has become a significant global health issue. BG levels should be appropriately checked in order to prevent severe outcomes, such as hypoglycaemia, hyperglycaemia, cardiovascular diseases, and renal failure. BG has traditionally been measured with self-monitoring devices that involve finger pricks. However, these techniques can only provide discrete data and cannot show continuous variation in glucose levels.

A CGM system makes a significant contribution to the effective management of diabetes [2]. CGM systems provide real-time glucose monitoring, making it easier to decide on insulin therapy by continuously measuring BG levels in interstitial fluid. With increasing access to CGM data, ML algorithms have been widely used to analyse glucose trends and forecast future BG levels.

The chapter provides an in-depth literature review of BG measurement techniques, ML methods for estimating BG levels, BG forecasting, XAI-based feature extraction, and current BG control methods. The shortcomings of existing approaches and the research gaps that drive the current study are also discussed in the chapter.

2.2 Blood Glucose Monitoring

Maintaining the BG levels within the recommended range is essential to getting rid of the long-term effects associated with diabetes. BG monitoring is also imperative for controlling diabetes, allowing patients to adjust insulin dosage, food intake, and physical exercise. Traditional BG monitoring involves glucometers that measure intermittent fingerstick readings. These methods cannot record dynamic changes in BG levels throughout the day. For this reason, hypoglycaemic or hyperglycaemic episodes may be missed between readings. CGM systems overcome these disadvantages and enhance the understanding of glucose patterns and fluctuations by providing frequent glucose levels.

2.3 BG measurement methods

Individuals can effectively manage diabetes by regularly monitoring their BG levels. Depending on the method used to measure glucose, BG estimation technology can be characterized into three types: invasive, minimally invasive, and non-invasive. Each of these methods has its own advantages and disadvantages in terms of cost, convenience, and accuracy.

2.3.1 Invasive BG Measurement methods

Invasive glucose-monitoring methods use blood samples to measure BG. For measuring glucose, these techniques usually require puncturing the skin to draw a tiny amount of blood. Self-Monitoring of BG with portable glucometers is the most popular invasive technique. Figure 2.2 illustrates invasive glucose measurement using a glucometer.

Figure 2.2: Invasive glucose measurement using glucometer [2]

Invasive methods have several drawbacks despite yielding consistent results:

- Repeated finger pricks cause pain and suffering
- Infection risk
- A limited number of measurements daily
- Inability to record continuous fluctuations in glucose

These restrictions prevent invasive monitoring techniques from providing comprehensive data on glucose trends throughout the day.

2.3.2 Minimally Invasive BG Measurement methods

Minimally invasive techniques involve implanting small sensors underneath the skin to estimate BG levels. Figure 2.3 illustrates a minimally invasive glucose measurement technique.

Figure 2.3: Minimally invasive glucose measurement [4]

The sensor sends data to a receiver or a smartphone app while continuously measuring BG levels. These technologies enable identification of glucose trends and fluctuations and provide glucose readings every few minutes. Devices from Dexcom and Abbott Laboratories are among the most popular CGM systems available [4].

Minimally invasive monitoring offers several advantages, including:

- Continuous monitoring of glucose levels
- The ability to recognize patterns and tendencies in BG levels
- Early alerts for high and low blood sugar levels
- Improved management and control of diabetes

However, CGM devices also have some disadvantages, such as sensor noise, the need for calibration, and physiological delays between BG levels and interstitial glucose measurements.

2.3.3 Non-Invasive BG Measurement methods

Non-invasive BG monitoring techniques estimate glucose levels without penetrating the skin or drawing blood. These technologies are the subject of active research because they promise painless, convenient glucose monitoring. Various sensing approaches have been proposed, including biofluid analysis, physiological signal measurement, and optical sensing technologies.

2.3.3.1 Bio-Fluid Based methods

Biological fluids, such as saliva, are one approach to non-invasive glucose monitoring. The glucose content in saliva samples can be detected using optical biosensors and electrochemical sensors [5], [6], [7]. These sensors measure BG levels by monitoring glucose metabolism and detecting its products. Though saliva-based sensing does not involve a blood sample, the correlation between saliva glucose concentration and BG levels may vary among individuals. Variations in saliva composition, hydration levels, and environmental conditions may impact the accuracy of BG estimation.

2.3.3.2 Physiological Signal-Based methods

Non-invasive glucose monitoring may include measuring physiological parameters and electrophysiological features of tissues. Methods such as impedance spectroscopy measure changes in tissue electrical impedance to estimate BG levels [8], [9]. On the same note, terahertz time-domain spectroscopy measures the interaction of electromagnetic waves with biological tissues to determine glucose concentration [10]. Advanced sensing systems have been designed to enhance glucose estimation the accuracy by incorporating physiological parameters, such as skin temperature, pressure sensors, and radio-frequency sensors [11].

To maintain continuous patient monitoring, these multivariate sensing systems are typically integrated with intelligent healthcare systems and Internet of Medical Things (IoMT) platforms [12], [13]. Besides, a wearable-based methodology has been investigated for non-invasive glucose estimation using signal processing and ML methods [14]. It proposes a time-frequency analysis-based approach that averages and fuses features, resulting in more accurate predictions by effectively localising the complex nature of physiological signals.

2.3.3.3 Optical methods

Non-invasive glucose monitoring with optical sensing techniques is the most commonly used approach because it enables examination of light interactions with living tissues. The estimation of BG by Photoacoustic spectroscopy is investigated. It involved two pulsed laser diodes and a multifaceted apparatus to estimate BG. Other methods, such as Raman spectroscopy [15] and Near-Infrared (NIR) spectroscopy, have been discussed to identify glucose molecules. In NIR spectroscopy, infrared light that passes through the tissue is used at specific wavelengths where glucose absorbs. Glucose concentration can be estimated using computational models based on signal differences [16], which have led to several NIRs-based sensor prototypes with better precision [17], [18]. Also, smart devices with multiple infrared sensors and ML algorithms are being developed to monitor BG with greater accuracy in smart health care systems [19], [20]. In addition, photoacoustic spectroscopy is also studied to enhance the precision of glucose detection. Two-wavelength photoacoustic spectroscopy and a kernel-based calibration method are proposed and demonstrated as a superior alternative to conventional one-wavelength techniques [21]. Pirnstill et al. used dual-wavelength polarimetry to compensate for corneal birefringence and motion artefacts for in vivo glucose monitoring [22]. In addition, the analysis of optical pulse signals using photoplethysmography (PPG) and ML has proven feasible for estimating BG [23], [24]. Microwave-based non-invasive methods monitor variations in the dielectric properties of the glucose mixture, using dual-frequency resonators and wearable antenna sensors [25], [26] to estimate glucose concentration, and optimising a dual-channel NIR sensor via Monte Carlo simulations [27] to improve optical sensitivity. However, such methods have limited accuracy and have not been fully tested in clinical settings on a large scale because they are only validated in a simulation environment or in small clinical cohorts, are prone to motion artefacts and physiological variability, have complex sensor alignment requirements, and have not been fully tested in large clinical settings.

2.3.3.4 Limitations of non-invasive methods

Even after extensive research, non-invasive BG monitoring methods still face several challenges. These techniques are influenced by physiological factors, such as skin thickness, saliva characteristics, sweat composition, and ambient variables, which in turn affect their accuracy. Moreover, many optical sensing systems require complex equipment and calibration, which limits their mobility and applicability for real-time CGM.

Table 2.1 illustrates the literature survey of non-invasive BG measurement methods. It comprises the sensing modality, operating wavelength, algorithm, dataset size, performance metrics, and reported limitations. It explains how traditional and emerging artificial intelligence (AI)-based multimodal sensing systems have replaced spectroscopic and microwave sensing techniques. It outlines the challenges that remain to be overcome to realise accurate, clinically viable non-invasive glucose monitoring.

Table 2.1: Literature review of state-of-the-art non-invasive BG measurement methods

Ref.	Sensing Modality	Wavelength	Algorithm	Dataset Size	Performance Metrics	Key Limitations
Dai et al. 2009 [8]	Bioimpedance spectroscopy	Electrical impedance spectrum	Statistical estimation	-	Correlation analysis	Bioimpedance affected by tissue hydration and electrode placement
Monte-Moreno et al. 2011 [24]	PPG	Red and Infrared PPG (dual wavelength)	Ridge linear regression, FCN, support vector machines, random forests	410 subjects	coefficients of determination (R^2), CEGA	Small subject population; Evaluated mainly under controlled conditions; Performance affected by motion artifacts and individual physiological variability
Pirnstill et al. 2012 [22]	Dual-wavelength Polarimetry	532 nm and 635 nm lasers	Linear regression	In vivo animal (rabbit) experim-ents	mARD, CEGA	Requires precise optical alignment; Corneal birefringence and eye motion remain challenging despite dual-wavelength compensation; Not validated in humans
Song et al. 2015 [9]	Bioimpedance + multi-wavelength NIRs (m-NIRs)	850 nm, 950 and 1300 nm	-	10 subjects	mARD, CEGA	Small dataset; Subject-specific calibration required
Shih et al. 2015 [15]	Transcutaneous Raman spectroscopy	Raman laser (830 nm)	-	-	RMSE, CEGA	Weak Raman signal; Expensive instrumentati-on; Motion sensitive

Malik et al. 2016 [6]	Electrochemical saliva sensing	-	Logistic regression, ANN, SVM	175 saliva samples	accuracy, precision, sensitivity, F1 score	Saliva affected by oral conditions; No CGM
Cherkasova et al. 2016 [10]	Terahertz spectroscopy	Terahertz (0.1–10 THz)	-	6 subjects	Spectral analysis	High water absorption; Laboratory setup only
Haxha et al. 2016 [17]	NIRs	940 nm	-	Prototype evaluation	Error analysis	Ambient light and skin thickness affect accuracy; Prototype only
Ali et al. 2017 [16]	Visible laser transmittance/ refraction	Visible laser (650 nm)	-	45 subjects	Correlation, Mean Error	Sensitive to finger alignment; Limited clinical validation
Prasad et al. 2018 [7]	Electrochemical nanoparticle electrode	-	-	saliva samples	Sensitivity, Detection limit	Laboratory sensor; Not suitable for wearable/non-invasive monitoring
Pai et al. 2018 [21]	Dual-wavelength photoacoustic spectroscopy	940 nm and 1300 nm	Kernel-based calibration	-	RMSE, mARD, MAD, CEGA	Complex instrumentati-on; Acoustic noise sensitivity; Limited validation.
Singh et al. 2019 [5]	Optical saliva biosensor	590 nm	None	-	LOD	Weak saliva-BG correlation; Limited clinical applicability
Jain et al. 2019 [18]	NIRs	940 nm and 1300 nm	Huber model	200 subjects	mARD, MAD, RMSE, AvgE	Physiological parameters not considered; Regression model limits nonlinear learning
Habbu et al. 2019 [23]	PPG	Infrared LED (940 nm)	FCN	611 subjects	R^2, CEGA	Small clinical dataset; Affected by skin properties, Peripheral perfusion, and motion artifacts
Joshi et al. 2020 [12]	m-NIRs	940 nm and 1300 nm	Deep Neural Network (DNN)	74 subjects	Average Error (AvgE), mARD, CEGA	Limited dataset

Jain et al. 2020 [19]	m-NIRs	940 nm and 1300 nm	FCN	93 subjects	mARD MAD RMSE AvgE	Limited dataset; Capillary glucose only; no physiological parameters
Althobaiti et al. 2021 [27]	NIRs	1200-1900 nm	-	-	SNR	Simulation only; No experimental or clinical validation
Joshi et al. 2022 [13]	m-NIRs	940 nm and 1300 nm	Deep Neural Network (DNN)	4 subjects	-	Focused on security; Limited physiological parameter integration
Mohammadi et al. 2023 [25]	Dual-frequency microwave resonator	Microwave	-	Aqueous glucose samples	Sensitivity	Only aqueous glucose tested; No human validation
Kirubakaran et al. 2023 [26]	Microwave active sensor antenna	Microwave	-	150 subjects, 410 samples	Accuracy	Motion artifacts; Prototype evaluation; No ML
Sun et al. 2023 [11]	m-NIRs	1370 nm and 1640 nm	Random Forest	5 subjects	RMSE, mARD, CEGA	Requires multimodal hardware; Limited external validation
Jain et al. 2024 [20]	m-NIRs	940 nm and 1300 nm	DNN	116 subjects	mARD AvgE, R^2	Small dataset; Only Blood Pressure and body temperature considered

2.4 Machine Learning in healthcare

Machine learning (ML) has arisen as a key tool in disease diagnosis, enabling computational models to learn from patient data that support diagnostic decision-making and predictive analysis. Healthcare has extensively utilized ML techniques for predictive modelling, patient monitoring, medical image analysis, and disease diagnosis. Large amounts of CGM data can be analysed using ML algorithms to identify patterns in glucose changes for diabetes management. Predictive models that forecast future BG levels from past measurements and other physiological variables can be created using these methods.

Traditional ML and DL are the two main classes of ML approaches. With differing degrees of effectiveness, both strategies have been used to solve glucose prediction problems.

2.5 Machine Learning Techniques used for BG estimation

Several ML techniques are applied to CGM data to predict BG levels. Usually, these techniques depend on statistical correlations between input variables and glucose results.

Typical conventional ML techniques consist of:

- K nearest neighbour
- Support vector machine
- Decision Tree
- Random Forest
- Multiple Linear regression
- Support Vector Regression

2.5.1 K- nearest neighbour

The simplest ML technique is k-nearest neighbour (k-NN) [28]. The method uses labeled examples to memorize the features and labels associated with a dataset.

k-NN Algorithm steps:

- Select the number of neighbours (*k*) to take into account.
- Determine the target point's Euclidean distance (*d*) from every other point in the collection. Equation 2.1 calculates the Euclidean distance (*d*) in two-dimensional space between A (x_1, y_1) and B (x_2, y_2).

$$d = \sqrt{(x_1 - x_2)^2 + (y_1 - y_2)^2} \tag{2.1}$$

  The formula can be generalized to multi-dimensional inputs, respectively.
- Choose the *k* data points with the smallest distances to the target point.
- Among the k-NN, the class label that occurs most often should be assigned.

2.5.2 Support vector machine

Support Vector Machine (SVM) [28], [29] is frequently used in many different applications and is especially useful for high-dimensional datasets. Finding a hyperplane that optimizes

the margin between each class is the main objective of SVM (Figure 2.4). This gives the classes a strong division. Equation 2.2 represents the hyperplane equation:

$$\boldsymbol{W^T x + b_0 = 0} \tag{2.2}$$

Where $\boldsymbol{x}$ = vector of input feature, $\boldsymbol{b_0}$= bias, W = weight vector.

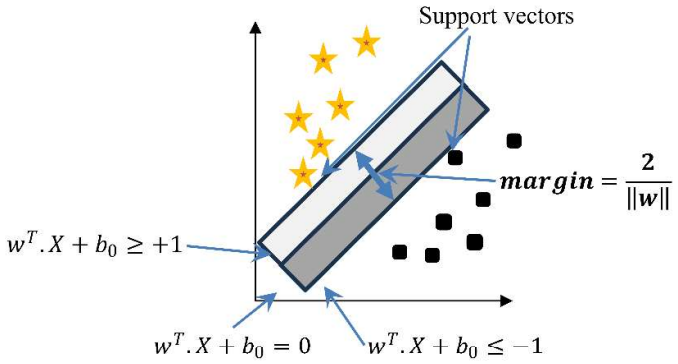

Figure 2.4: SVM classification with space of multidimensional feature. Rectangular boxes and stars represent classes [28]

The separation between the support vectors and the hyperplane is referred to as the margin (Equation 2.3).

$$\text{Margin} = \frac{2}{\|W\|} \tag{2.3}$$

$\|W\|$ should be minimized to maximize margin subject to the constraint that all training samples satisfy a correct classification condition, expressed as $y_i(w^T.x_i + b_0) \geq 1$, where y_i is the class label. Support vectors are the data points closest to the separating hyperplane in each class, and they are important in determining the decision boundary.

2.5.3 Decision Tree

Decision Tree [30] is structured as a tree, where the branches denote the decision rules, the internal nodes denote the features or qualities, and the leaf nodes denote the results or desired values. Regression and classification tasks are both performed using a Decision Tree.

Methods for constructing a decision tree:

- Determine which characteristic best divides or categorizes the data.

- Usually, this is accomplished by computing metrics for each feature. The Gini Index is used for classification, and variance is used for regression.

$$Gini\ index(S) = 1 - \sum_{i=1}^{c} p_i \tag{2.4}$$

$$Variance\ (S) = \frac{1}{|S|} \sum_{i=1}^{|S|} (y_i - \bar{y})^2 \tag{2.5}$$

where S denotes the current set, y_i denotes the i^{th} data point target value, $\bar{y}$ denotes the target values' mean in set S, p_i denote the i^{th} class probability in set S.

- Based on the selected feature and its corresponding threshold, split the dataset into subsets.
- Repeat the above procedure that creates leaf nodes for each subset. Using only the remaining features, decide which feature in each subset is ideal for splitting.
- For classification, a class label is assigned to a leaf node; for regression, a predicted value is assigned.

In order to come up with predictions of a new data point, you would use the decision pathways along each root to the leaf node, depending on its feature values. The value of a leaf node is the final prediction, which, in the case of classification, is a class label or, in regression, is a continuous output.

2.5.4 Random Forest

Random Forest (RF) [31], [32] builds many decision trees and aggregates their predictions to minimize overfitting. It is also utilized for regression and classification tasks. The primary procedure for building an RF is as follows:

- To construct a bootstrap sample from the original data set, N data points are randomly selected with replacement. Several bootstrap samples are produced by repeating this procedure.
- For every tree, choose a subset of features at random.
- Create a DT for every feature subset and bootstrap sample.
- To build a forest of decision trees, repeat steps 1-3.
- In each classification, every tree is a prediction of a single classification job, and the overall prediction of the trees is the most frequently predicted classification. To

obtain a final prediction for a regression task, the mean of each tree's predictions is taken.

2.5.5 Multiple Linear regression

Multiple Linear Regression (MLR) [33] is a statistical method that uses Equation 2.6 to estimate the relationship between input attributes and the desired output.

$$Y = \alpha_0 + \alpha_1 x_1 + \alpha_2 x_2 + \cdots + \alpha_n x_n + \varepsilon \tag{2.6}$$

The targeted output is denoted by Y, the intercept by α_0, the error term by ε, and the coefficients corresponding to the input characteristics x_1, x_2, …, and x_n are denoted by α_1, α_2, …, and α_n, respectively. MLR desires to minimize the difference between the actual targeted output Y and the predicted output ($\hat{Y}$) by estimating the α_0 , α_1, α_2,…, α_n.

2.5.6 Support Vector Regression

Support Vector Regression (SVR) [34] is an extension of the SVM that can be applied to regression, where the objective is to predict continuous output values. Rather than minimizing prediction error alone, SVR attempts to fit a function with a certain tolerance (ε), so that errors within that tolerance can be neglected. Equation 2.7 defines the hyperplane and margin of tolerance ε.

$$F(x) = |y_i - (\omega^T x + \alpha_0)| \leq \varepsilon \tag{2.7}$$

Where, α_0= bias, x = vector of input feature, and ω^T = weight vector.

Any mistakes that fall outside this tolerance are punished; those that fall within it are forgiven. Equation 2.8 represents the loss of SVR:

$$Lf\big(y, \mathrm{F}(x)\big) = max(0, |y - \mathrm{F}(x)| - \varepsilon) \tag{2.8}$$

The sum of these losses, represented by Equation 2.8, is minimized using Equation 2.9.

$$min_{w,b_0} \frac{1}{2}\|w\|^2 + C\sum_{i=1}^{N} L\big(y_i, f(x_i)\big) \tag{2.9}$$

Here, C represents a regularization parameter that helps the model avoid overfitting during training. SVR finds the optimal hyperplane that satisfies the optimization problem's requirements by adjusting the model's weights and biases throughout training.

2.6 Deep Learning Methods used for Glucose estimation

2.6.1 Fully Connected Network

Fully Connected Network (FCN) or a dense neural network, is a type of Artificial Neural Network (ANN) where each node of a specific layer is linked with every other node in the following layer. The input, hidden, and output layers make up the FCN. The input layer has a node for every feature of the incoming data. The FCN's output layer produces the final output. The FCN's general architecture is shown in Figure 2.5.

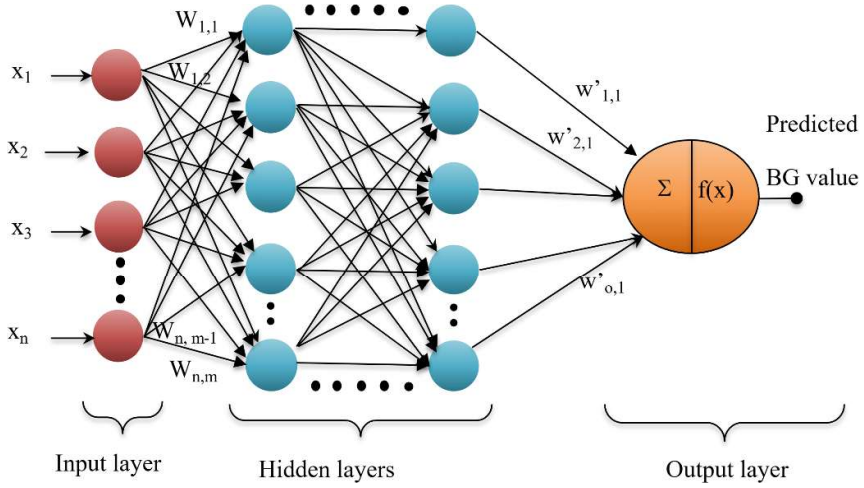

Figure 2.5: General architecture of FCN [19]

In Figure 2.5, n represents the number of neurons in the preceding layer, and x is the input features. m and o represent the number of hidden neurons used in hidden layers. W_{ij} is the weight associated with each connection. Each neuron uses an activation function for its output after a linear transformation. The output of the l^{th} layer, Z^l, is calculated as follows (Equation 2.10):

$$Z^{(l)} = f\left(W^{(l)}Z^{(l-1)}+b^{(l)}\right) \tag{2.10}$$

Here, $Z^{(l-1)}$ denotes the input to layer l, $W^{(l)}$ represents the weight matrix, $b^{(l)}$ represents the bias vector, and f represents the activation function. The output $Z^{(l)}$is then passed to the next layer.

During training, biases and weights are updated to minimize the loss using the loss function's gradient. Cross-entropy is utilized in classification tasks, while Mean Squared Error (MSE)

is applied for regression tasks, and the Rectified Linear Unit (ReLU) is used as the activation function for each neuron.

$$Cross\ Entropy\ Loss = -\sum_{i=1}^{N} y_i log\ (\hat{p}_i) \tag{2.11}$$

Where N, $\hat{p}$ and y are the number of classes, predicted probabilities, and actual label, respectively.

$$MSE\ loss = \frac{1}{n}\sum_{i=1}^{n}(y_i - \hat{y}_i)^2 \tag{2.12}$$

Where $\hat{y}$ and y are predicted and targeted output, respectively. n represents the total samples.

ReLU activation function is given by Equation 2.13.

$$ReLU\ (x) = \max(0, x) \tag{2.13}$$

2.6.2 Convolutional Neural Network

Convolutional Neural Network (CNN) [35], [36] can learn extremely complex features from input data due to their feed-forward architecture. It is composed of multiple processing layers, each of which learns distinct characteristics from the input data. The first layers learn high-level important features, whereas the deeper layers learn least-level features. CNN offers features for sharing weights. Figure 2.6 depicts the CNN architecture.

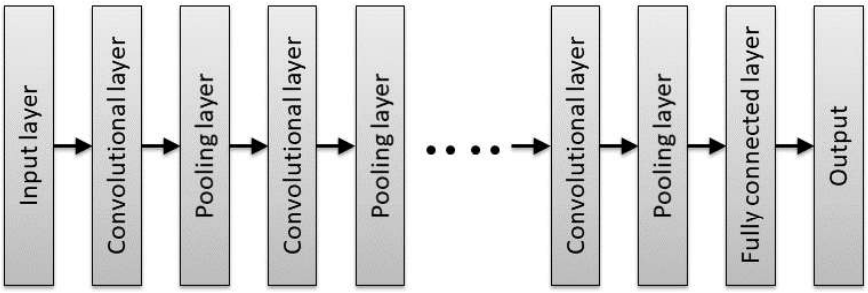

Figure 2.6: Generalize CNN architecture with convolutional, pooling and dense layers [35]

CNN has many convolutional and pooling layer pairs. Finally, a Fully Connected (FC) layer is employed. Each convolutional layer contains several kernels, known as filters. A feature

map is produced by performing a convolution operation between filters and input metrics. Equation represents the convolution operation of each layer.

Let the input matrix be $X \in \mathbb{R}^{H \times W}$ and the kernel (filter) be $K \in \mathbb{R}^{f \times f}$.
The convolution output at location (i, j) is

$$Y(i,j) = \sum_{m=0}^{f-1} \sum_{n=0}^{f-1} X(i+m, j+n)\, K(m,n) + b \tag{2.14}$$

Where H and W represent height and width of input matrix, f is a size of the kernel (filter dimension $f \times f$), m and n are indices representing kernel positions, $Y(i,j)$ is an output value at position (i,j) in the feature map and b is the bias term.
At the start, each kernel is assigned a random weight during training. Each training epoch includes extracting important features by the kernel and updating the weights. Each CNN layer is preceded by an activation function, which provides the model with non-linearity. A nonlinear activation function, like ReLU, is frequently used after convolution:

$$A(i,j) = \sigma(Y(i,j)) \tag{2.15}$$

where $\sigma(x) = \max(0, x)$

The pooling layer down samples features maps, reducing their size without losing the most significant information. Max Pooling is the most commonly used pooling technique. Equation represents pooling operation of window size $f \times f$:

$$Y(i,j) = \max_{0 \le m,n < f} X(i+m, j+n) \tag{2.16}$$

The output of the final pooling or convolutional layer is flattened and fed to the dense layers.

The dense layer operation is defined as Equation 2.17:

$$z = Wx + b \tag{2.17}$$

After activation function:

$$a = \sigma(z) = \sigma(Wx + b) \tag{2.18}$$

where x represents Input feature vector after flattening, W represents dense layer weight matrix, b represents bias vector, z represents linear combination of inputs, a represents activated output, and σ represents activation function.

2.7 Feature extraction using Explainable AI

Explainable AI (XAI) feature extraction focuses on quantifying the interpretable contribution of input features to a model's prediction [37]. XAI methods such as Local Interpretable Model-agnostic Explanations (LIME) and Shapley Additive Explanations (SHAP) provide both local and global views of feature relevance [38]. On the contrary, the traditional feature extraction techniques are mainly based on dimensionality reduction or transformation. Such approaches allow prioritizing characteristics by impact, making it easier to choose the most informative features and discard the unnecessary or less important ones. The extraction of features using XAI helps understand the influence of physiological features on prediction results in data-driven systems such as BG estimation.

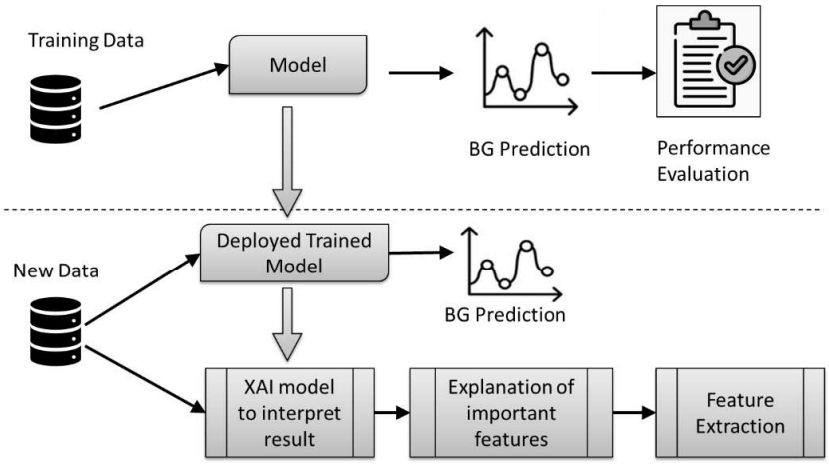

Figure 2.7: Conceptual diagram for Feature extraction using XAI [39]

Figure 2.7 shows a conceptual diagram of Feature extraction using XAI [39], which describes how the model predicts outcomes and which features are most significant for the prediction. Initially, training data is used to train the ML model. The trained model is then incorporated into an XAI framework, which feeds it with new input data to make predictions. The model uses the data to predict BG levels, and XAI analyses and explains the expected results. Based on the outcome, the most important features contributing to the prediction can be identified, and feature extraction is performed.

2.7.1 Shapley Additive Explanations

After refining the dataset, the SHAP [40] method is applied to identify the features that significantly contribute to BG estimation. SHAP calculates the Shapley values for each feature of the complex model to determine each feature's contribution to predicting the output [41]. Shapley value is defined in Equation 2.19 [40]. This process allows us to eliminate the least important features, thereby simplifying the ML model.

$$\emptyset_j(x) = \sum_{s \subseteq \{x_1, x_2, \ldots, x_m\} \setminus \{x_j\}} \frac{|s|!(m-|s|-1)!}{m!} (val\ (s \cup \{x_j\} - val(s))) \quad (2.19)$$

Where, $\emptyset_j(x)$ presents Shapley value of feature x_j, m indicates the total available features, s represents the model's subgroup for a given feature, and val represents the corresponding predicted feature values.

2.7.2 Local Interpretable Model-agnostic Explanations

LIME [42] is a local explanation technique that helps networks make complex models interpretable. LIME first builds an expanded dataset by perturbing the data. LIME then uses the additional dataset to train an interpretable model. Lastly, the test dataset is used to contrast the LIME interpretable model with the black-box model.

Let g be the explanatory model, and y be the initial prediction function. g is a member of the set of explainable models represented by G. In this case, the prediction $y(x)$ at input x needs to be explained. First, the mapping function h_x (x = $h_x(x')$) is used to convert x to an interpretable x'. Following that, x' is perturbed, and instances are generated around x'.

A weight π_x is assigned to each instance. The model complexity is measured by adding $\Omega(g)$, which assigns lower weights to examples that are far from x' and higher weights to instances that are close to x'.

Equation 2.20 [42] provides the explanation generated by LIME:

$$\xi(x) = \underset{g \in G}{argmin}\, \mathcal{L}(y, g, \pi_x) + \Omega(g) \quad (2.20)$$

Using the perturbed dataset, the explanation of $\xi(x)$ is obtained via optimization of $\mathcal{L}$.

2.8 Methods for Blood Glucose forecasting

Controlling BG levels within the glycaemic range is vital for T1D to prevent both critical and long-term complications. As a result, accurate forecasting of BG levels has become a critical area of research. Advances in CL systems, such as AP technologies, have enabled automated insulin delivery. However, challenges remain, particularly in Postprandial Glucose Control, as it can be difficult to estimate the required insulin dose based on food intake manually [43], [44], [45], [46]. Predictive models to improve glycaemic control and Time in Range (TIR) have been made easier by the availability of CGM data, as well as physiological and behavioural inputs like insulin, nutrition, and physical activity [47], [48]. However, reliable forecasting is a difficult time-series problem because BG dynamics are intrinsically nonlinear, patient-specific, and influenced by numerous external factors [49]. As a result, numerous computational methods have been put forth, which can be roughly divided into four main categories.

2.8.1 Classical and ML-Based Methods

The early BG prediction systems utilized various statistical and ML methods, including Autoregressive Integrated Moving Average (ARIMA), regression models, and ANNs. These techniques established a fundamental framework for glucose forecasting. While ARIMA offers interpretable time-series modelling, it has limitations in capturing the nonlinear fluctuations of glucose levels [50]. In contrast, ANN-based algorithms improve prediction accuracy by learning nonlinear correlations from continuous glucose monitoring (CGM) data and artificial features [33], [51]. Nevertheless, most of these techniques continue to rely on manual feature engineering, even with these developments. Also, they do not adequately represent long-term temporal relationships, rendering them incapable of adapting to the complex patterns of physiological regulation.

2.8.2 Deep Learning-Based Sequential Models

Sequential models based on DL, such as simple Recurrent Neural Networks (RNNs), Long Short-Term Memory (LSTM) [52], [53], Gated Recurrent Unit (GRU) [54], [55], and Bidirectional LSTM [56], have been popular in attempts to better learn temporal dependencies in glucose dynamics. These models have produced significant improvements in prediction accuracy across a range of Prediction Horizons (PHs) by successfully identifying sequential patterns in the CGM data [57], [58]. Accurately estimating BG levels

is challenging because factors beyond insulin infusions affect actual glucose levels. The use of these characteristics as input components in BG forecasting across various PHs has been previously studied, leading to improved forecast accuracy [59], [60]. Although other optimization methods, such as Particle Swarm Optimization, and signal decomposition methods, such as Variational Mode Decomposition, enhance prediction performance by reducing noise and extracting inherent features, they are also improved by the bidirectional learning that enhances context understanding [61], [62]. Nevertheless, these models may continue to fail to address both long-term dependence and short-term oscillations simultaneously, particularly when glucose levels vary rapidly.

2.8.3 Hybrid and Ensemble Models

Some proposals have been made to combine the strengths of different models using hybrid and ensemble models. Convolutional Recurrent Neural Network (CRNN), CNN-GRU, and CNN-LSTM are hybrid models that combine convolutional features with sequential-based learning, enabling the use of more global and local temporal BG patterns [63], [64], [65]. Ensemble methods enhance the strength and predictive power by aggregating the results of multiple learners [66]. These methods involve stacking models that have been enhanced using methods such as Grey Wolf Optimization. It also incorporates feature engineering and signal transformation techniques to convert event-based inputs into continuous representations, thereby enhancing model performance [58]. Adaptation of risk-conscious groups improves safety-critical forecasting [67]. These models are, however, typically computationally expensive, hard to interpret, and not necessarily suitable for real-time or resource-constrained operation.

2.8.4 Advanced and Emerging Approaches

Recent research has increasingly explored advanced approaches, including transformer-based models, Neural Architecture Search (NAS), personalized learning frameworks, and Large Language Model (LLM)-based predictors. Transformer designs are more effective than traditional recurrent models at handling long-range dependencies and multi-horizon dynamics in glucose [56], [68], [69]. To optimize model performance, NAS methods automatically design architectures and optimize hyperparameter search [70]. Incrementally trained LSTM models and multimodal frameworks that incorporate glucose, insulin, meal, and physical activity data enhance individual-specific prediction accuracy [71], [72], [73]. Also, with reduced inter-patient variability, LLM-based models have demonstrated

promising results with long PHs [74]. However, the applicability of these models in real-time and edge-device applications is limited, as they often have high data requirements and are computationally intensive.

2.8.5 Limitations of current BG forecasting models

Even though significant progress has been made across all categories, several challenges remain. Many models have a poor ability to capture both long-term glucose dynamics and short-term variability, particularly during severe hyperglycaemia. In addition, the issues of small sample size, limited generalizability, sensor noise, and patient heterogeneity continue to affect the model's robustness. Very accurate models, especially hybrid and transformer-based ones, are not well-suited for practice due to their computational complexity and limited interpretability. Such shortcomings highlight the need for powerful, scalable, and understandable BG forecasting models that can capture multiscale temporal variations while remaining applicable in real time.

2.9 Existing methods for Blood Glucose control

Maintaining BG levels within the euglycemic range (70-180 mg/dL) is key to preventing the acute and chronic health effects of T1D, including cardiovascular disease, kidney disease, and retinopathy [75]. Over the past decades, several BG control techniques have been proposed, starting from traditional open-loop approaches such as MDI therapy to advanced automated systems, such as CL and AP technologies. In traditional techniques, insulin dosing decisions are entirely patient-driven and often supported by CGM. In contrast, modern systems integrate sensing, actuation, and control algorithms to automate insulin delivery [76]. Clinical and real-world research has demonstrated that these strategies can lower the risk of hypoglycaemia and improve glycaemic outcomes, especially Time in Range (TIR) [77], [78], [79]. However, the majority of existing insulin dosing methods rely exclusively on current BG levels and fail to leverage projected data, which is essential for proactive glucose management.

2.9.1 Multiple Daily Injection Based Control Methods

The vast majority of T1D individuals worldwide rely on MDI therapy to manage BG levels, in which they receive exogenous insulin to supplement endogenous insulin production [80]. In this therapy, postprandial glucose is controlled using rapid-acting insulin to keep it within the recommended range. Insulin dosage is usually calculated using standard bolus formulas

based on current BG, CHO intake, insulin sensitivity, and correction factor [81]. According to the research, MDI has the potential to improve glycaemic control and is a feasible and acceptable option when combined with CGM, systematic education, and frequent self-management strategies [82], [83]. Theoretical models have also been used to model insulin delivery as impulsive control inputs, demonstrating consistent glucose regulation in the ideal case [84]. In addition to conventional formula-based approaches, ML-based bolus optimization has been proposed to enhance dosing accuracy [85]. Moreover, CGM-aided MDI can improve glycaemic awareness and reduce HbA1c, but only slightly, in observational and multicentre studies [86], [87]. With these advantages, CGM-based decisions are largely reactive, as insulin doses are typically based on current glucose levels rather than projected future glucose levels.

2.9.2 Insulin Pump Methods

An insulin pump delivers insulin continually with adjustable basal and bolus doses, offering an alternative to MDI. CGM sensors integrated into insulin pump systems improve glucose monitoring and support insulin dosing decisions. Clinical trials, including multicentre randomized studies, show that transitioning from MDI to insulin pump therapy improves glycaemic control and reduces HbA_1c levels in both adult and paediatric populations [88], [89]. Although direct comparisons are limited by variations in research design and patient selection, real-world registry analyses also suggest better glycaemic control with pump therapy compared with MDI and sensor-augmented methods [90].

2.9.3 Closed-Loop BG Control Systems

CL systems, also known as AP systems, represent a substantial development in BG control by combining CGM, insulin pumps, and control algorithms to automate insulin delivery [91]. Advanced Hybrid CL (AHCL) systems and tubeless insulin delivery technologies considerably improve glycaemic outcomes, including increased TIR and reduced hypoglycaemia across a variety of groups, according to multicentre randomized trials and real-world research [78], [79], [92], [93], [94]. Improved hyperglycaemia control without increased risk of severe hypoglycaemia is confirmed by a pooled analysis of Control-IQ studies [95], [96]. According to systematic evaluations, integrated AP systems that combine CGM, insulin infusion, and predictive algorithms consistently outperform traditional therapy[76]. Dual-hormone systems that include both glucagon and insulin improve safety by minimizing hypoglycaemic occurrences, especially during exercise and at night [97].

Emerging techniques, including intermittent CL systems for MDI users and innovative insulin delivery technologies, show improved glycaemic control without requiring complete automation [98], [99], [100], [101]. Even in these systems, PHs are often short, and management actions are rarely explicitly optimized for medium-term anticipated BG values.

2.9.4 Limitations of Existing BG Control Methods

Nevertheless, despite significant development, existing BG management systems have significant shortcomings. Innovative systems, including insulin pumps and CL technology, are typically associated with high prices, technical complexity, and the need to use the devices continuously, limiting their availability in resource-limited settings. A significant drawback of insulin pump and AP systems is that patients must wear external devices all day, which can be uncomfortable and inconvenient, and may reduce long-term compliance. Open-loop methods, e.g., MDI, rely on patient knowledge and manual calculations, as well as compliance, which can lead to unpredictable glycaemic outcomes. Most current systems are not sensitive to dynamic physiological variables, such as the unpredictability of meals, physical activity, and stress. Also, sensor issues, lack of personalization, and inability to respond to rapid glycaemic fluctuations reduce overall performance.

2.10 Summary

The chapter summarizes existing methods for managing diabetes, with a focus on BG monitoring, estimation, prediction, and control. It discusses various BG measurement methods, including invasive, minimally invasive, and non-invasive approaches, highlighting the importance of specific CGM systems. Particular attention is given to the limitations of invasive and minimally invasive methods that require skin penetration for BG sampling. These approaches carry a risk of infection for patients. Additionally, traditional invasive methods are unsuitable for CGM because they require multiple readings throughout the day, and the practice of repeatedly pricking a finger can be painful. Non-invasive methods are more appropriate for CGM. Researchers have reported prediction accuracies with an RMSE of 12.7 mg/dL, a MAD of 8.3 mg/dL, and a mARD of 5.34% for BG measurement using only sensor values.

Furthermore, prediction accuracy can improve by incorporating both sensor data and the patient's physiological parameters. This chapter discusses the use of XAI strategies for feature extraction and considers the roles of ML and DL in glucose estimation. However,

the BG forecasting models discussed are less accurate and often fail to effectively capture both short- and long- term dependencies, especially when glucose levels fluctuate rapidly. Additionally, the chapter reviews BG control methods, including MDI, insulin pumps, and CL devices. Current BG control methods struggle to maintain stable BG levels throughout the day, particularly amid variable meal-related CHO intake, which can lead to hyperglycaemic or hypoglycaemic events. In summary, the chapter emphasizes the need for predictive, accurate, and user-friendly technologies for monitoring and controlling glucose levels, while outlining the main barriers to achieving these goals.

Chapter 3
Experimental Dataset collection for Blood Glucose Estimation

3.1 Introduction

This chapter presents the establishment of a reliable dataset for non-invasive BG estimation. The chapter begins with an idea of a three-sensor non-invasive device and intelligent Glucometer (iGLU) data. The chapter also describes the use of XAI methodologies to identify the most important wavelengths for BG estimation. It also explains how to create datasets with a non-invasive, single-sensor device. The use of the inter-quartile range (IQR) methodology for outlier detection and data refinement to increase model accuracy and robustness is among the data preprocessing techniques presented.

3.2 Three sensor non-invasive device for BG estimation

An NIR spectroscopy-based an Intelligent Glucose Meter (iGLU) was developed using three sensors [19]. This device employs 940 nm for absorption and reflectance, and 1300 nm for absorption to detect glucose molecules in finger blood. Figure 3.1 demonstrates the fundamental diagram for BG estimation utilizing 3-sensor non-invasive device.

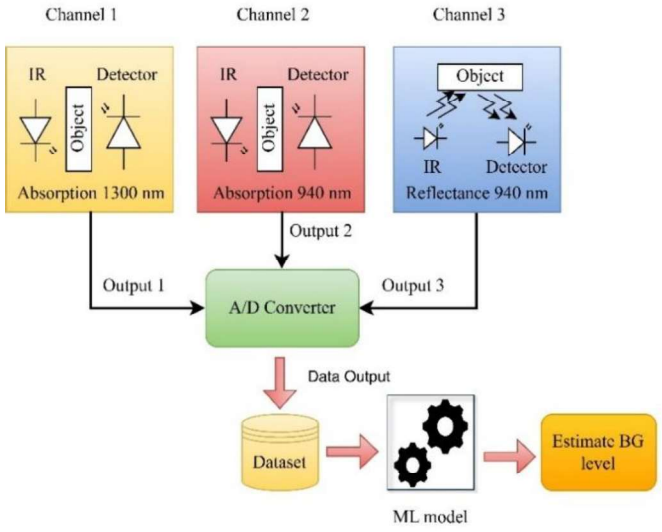

Figure 3.1: Fundamental diagram for BG estimation utilizing 3-sensor non-invasive device [19]

Three fingers are placed in the respective sensors, which generate corresponding voltages based on the concentration of glucose molecules. Figure 3.2 illustrates a 3-sensor non-invasive device worn on the fingers.

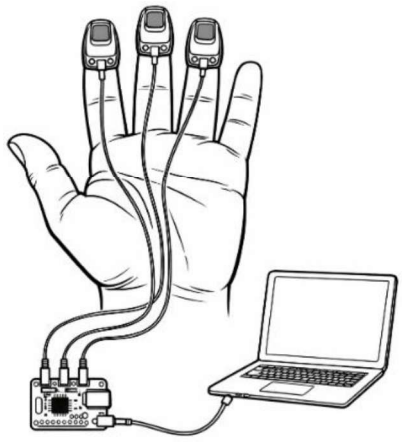

Figure 3.2: Illustration of a 3-sensor non-invasive device worn on fingers [19]

An FCN model with 10 layers and 10 hidden neurons per layer was implemented and validated using data collected from 96 participants who used the device [19]. Table 3.1 summarizes the participants' gender, age and diabetic related information. The collected dataset includes data from the three sensors (channels 1, 2, and 3), capillary glucose, along with information on gender, age, and weight. This dataset is referred to as the iGLU dataset in the thesis.

Table 3.1: Gender, age and diabetic information of participants of iGLU dataset [19]

	Prediabetic		**Diabetic**		**Healthy**	
Gender	**Male**	**Female**	**Male**	**Female**	**Male**	**Female**
No of subjects	16	16	28	22	9	5
Age range (Years)	24-68	26-65	30-68	30-73	23-67	35-62

3.3 Identification of important wavelength for BG estimation using iGLU dataset

An FCN and a CNN are implemented to assess the performance of these networks with respect to participants' specific characteristics, as [19] relied solely on data from the three

sensors for BG estimation. We also aim to determine which specific sensor wavelength contributes most to BG estimation among the three sensor wavelengths. Table 3.2 and Table 3.3 contain the detailed layer-wise configurations of the FCN. The computation of learnable parameters in a dense layer is:

$$\text{Learnable parameters of dense layer} = (\text{input} \times \text{neurons}) + \text{bias} \tag{3.1}$$

Table 3.2: FCN architecture with layer-wise detailed configuration

Implementation of FCN		
Layer	**Neurons**	**Learnable parameters**
Dense 1	Input features: 6, neurons: 10	70
Dense 2	10	110
Dense 3	10	110
Dense 4	10	110
Dense 5	10	110
Dense 6	10	110
Dense 7	10	110
Dense 8	10	110
Dense 9	10	110
Dense 10	10	110
Output	1	11
	Total	1,071

Table 3.3 contains the detailed layer-wise configurations of the CNN. The computation of learnable parameters in a convolution layer is:

$$\text{Learnable parameters of convolution layer} = (k \times i \times f) + f_0 \tag{3.2}$$

Where, k = kernel size, i = input channel, f = number of filters applied in convolution layer, and f_0= number of biases. Our data is one dimensional. Therefore, i =1 for FCN.

The ReLU activation function is used in both networks (Equation 3.3).

$$Relu\ (x) = \max(0, x) \tag{3.3}$$

Table 3.3: CNN architecture with layer-wise detailed configuration

Implementation of CNN			
Layer	**Filter size/ Neurons**	**Output shape**	**Learnable parameters**
Convolution 1	f= 6, k = 2, i =1	(6, 6)	18
Pooling 1	Max pooling, size: 2	(3, 6)	0
Convolution 2	f= 16, k = 2, i =6	(3, 16)	208
Pooling 2	Max pooling, size: 2	(2, 16)	0
Dense layer 1	128 neurons	128	4,224
Dense layer 2	64 neurons	64	8,256
Output	1 neuron	1	65
		Total	12,771

We have used two sets of inputs, with and without scaling, to train the FCN and CNN. In the first method, we used raw, unscaled inputs. The FCN and CNN are trained on the same dataset using the Min-Max scaler, which scales each input to the range [0, 1]. The min-max scaler [102] is represented by Equation 3.4.

$$MinMax\ scaler, \qquad X' = \frac{X - X_{min}}{X_{max} - X_{min}} \tag{3.4}$$

Where X is the actual value of input feature, and X_{max} and X_{min} are the maximum and minimum values of the input feature in the training dataset, respectively. The normalized output, X', is adjusted to a range of [0, 1] for training the model.

3.3.1 Performance evaluation metrics

3.3.1.1 Root Mean Square Error (RMSE)

RMSE measures the difference between the target values and the model-predicted BG values [53].

$$RMSE = \sqrt{\frac{1}{M}\sum_{n=1}^{M}(y_n - \widehat{y_n})^2} \tag{3.5}$$

Where, M is the total predictions, y_n and $\widehat{y_n}$ are targeted and model-predicted BG outputs, respectively.

3.3.1.2 Mean Absolute Relative Difference (mARD)

mARD measures the model's performance by averaging the absolute differences between the target values and the model-predicted BG values. It is estimated according to Equation 3.6. When the mARD is lower, the predicted value is closer to the actual value. An mARD below 10 percent is usually taken to indicate that a model or device is performing well.

$$mARD = \frac{1}{M}\sum_{k=1}^{M}\frac{|y_k - \widehat{y_k}|}{y_k} \tag{3.6}$$

Where, M is the total predictions, y_k and $\widehat{y_k}$ are targeted and model-predicted BG outputs, respectively.

3.3.1.3 Mean Absolute Deviation (MAD)

The MAD metric shows the mean absolute difference between each BG predicted value by the model and the mean predicted value. It displays the distribution of the predicted values. Equation 3.7 is used to determine MAD.

$$MAD = \frac{1}{M}\sum_{n=1}^{M}(\hat{y}_n - \bar{y}) \tag{3.7}$$

Where, M is the number of predictions, $\hat{y}_n$ is the predicted value, $\bar{y}$ is the mean of $\hat{y}_n$.

3.3.2 Performance analysis of implemented FCN and CNN

Table 3.4 compares the performance evaluation of the implemented FCN and CNN with prior work [19]. After analysing the results, Table 3.4 demonstrates that both models outperform prior work. When trained on scaled data, the FCN model has an mARD of 1.7, a MAD of 3.45 mg/dL, and an RMSE of 6.27 mg/dL.

In comparison, the CNN trained on scaled data demonstrates significantly better performance, with an mARD of 0.05%, a MAD of 0.06 mg/dl, and an RMSE of 0.12 mg/dl. The results demonstrate that the CNN model outperforms the FCN and previous studies. The findings indicate that the performance of the ML models can be enhanced by incorporating individuals' physiological parameters.

Table 3.4: Performance evaluation of the implemented models with prior work

Model name	Features	mARD (%)	MAD (mg/dL)	RMSE (mg/dL)
FCN [19]	3 Sensor data	7.32	9.89	11.56
FCN without scaling (Our work)	Gender, Age, Height, 3 sensor data	2.6	5.07	8.76
FCN with scaling (Our work)	Gender, Age, Height, 3 sensor data	1.7	3.45	6.27
CNN without scaling (Our work)	Gender, Age, Height, 3 sensor data	0.09	0.12	0.24
CNN with scaling (Our work)	Gender, Age, Height, 3 sensor data	0.05	0.057	0.12

3.3.3 Feature importance using Explainable AI

In this study, XAI is used to understand the contributions of the different sensors in the iGLU dataset, rather than to select the most relevant wavelengths. The goal is to determine the relative importance of the three sensors and to explore whether a single sensor could provide sufficient information to accurately estimate the BG level, thereby reducing hardware complexity, costs, and power consumption.

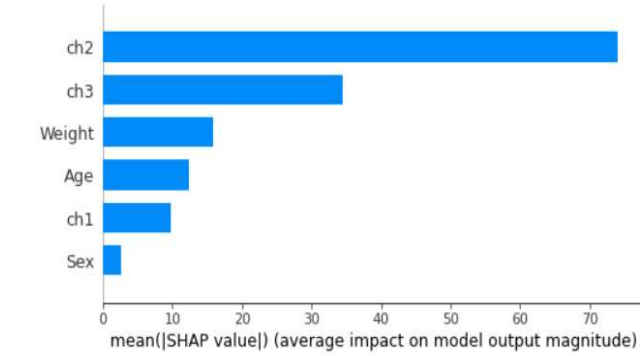

(a)

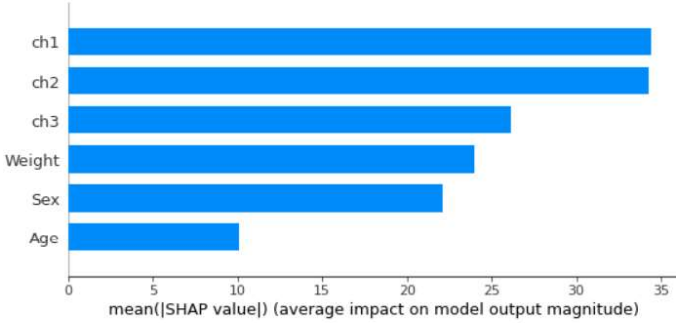

(b)

Figure 3.3: Feature importance calculating using SHAP (a) for FCN and (b) for CNN

The wavelengths used in the original iGLU dataset are physiologically relevant, and no changes in the sensors' wavelengths are made during this research. Based on the XAI analysis, the most informative sensor is selected for the next steps in developing the proposed single-sensor non-invasive BG measurement device.

Among the different XAI methods, we have used the SHAP approach to predict the individual contributions of three sensors and various features to BG estimation. Figure 3.3 shows the feature intensities used in the prediction process, indicating that channel 2 (940 nm absorption) is the largest contributor to BG estimation. This insight facilitates the development of a single, non-invasive BG-measuring device that leverages this sensor characteristic, thereby eliminating the need for multiple sensors.

3.4 Experimental Dataset collection for BG estimation using single sensor non-invasive device

Section 3.3.3 indicates that a single sensor having a wavelength of 940 nm is sufficient for BG estimation. Therefore, a single-sensor non-invasive device is developed using a 940 nm wavelength to estimate BG level. This device avoids using of three sensors for BG estimation. BG estimation data are collected using this instrument, which utilises NIR absorption spectroscopy at 940 nm. This method measures the amount of NIR radiation absorbed by molecules to detect glucose in blood. A single infrared (IR) sensor operating at 940 nm, with the detector located on the opposite side, is used to measure BG non-invasively. Figure 3.4 demonstrates the fundamental diagram of the BG estimation procedure using a single sensor.

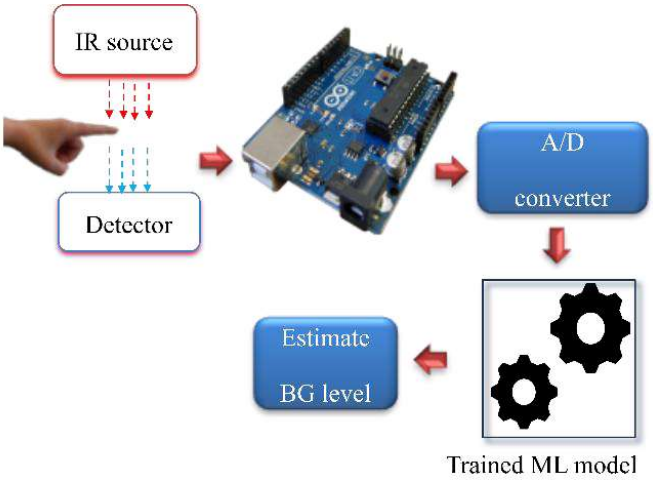

Figure 3.4: Fundamental diagram illustrating the BG estimation process using single sensor

When an IR source and the detector are placed between a finger, the IR waves are absorbed by the glucose molecules present in the blood. The detector then measures the remaining unabsorbed waves. The glucose molecules absorb waves based on the difference between the total released waves and those that remain unabsorbed. The device produces an electrical signal proportional to the BG level. The microcontroller's Analog-to-Digital Converter (ADC) then converts this signal into digital data. The BG level is represented as a five-digit number (approximately 0–25,000) by the ADC.

3.4.1 Hardware description: Single sensor non-invasive device for BG measurement

A single-sensor non-invasive device for BG data collection was designed and developed under the guidance of Dr Amit Joshi from MNIT, Jaipur. The same device was used to collect BG data in this work. Figure 3.5 illustrates the actual device used for BG data collection. The BG measurement system comprises a single sensor operating at 940 nm, a data acquisition module with a microcontroller, and a data logging interface to a computer.

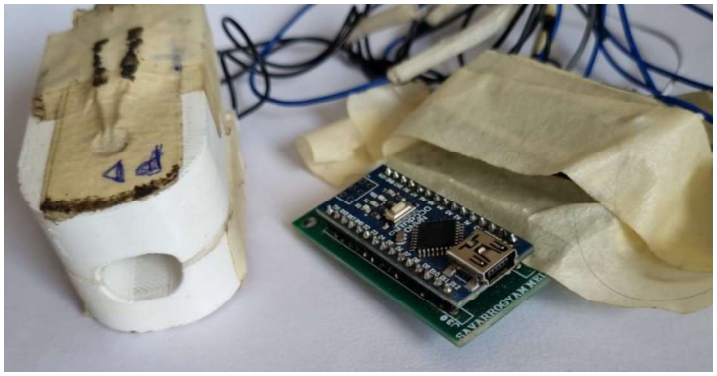

(a)

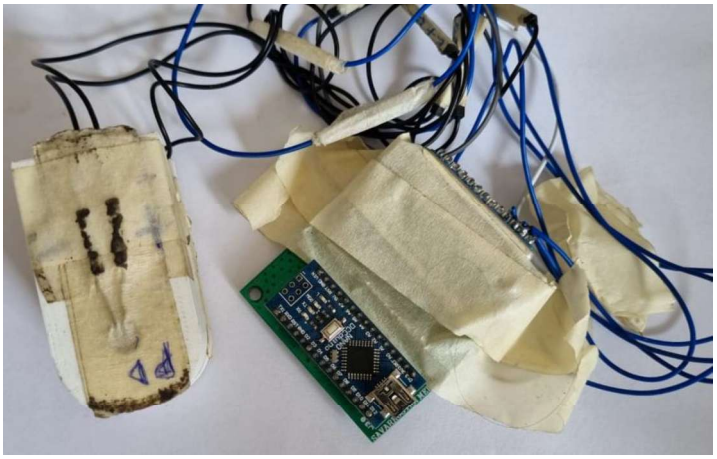

(b)

Figure 3.5: Actual hardware used for BG data collection (a) Front view (b) Top view

The sensor continuously collects the participant's physiological signal non-invasively and produces an analogue output proportional to the measured physiological parameter. The microcontroller then receives the signal via its ADC, which converts and formats the signal for transmission. Arduino Nano is used in the hardware implementation. The data are transmitted serially to a laptop via a USB serial port, enabling reliable, continuous data transfer. A custom data logging program is used on the computer to capture the serial data stream and automatically store each measurement in a Microsoft Excel spreadsheet for further pre-processing, analysis and ML model building. This hardware architecture offers a simple, portable, low-cost, and efficient solution for non-invasive BG data acquisition. It enables accurate synchronisation between the sensor's BG data and the reference BG data during clinical data collection.

3.4.2 Experimental Dataset Collection Protocol

From August-2023 to November-2023, a device was installed at the Shreenath Clinical Laboratory in Valsad, Gujarat, India, to collect BG data along with other relevant information. Written consent was obtained from all participants for data collection. The data were collected in a controlled laboratory environment using the developed non-invasive BG measurement device to minimize the effects of external variables.

The participants were seated in chairs to minimize motion artefacts during data acquisition and to ensure the sensors were positioned correctly. The finger was cleaned before the data was taken. The laboratory technician took a blood sample to measure serum glucose levels, while a simultaneous reading was obtained using a developed non-invasive device. This device took multiple consecutive readings to indirectly estimate the body's BG levels. The readings were saved in an Excel sheet for each participant using a laptop. Laboratory glucose (serum glucose) was used as the reference value (Targeted value).

Figure 3.6 illustrates the laboratory setup for a single-sensor non-invasive device, showing the positions of the finger and sensor. To reduce physiological variation in BG concentration, readings were taken using a non-invasive device, and a blood sample was collected in a laboratory within about 1-2 minutes of one another. All the measurements were taken at room temperature (24 - 27 °C) under normal laboratory conditions. BG was measured at various times (fasting, postprandial, and random) depending on participant availability. The total measurement procedure for each participant took about 3–4 minutes.

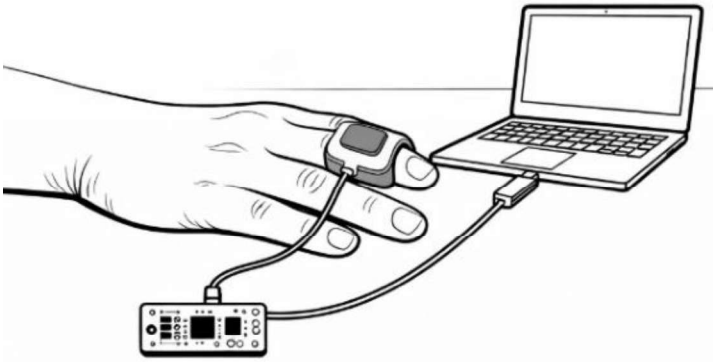

Figure 3.6: Illustration of a laboratory setup with single-sensor non-invasive device

The participants had a range of physiological properties, but the influences of different skin types (e.g., skin tone and thickness), and temperature and humidity were not examined separately. These factors could affect the sensor's operation in real-world applications. They will be explored systematically in future work to further evaluate the robustness and feasibility of the proposed device in clinical settings.

Written consent was obtained from all participants for data collection. Refer to Annexure-I for the participant's consent and data collection forms. Participants who voluntarily provided informed consent and satisfied the study requirements were included. At the same time, individuals with incomplete records, poor sensor measurements, or conditions that could interfere with reliable data acquisition were excluded.

Data were collected in two phases: 623 from August to October 2023 and 161 in November 2023. In this study, data were collected from 784 participants, including their BG levels and other relevant information. The details gathered included gender, age, systolic blood pressure (Sys. BP), diastolic blood pressure (Dia. BP), weight, heart rate, height, duration of diabetes, diabetes history, daily walking steps, sleep duration, sleep quality, smoking habits, alcohol consumption, and serum BG levels. This dataset is referred to as the Single-sensor dataset in the thesis.

Table 3.5 presents participants' gender information for the dataset generated using a single-sensor non-invasive device, grouped by age. Age groups are older adults (> 60 years), adults (19-59 years), and adolescents (13-18 years).

Table 3.5: Participants' gender information for the dataset generated using a single-sensor non-invasive device, grouped by age

Age Group (Years)	Gender Wise Samples
Male: - 21-85	Male: - 462
Female: - 14-80	Female: - 322
Adolescent (13-18 Years)	
Male: - -	Male: - 0
Female: - 14-18	Female: - 5
Adult (19-59 Years)	
Male: - 21-59	Male: - 294
Female: - 20-59	Female: - 194
Older Adult (>60 years)	
Male: - 60-85	Male: - 168
Female: - 60-80	Female: - 123

Table 3.6 presents the descriptive statistics of the dataset comprising 784 participants. For each parameter, the statistical metrics include the standard deviation (SD), mean, minimum (Min.), and maximum (Max.). These statistical analyses provide insights into the dataset's distribution, central tendency, and variability, which are used for additional modelling, outlier detection, and machine-learning-based prediction.

Table 3.6: Statistical distribution of recorded parameters of participants in Single-sensor dataset

Parameters	Unit	Min.	Max.	Mean	SD
Age	Years	14	85	53.67	12.91
Weight	Kilogram	25	124.4	67.36	13.12
Height	Centimeter	53	185.42	164.84	9.56
Sys. BP	mmHg	69	221	134.51	20.24
Dia. BP	mmHg	25	158	87.89	14.14
Duration of diabetes	Years	0	45	3.90	6.13
Heart rate	Bits/minute	40	150	85.39	13.76
Diabetes history	Years	0	5	0.47	0.99
Sleep time	Hours	3	10	6.81	0.93
Blood Glucose	mg/dL	57	464	135.06	58.18
Sensor value	-	4079	25197	14802.59	3728.19

Table 3.7 summarizes the distribution of categorical variables, including gender, slip quality, smoking status, and alcohol consumption. The values are represented as counts and corresponding percentages. This representation helps understand the dataset's composition and identify class imbalances that may influence model performance.

Table 3.7: Distribution of categorical parameters of participants in Single-sensor dataset

Parameters	Category	Count	Percentage (%)
Gender	Male	463	58.93
	Female	322	41.07
Slip Quality	Good	585	74.62
	Normal	174	22.19
	Bad	25	3.19
Smoking	No habit	771	98.34
	Current	11	1.4
	former	2	0.26
Alcohol consumption	No	743	94.77
	Regular	24	3.06
	Occasionally	17	2.17

3.5 Data preprocessing

In the data preprocessing phase, inaccurate sensor data arising from practical measurement constraints are excluded from the study. Two kinds of invalid measurements were found. The first is that if the participant's finger is not in the correct position, or if the finger size is too large or too small for the device's finger holder, the sensor output is below 7000, indicating an invalid measurement. Samples of this type are excluded in this work. Second, in practice, the sensor output saturates when the blood glucose level exceeds 230 mg/dL and yields virtually the same reading regardless of the actual glucose level. All samples are excluded from this work if the reference blood glucose exceeds 230 mg/dL, as this does not yield reliable data for model development.

Additionally, some HbA1c data are included in the dataset but are later excluded from the research. HbA1c represents the average glucose level of patients attached to their haemoglobin over the past two to three months. However, we were targeting current BG level measurements, so we excluded those readings from the research. When the BG data for subjects are recorded, multiple data points per subject are stored in an Excel file. Upon

reviewing, it is discovered that some readings fell outside a specific range. These outside data points are treated as outliers and should be removed. Figure 3.7 shows the recorded BG values in Excel for participants 8 and 26. Orange dots represent the outliers within the recorded data. These outlier data points are identified and removed using the IQR approach [103], [104]. The average of all remaining readings is then calculated to determine an analogous BG level for each individual after the outliers are excluded. Additional missing data points are found among the parameters recorded during participants' laboratory visits. The missing values are imputed using the parameter's mean.

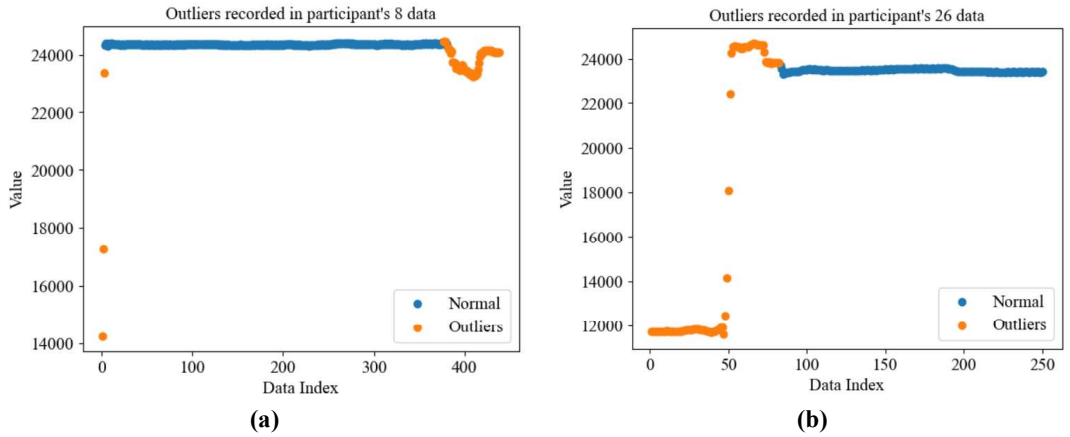

Figure 3.7: Visualization of recorded BG values for (a) Participant no. 8 and (b) Participant no. 26, highlighting the occurrence of outliers in the recorded data

Consequently, after data preprocessing, 552 cleaned participants' data are retained for further experimentation. The final set of 15 parameters used to estimate BG levels include device readings, gender, age, and Sys. BP, Dia. BP, weight, heart rate, height, duration of diabetes, diabetes history, daily walking steps, sleep duration, sleep quality, smoking habits, and alcohol consumption. The target values are the BG levels measured by laboratory personnel (serum glucose).

3.5.1 Inter-quartile range

The IQR is a method for identifying outliers in normally distributed data [103] . The IQR method is a robust statistical approach that accounts for the spread of the middle 50% of the data to detect and eliminate outliers. The primary benefit of this is that it is easy, requires less computation, and is less sensitive to extreme values than the mean or standard deviation (SD) approaches. Figure 3.8 illustrates the construction of a box plot for IQR. The first (Q1),

second (Q2), and third quartiles (Q3) are the separated ranges. IQR = Q3 − Q1 is the difference between the first and third quartiles. The IQR, which is technically an H-spread, is sometimes referred to as midspread or middle 50%. IQR can be used to create a boxplot, a straightforward graphical depiction of the interquartile range, and to divide the points into 25% intervals. This method divides the dataset into four equal sections, or quartiles.

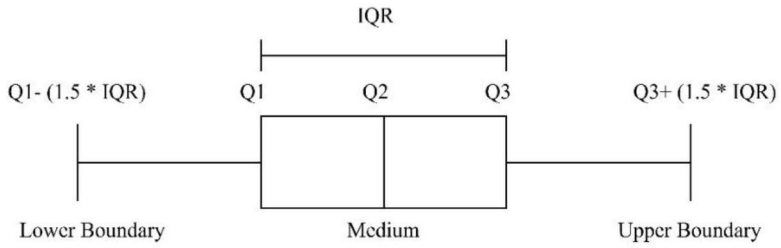

Figure 3.8: Illustration the construction of a box plot for IQR

The algorithm for outlier detection and removal using IQR is detailed in Algorithm 3.1.

Algorithm 3.1 Outlier detection and removal using IQR

Input:

Data = $\{x_1, x_2, x_3, ..., x_n\}$ // Input dataset

Output:

Clean_Data // Dataset after removing outliers
Outliers // Set of detected outliers

1: Sort the dataset in ascending order
2: Data sorted ← sort (Data)
3: Compute quartiles
4: Q1 ← 25th percentile of Data sorted
5: Q2 ← 50th percentile (median) of Data sorted
6: Q3 ← 75th percentile of Data sorted
7: Compute Interquartile Range
8: IQR ← Q3 − Q1
9: Compute bounds for outlier detection
10: Lower Boundary ← Q1 − (1.5 × IQR)
11: Upper Boundary ← Q3 + (1.5 × IQR)
12: Initialize empty set
13: Clean Data ← ∅
14: Outliers ← ∅
15: **for** each data point $\mathbf{x_i}$ in Data sorted **do**
16: **if** ($\mathbf{x_i}$ < Lower Boundary) OR ($\mathbf{x_i}$ > Upper Boundary) then
17: add $\mathbf{x_i}$ to Outliers
18: **else**
19: add $\mathbf{x_i}$ to Clean Data
20: **end if**
21: **end for**
22: **Return Clean Data, Outliers**

3.5.2 Data visualization after outlier removal using IQR

Figure 3.9 illustrates the visualization of recorded BG values after applying IQR for Participant no. 8 and Participant no. 26. Blue dots represent cleaned data after applying IQR. Figure 3.9 demonstrates that the IQR outlier removal method successfully removes outliers from the recorded data of all participants while preserving the most important BG level data points. This method also ensures that important data points are not removed when cleaning outliers for all participants. The average of all remaining readings is then calculated to determine an analogous BG level for each individual after the outliers are excluded.

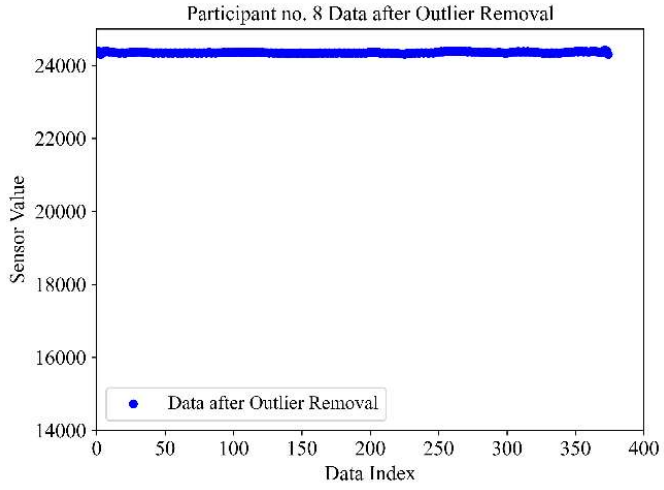

(a)

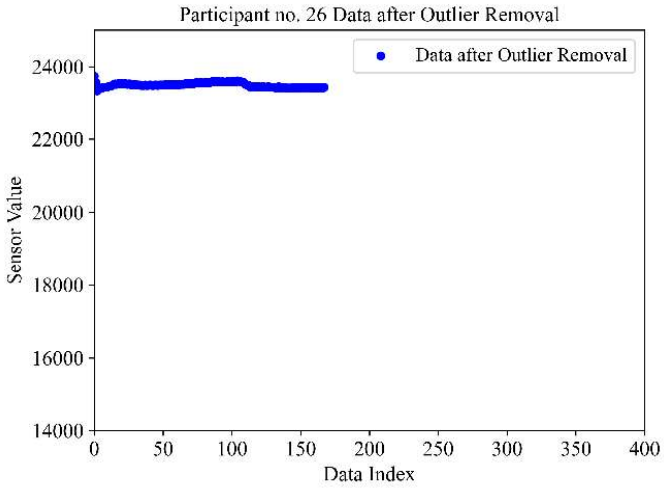

(b)

Figure 3.9: Visualization of recorded BG values after applying IQR for (a) Participant no. 8 and (b) Participant no. 26, blue dots highlighting the data points after outliers' removal.

3.6 Summary

This chapter focuses on generating and preparing a dataset for accurate BG estimation using non-invasive sensing approaches. It describes the design and construction of a one-sensor data-acquisition instrument. A single-sensor device is easier to implement, less complex, and more convenient for patients than a three-sensor device, since only one sensor is used. The state-of-the-art non-invasive device uses capillary glucose as a targeted BG, but we have used serum glucose because it is considered an accurate reading by physicians. The chapter also presents XAI techniques to identify key wavelengths relevant to BG estimation using the iGLU dataset. Finally, the IQR method, a vital data preprocessing technique, is applied to improve data quality and the consistency of BG prediction models. This chapter also shows that a single sensor dataset includes 15 physiological parameters of participants, including sensor values used to estimate BG levels. This dataset includes serum glucose, which can be used as a targeted BG level with ML models.

Chapter 4
Blood Glucose measurement using Machine Learning techniques

4.1 Introduction

This chapter introduces the use of ML techniques for precise, continuous estimation of BG from a non-invasive sensor. Conventional BG monitoring systems, especially invasive ones, are commonly associated with discomfort and limited capacity for continuous monitoring. To overcome these shortcomings, this study examines a data-driven methodology that uses physiological and sensor-based characteristics to develop predictive models for BG estimation. The chapter is devoted to selecting relevant input features, preprocessing the collected data, and applying ML models to BG prediction. Moreover, a Distributed Architecture is designed by splitting the dataset into clinically significant BG ranges, enabling range-specific learning and improved prediction. To address limited data and range variability, statistical data augmentation based on the average SD is applied to enhance the dataset's variability and strength. The effectiveness of the non-invasive BG estimation architecture is assessed using standard metrics, and its performance is compared with that of state-of-the-art models.

4.2 Performance Enhancement of Blood Glucose measurement using Range-Based Data Segmentation

As discussed in section 3.4, Data for this study were collected in two phases: 623 samples were gathered from August to October 2023, and an additional 161 samples were collected in November 2023. The data from the first phase were processed using the IQR method, as described in section 3.5, resulting in 491 cleaned data points.

The experimentation started with the implementation of two DL models for BG estimation: an FCN and a CNN. an FCN and a CNN. Both models were trained and tested on the cleaned data from 491 participants. A total of 15 important features is used to train the models. These features include device readings, gender, age, Sys. BP, Dia. BP, weight, heart rate, height,

duration of diabetes, diabetes history, daily walking steps, sleep duration, sleep quality, smoking habits, and alcohol consumption. Table 4.1 and Table 4.2 contain the detailed layer-wise configurations of the FCN and CNN, respectively.

Table 4.1: FCN architecture with layer-wise detailed configuration

Implementation of FCN		
Layer	**Neurons**	**Learnable parameters**
Dense 1	Input features: 15, neurons: 10	160
Dense 2	10	110
Dense 3	10	110
Dense 4	10	110
Dense 5	10	110
Dense 6	10	110
Dense 7	10	110
Dense 8	10	110
Dense 9	10	110
Dense 10	10	110
Output	1	11
	Total	1,161

ReLU is used as an activation function in both models. Table 4.3 shows the performance analysis of the FCN and CNN on the single-sensor dataset. The results indicate that both models performed poorly, with RMSEs of 46.99 and 59.34 mg/dL, respectively.

Table 4.4 shows the performance assessment of FCN and CNN on a single sensor dataset trained using range-based data segmentation. The experimental findings show that BG estimation performance is much enhanced by range-based data segmentation. Both FC and CNN models exhibit similar accuracy across 90–125 mg/dL, with the CNN performing marginally better in RMSE and mARD. Both models function similarly in the range 126–160 mg/dL, with FC exhibiting somewhat higher relative accuracy. However, CNN performs much better than FC in the BG range 161–250 mg/dL, greatly reducing RMSE, mARD, and MAD owing to its capability to capture complex nonlinear relationships. Overall, the results validate the efficacy of the distributed framework by confirming that

training distinct models on BG range-specific subsets improves prediction accuracy, especially in high-variability zones. Consequently, further research is conducted using a Distributed Architecture [105] to enhance the predictive performance of ML models for BG estimation. However, performance improvements for models are limited due to the small, less diverse dataset. This issue can be addressed by augmenting the data to increase its diversity and size.

Table 4.2: CNN architecture with layer-wise detailed configuration

Implementation of CNN			
Layer	**Filter size/ Neurons**	**Output shape**	**Learnable parameters**
Convolution 1	f= 6, k = 2, i =1	(15, 6)	18
Pooling 1	Max pooling, size: 2	(7, 6)	0
Convolution 2	f= 16, k = 2, i =6	(7, 16)	208
Pooling 2	Max pooling, size: 2	(3, 16)	0
Convolution 3	f= 32, k = 2, i =16	(3, 32)	1056
Pooling 3	Max pooling, size: 2	(1, 32)	0
Dense layer 1	256 neurons	256	8448
Drop Out 1	30 %	256	0
Dense layer 2	128 neurons	128	32896
Drop Out 2	30 %	128	0
Dense layer 3	64 neurons	64	8256
Drop Out 3	30 %	64	0
Dense layer 4	32 neurons	32	2080
Drop Out 4	30 %	32	0
Output	1 neuron	1	33
		Total	52,995

Table 4.3: Performance evaluation of FCN and CNN using Single-sensor dataset

Model	**Data Sample**	**Training**	**Testing**	**RMSE (mg/dL)**
FC	491	393	98	46.99
CNN	491	393	98	59.34

Table 4.4: Performance evaluation of FCN and CNN using Range-Based Data Segmentation

Model	Data Sample	Training samples	Testing samples	RMSE (mg/dL)	mARD%	MAD (mg/dL)
BG range: 90-125 mg/dL						
FC	242	193	49	13.95	11.49	5.80
CNN	242	193	49	13.59	10.48	6.15
BG range: 126-160 mg/dL						
FC	98	78	20	14.93	7.8	7.13
CNN	98	78	20	14.95	8.6	7.09
BG range: 161-250 mg/dL						
FC	72	57	15	30.69	12.3	13.03
CNN	72	57	15	19.72	7.66	7.10

4.3 Feature extraction for Blood Glucose estimation

Further research is conducted using the SHAP method to specify the contributions of the 15 features used for BG estimation in training an FCN and a CNN. The SHAP method is applied to both the FCN and CNN to identify which features are the most and least important for BG estimation. Figure 4.1 and Figure 4.2 illustrate the feature importance as determined by SHAP analysis for the FCN and the CNN, respectively.

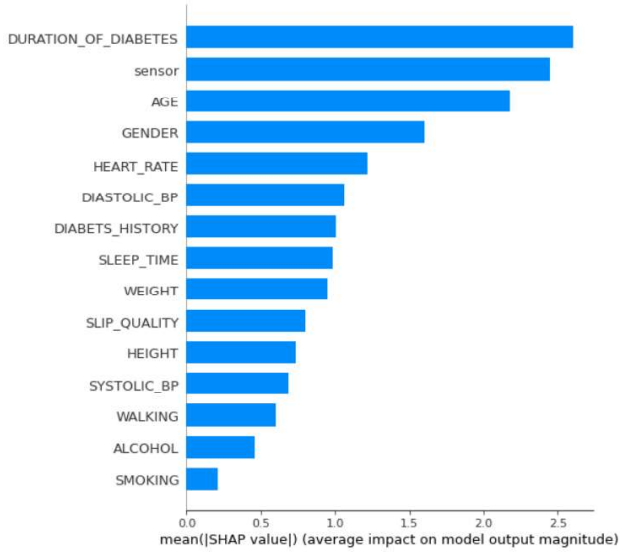

Figure 4.1: Feature importance visualization of the FCN obtained using SHAP, highlighting each input feature's contribution to the model's predictions

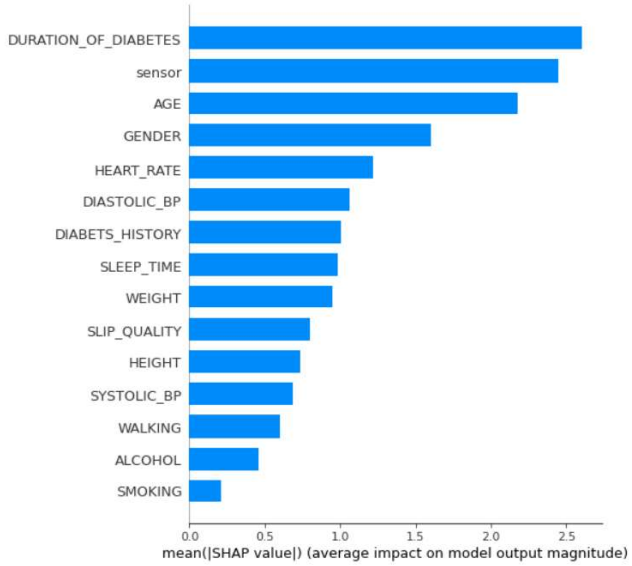

Figure 4.2: Feature importance visualization of the CNN obtained using SHAP, highlighting each input feature's contribution to the model's predictions

The results indicate that the features related to smoking and alcohol have minimal importance and can be excluded from the BG prediction model. Consequently, these two features are removed, and both the FCN and CNN are retrained using the remaining 13 features, maintaining a similar implementation setup as depicted in Section 4.2

Table 4.5: Performance evaluation of FCN and CNN using Range-Based Data Segmentation trained with 13 features

Model	Data Sample	Training samples	Testing samples	RMSE (mg/dL)	mARD%	MAD (mg/dL)
BG range: 90-125 mg/dL						
FC	242	193	49	13.8	10.8	5.88
CNN	242	193	49	11.1	8.85	4.87
BG range: 126-160 mg/dL						
FC	98	78	20	13.45	7.4	5.94
CNN	98	78	20	13.98	7.5	7.18
BG range: 161-250 mg/dL						
FC	72	57	15	33.37	12.3	17.1
CNN	72	57	15	32	12.9	12.75

As the performance comparisons in Table 4.4 and Table 4.5 show, reducing the number of input features has an insignificant effect on the model's accuracy across all BG levels.

Although the CNN achieves higher accuracy with 13 features in the BG range (90-125 mg/dL) (as evidenced by lower RMSE, mARD, and MAD), the FCN model shows no significant improvement in accuracy. Both models have very similar performance with slight differences in the BG range 126-160 mg/dL. Performance differences are slightly more pronounced in the BG range 161-250 mg/dL, although overall trends remain the same, with CNN still performing better than FC.

These findings indicate that the essential predictive information is retained despite feature reduction. Thus, since both sets of features yield similar outcomes, the 13 features can be selected to reduce the model's complexity and computational cost. Therefore, for further research, smoking habits and alcohol consumption are dropped, and 13 important features are finalized. The features, which are used to train the BG estimation model, include age, gender, weight, Sys. BP, Dia. BP, height, heart rate, diabetes history, duration of diabetes, sleep duration, sleep quality, daily walking steps, and device readings. The serum BG collected from laboratory tests serves as the target value.

4.4 Data Augmentation

As discussed in Section 3.5, after data pre-processing, 552 records are used for further research. However, this dataset is limited to training a distributed architecture, which may have contributed to underfitting and lowered the model's effectiveness. To address these issues, a data augmentation stage is incorporated into the architecture to enhance the model's performance. Data augmentation increases the diversity of the dataset and improves the generalisation capability of the ML models. A statistical analysis is performed on the dataset to apply data augmentation to the tabular data properly. The augmented samples are obtained by adding slight variations to each feature, consistent with the observed statistical variability. The perturbations are kept within physiologically realistic ranges to maintain the relationship between the BG reference measurements and the sensor measurements.

Tables 4.6 and 4.7 present a comprehensive statistical analysis of the collected dataset, BG-range-wise, including distributions (minimum and maximum) and central tendency (mean ± standard deviation) for all selected features. The dataset is divided into eight BG intervals (70-90 to 211-230 mg/dL), with an uneven distribution of records, higher concentrations in the lower and mid ranges, and significantly fewer samples in the higher BG ranges. Table 4.6 indicates that all physiological and demographic parameters, such as age, Sys. BP, Dia.

BP, weight, heart rate, and sensor readings are within realistic and clinically acceptable limits across all BG ranges; therefore, the data are reliable.

Table 4.6: BG range wise statistical analysis of recorded features of participants (Min. and max.)

BG range (mg/dL)		70-90	91-110	111-130	131-150	151-170	171-190	191-210	211-230
Records	Count	82	183	113	73	36	32	19	14
Age (yrs)	Min.	21	18	24	26	25	35	30	14
	Max.	79	85	79	76	71	74	72	63
Weight (kg)	Min.	30	38	46	52	42	52	52	25
	Max.	102	113	103	97	95	124	92	82
Height (cm)	Min.	145	142	53	147	147	135	150	150
	Max.	180	185	185	185	180	185	180	178
Sys. BP (mmHg)	Min.	88	80	106	82	69	115	120	87
	Max.	202	221	188	184	190	180	187	147
Dia. BP (mmHg)	Min.	64	50	64	25	41	67	66	62
	Max.	123	131	127	132	117	120	116	108
HR (Bits/min.)	Min.	58	47	58	40	68	69	65	63
	Max.	125	131	139	111	117	107	133	112
Walking (steps)	Min.	1000	200	1000	500	2000	1000	1000	2500
	Max.	9000	10000	9000	8000	8000	5000	8000	6500
Duration of diabetes (yrs)	Min.	0	0	0	0	0	0	0	0
	Max.	30	22	30	45	23	23	15	11
Diabetes history	Min.	0	0	0	0	0	0	0	0
	Max.	2	5	4	5	5	5	5	3
Sleep time (hrs)	Min.	6	3	3	5	4	4	4	6
	Max.	8	10	9	8	8	8	8	8
Sleep quality	Min.	1	0	0	0	0	0	1	0
	Max.	2	2	2	2	2	2	2	2
Sensor	Min.	7262	7641	7421	7434	7160	7246	8910	11638
	Max.	19990	23552	21762	24353	25200	21048	24400	23736
BG (mg/ dL)	Min.	72	91	111	131	151	172	191	212
	Max.	90	110	130	150	170	190	210	230

Table 4.7: BG range wise statistical analysis of recorded features of participants (Mean ± SD)

BG range (mg/dL)		70-90	91-110	111-130	131-150	151-170	171-190	191-210	211-230	Average
Records	Count	82	183	113	73	36	32	19	14	-
Age (yrs.)	Mean ± SD	52.8 ± 15	54.1 ± 12	56 ± 12	55 ± 12	56 ± 11	56 ± 9.7	53.7 ± 11.7	42.8 ± 12.7	53.3 ±12
Weight (kg)		65 ± 14	69 ± 13	70 ± 12	70 ± 10	65 ± 13	72 ± 14	67 ± 10	66 ± 16	68 ± 12
Height (cm)		166 ± 8	166 ± 8	165 ± 13	167 ± 8	164 ± 9	167 ± 10	166 ± 10	168 ± 8	166 ± 9
Sys. BP (mmHg)		134 ± 18	135 ± 18	136 ± 14	136 ± 18	134 ± 21	139 ± 16	137 ± 18	128 ± 16	134 ± 17
Dia. BP (mmHg)		87 ± 11	89 ± 13	88 ± 9	90 ± 15	84 ± 14	90 ± 12	90 ± 12	89 ± 12	88.5 ± 12
HR (Bits/min.)		85 ± 12	83 ± 12	85 ± 12	84 ± 10	86 ± 11	86 ± 8	85 ± 17	86 ± 11	85 ± 12
Walking (steps)		3418 ± 1394	3825 ± 1656	3394 ± 1357	3688 ± 1531	3604 ± 1212	2984 ± 1008	3697 ± 1626	3786 ± 1236	3549 ±1377
Duration of diabetes (yrs)		2 ± 5	3 ± 5	5 ± 7	5 ± 7	7 ± 7	8 ± 8	4 ± 4	3 ± 3	4.65 ± 6
Diabetes history		0 ± 1	0 ± 1	1 ± 1	1 ± 1	1 ± 1	1 ± 1	1 ± 1	0 ± 1	1 ± 1
Sleep time (hrs.)		6.8 ± 1	6.7 ± 1	6.7 ± 1	6.8 ± 1	6.7 ± 1	6.7 ± 1	6.8 ± 1	7.1 ± 1	6.8 ± 1
Sleep quality		2 ± 0	2 ± 1	2 ± 1	2 ± 0	2 ± 0	2 ± 1	2 ± 0	2 ± 1	1.7 ± 1
Sensor		13420 ± 3328	14222 ± 3131	14540 ± 3244	14350 ± 3567	15422 ± 3899	14781 ± 3672	16706 ± 3453	16117 ± 3224	14944 ± 3439
BG (mg/ dL)		85 ± 5	100 ± 6	119 ± 6	140 ± 6	159 ± 5	180 ± 6	201 ± 5	220 ± 6	150 ± 5

Table 4.7 shows stable average values across ranges, while moderate variability in standard deviations for features such as walking steps and sensor readings reflects participant diversity and dataset representativeness. Imbalanced record distribution and small sample sizes in higher BG ranges can negatively impact the performance of range-specific models in a distributed architecture. The SD measures the variability of the observed data across features. To successfully address this, the statistical measures obtained from this analysis are directly applied to the data augmentation process.

Specifically, the SD of each feature for each BG range is used as a reference to generate synthetic samples centred on the mean. This methodology ensures that the augmented information does not destroy the inherent variability of the original data, but instead mimics the existing samples. Therefore, average SD-based augmentation increases data variety, preserves the distribution, and enhances the robustness and generalizability of the BG estimation model across all glucose levels. Algorithm 4.1 presents the data augmentation process using SD on the pre-processed dataset.

Algorithm 4.1 Data augmentation using SD

Input:

Pre-processed dataset $\boldsymbol{D}$

Output:

Augmented dataset $\boldsymbol{D_{augmented}}$

1: Load the pre-processed dataset $\boldsymbol{D}$
2: Divide the dataset into n equal-sized subsets, each subset indicating particular characteristics of the BG range (n = 8).
3: Compute Average SD $(\boldsymbol{\sigma_{average}})$ for each feature
4: For each record in dataset:
   a. Generate $\boldsymbol{k}$ random numbers for the given range using $\boldsymbol{\sigma_{average}}$
   b. For each feature:
      New value = Actual value + Random number
   c. Create new augmented record
   d: Repeat steps a to c such that the total number of data records after data augmentation becomes equal
5: Repeat for all features and all records
6: Append all augmented records to original dataset

$$\boldsymbol{D_{augmented}} = \boldsymbol{D} + \text{Augmented Data}$$

7: end

Table 4.8 provides an outline of the total number of participants and the division of the training and testing data after data augmentation. It presents the distribution of BG data across various BG ranges used to train the architecture. It displays the number of training and testing records at each BG interval between 70 and 230 mg/dL. The nearly equal

numbers of training and testing samples in each BG range indicate that the models will have the opportunity to learn from data across all ranges, minimising the risk of biased results for any specific range. The training and testing samples contain 14,318 and 3,580 records, respectively, for a total of 17,898 records. The data is fairly well-balanced across all BG ranges, ensuring balanced model learning and assessment.

Table 4.8: BG range wise of dataset after augmentation with training and testing records

Sr. no	BG range (mg/dL)	Training records	Testing records
1	70-90	1690	462
2	91-110	1817	440
3	111-130	1788	451
4	131-150	1801	441
5	151-170	1798	450
6	171-190	1830	428
7	191-210	1780	467
8	211-230	1814	441
		14318	**3580**
	Total	**17898 records**	

4.5 Proposed Lightweight Distributed Architecture for BG measurement

As discussed in Section 4.2, a Distributed Architecture is used to increase the predictive accuracy of ML models for BG estimation, and a total of 13 features from section 4.3 are used as inputs to the proposed architecture. Figure 4.3 presents the proposed Distributed Architecture for BG estimation.

The dataset mentioned in Section 3.5 is used, and data augmentation (section 4.4) is applied. After augmentation, all data points are normalized to the range [0, 1] using the Min-Max scaler (Equation 3.2). The new augmented dataset is divided into eight subsets. The first subset contains data from individuals with BG levels between 70 and 90 mg/dL. Subsequent subsets are 91-110 mg/dL, 111-130 mg/dL,…., and 211-230 mg/dL, respectively. Eight regression models are trained and tested separately on these subsets, with each model

focused on a single subset. RM_0 to RM_7 in Figure 4.3 represent regression models trained separately on different BG-range subsets. After that, a pre-classifier is implemented to classify the input data for BG ranges from 70 to 230 mg/dL into eight classes. The subsets represent an eight-class set used to train and test the pre-classifier.

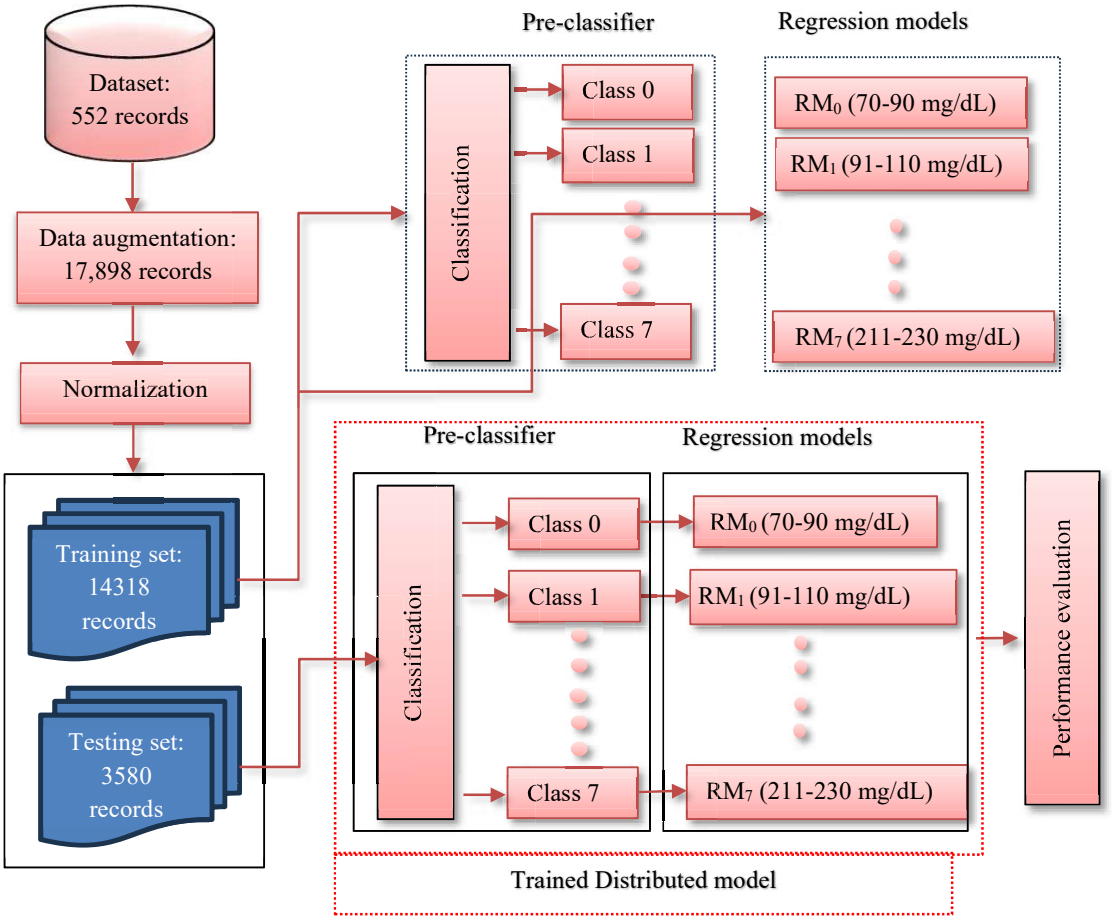

Figure 4.3: Proposed Distributed architecture for BG estimation

When new data enters the proposed architecture, it is first processed by the pre-trained pre-classifier stage, and the most suitable regression model among the eight is identified. The new data is then directed to its selected regression model for BG estimation. Using classification and regression models to estimate BG levels is the newness of the proposed architecture. Several regression and classification models have been implemented and trained for BG estimation. Rigorous experiments are conducted with various ML models to identify the best-suited one for BG estimation.

4.6 Evaluation metrics

4.6.1 Evaluation metrics for pre-classifier

4.6.1.1 Accuracy

Accuracy is one of the measures of the model's overall performance. It is the proportion of correct predictions (positive and negative) of all the predictions.

$$Accuracy = \frac{TP + TN}{TP + FP + TN + FN} \times 100\% \quad (4.1)$$

FP= False Positive, *TP*= True Positive, *FN*= False Negative, *TN*= True Negative

4.6.1.2 Precision

Precision is defined as the number of correctly predicted positive cases divided by the total number of predicted positive cases. Low precision implies reduced false positives.

$$Precision = \frac{TP}{TP + FP} \quad (4.2)$$

4.6.1.3 Recall

Recall refers to the fraction of actual positive cases that are correctly detected. High recall implies fewer false negatives.

$$Recall = \frac{TP}{TP + FN} \quad (4.3)$$

4.6.1.4 F1-score

The harmonic mean of recall and precision is known as the F1-score. It balances accuracy and recall, especially when the data is skewed.

$$F1\ score = 2 \times \frac{Recall\ \times\ RPrecision}{Recall + Precision} \quad (4.4)$$

4.6.2 Evaluation metrics for Regression model

The regression models' performance is measured using RMSE, MAD, and mARD. (Refer to section 3.3.1).

4.7 Performance evaluation and result analysis of Distributed Architecture

MLR, SVR, DT, RF, and FCN are applied to the regression task in this research. RMSE and mARD are measures of regression model performance, along with MAD. Table 4.9 summarizes the regression model results.

Table 4.9: Performance analysis of regression models for BG estimation-direct analysis. Bold highlights the best test results for each model

Metrics	Regression models				
	MLR	**SVR**	**DT**	**RF**	**FCN**
mARD (%)	2.22	1.95	1.26	**1.01**	3.72
MAD (mg/dL)	1.56	1.56	1.17	**0.77**	1.03
RMSE (mg/dL)	3.38	3.2	2.1	**1.78**	2.35

K-NN, DT, SVM, FCN, and RF are used as pre-classifiers. These are measured using accuracy, recall, precision, and F1 score to determine the most appropriate architecture. The evaluation results of the pre-classifiers are given in Table 4.10.

Table 4.10: Performance analysis of the pre-classification models of Distributed Architecture (Bold letters in table highlights the best test results for each model)

Metrics	Pre-classifier				
	KNN	**SVM**	**DT**	**FCN**	**RF**
Accuracy (%)	74.77	80.9	94.7	97.05	**97.9**
Precision	0.74	0.81	0.95	0.97	**0.98**
Recall	0.75	0.81	0.95	0.97	**0.98**
F1 score	0.73	0.8	0.95	0.97	**0.98**

Table 4.9 and Table 4.10 provide the individual performance analyses of regression and classification models to determine the most appropriate models for a distributed architecture. Tables 4.9 and 4.10 indicate that the RF model achieves high accuracy on the dataset. For the performance evaluation of the proposed distributed architecture, the RF model is used for pre-classification and the regression stage.

Table 4.11: Performance evaluation of proposed distributed architecture using RF model

	mARD (%)	MAD (mg/dL)	RMSE (mg/dL)
Distributed architecture	1.51	1.79	6.08

The test data is processed using a pre-trained RF classifier that classifies it into 8 classes. These classified data are then subjected to their respective pre-trained RF regression models for BG estimation. Table 4.11 presents the performance analysis results of this distributed architecture, highlighting the effectiveness of using RF for both pre-classification and regression tasks. The comparison of the results presented in Table 4.3 and Table 4.11 indicates that training the range-based model enhances the effectiveness of the learning models and surpasses a single end-to-end regression model that is trained on the entire glucose range. Additionally, when comparing the results presented in Tables 4.11 and 4.5, the impact of data augmentation is clearly evident. The results indicate that data augmentation reduced the risk of model overfitting and improved the robustness of the developed model by exposing it to a wider range of feature variations.

The proposed distributed architecture uses a pre-classifier to decide which BG range to use for the regression. If the range assignment is incorrect and the error propagates to the regression stage, it will affect the final BG estimate. However, the error will be naturally limited by the design of the proposed framework. In particular, the pre-classifier sorts the BG values into contiguous intervals of about 20 mg/dL, such as 70-90, 91-110, 111-130,..., 211-230 mg/dL. This means that classification errors will likely be found within the relatively narrow glucose intervals, and not across large intervals. Therefore, the propagated estimation error is typically ±20 mg/dL, which helps reduce the effect of pre-classification error on the total estimation error. Moreover, the pre-classifier achieves high classification accuracy, reducing the misclassification rate and making the proposed distributed architecture more robust.

However, the developed non-invasive BG measurement device was tested in a controlled laboratory environment to minimize the effects of external variables. The participants had a range of physiological properties, but the influences of motion artefacts, different skin types (e.g., skin tone and thickness), and temperature and humidity were not examined separately. These factors could affect the sensor's operation in real-world applications. They will be

explored systematically in future work to further evaluate the robustness and feasibility of the proposed device in clinical settings.

4.8 Clarke Error Grid Analysis

The Clarke Error Grid Analysis (CEGA) assesses the predictive performance of different models of BG levels [106]. Zone A refers to the predicted values of the BG that do not exceed the reference value by more than 20 percent. The zone is applied to describe the model, with a separation of predicted and targeted BG levels across five zones: A to E. In Zone B, a predicted BG value is within 20 percent of the target value and does not lead to many inaccurate predictions. The BG range is 70-180 mg/dL, which is within Zone C, but the expected result falls outside this range. Zone E describes instances where the expected result is either above or below 70 mg/dL, depending on whether the targeted value exceeds 180 mg/dL or falls below it. For the model to be beneficial in clinical practice, all anticipated outcomes must fall within Zones A and B.

Figure 4.4 demonstrates the CEGA of Distribution Architecture with an RF pre-classifier and various regression models. It shows that all prediction points lie in Zone A across all models. The analysis demonstrates the clinical applicability of the proposed architecture and the other implemented models.

Among the models evaluated, the RF-based model has the most points near the reference line, indicating the greatest clinical accuracy and the lowest prediction error. The DT and FCN models also exhibit good clinical performance; SVR and MLR have relatively larger deviations from the reference line because of their limited capability to capture nonlinear BG variations.

Importantly, there are no clinically relevant prediction errors in Zones D and E, suggesting a distributed architecture that avoids them. The improvement is believed to be due to the RF pre-classifier, which classifies samples by BG range (20 mg/dL), allowing each regression model to learn BG patterns within that range. The prediction deviation is also limited even if the pre-classifier assigns the wrong neighbouring BG range, thereby ensuring a clinically safe prediction of the BG value. Overall, CEGA results show that the proposed distributed architecture achieves high prediction accuracy and clinical safety for BG estimation.

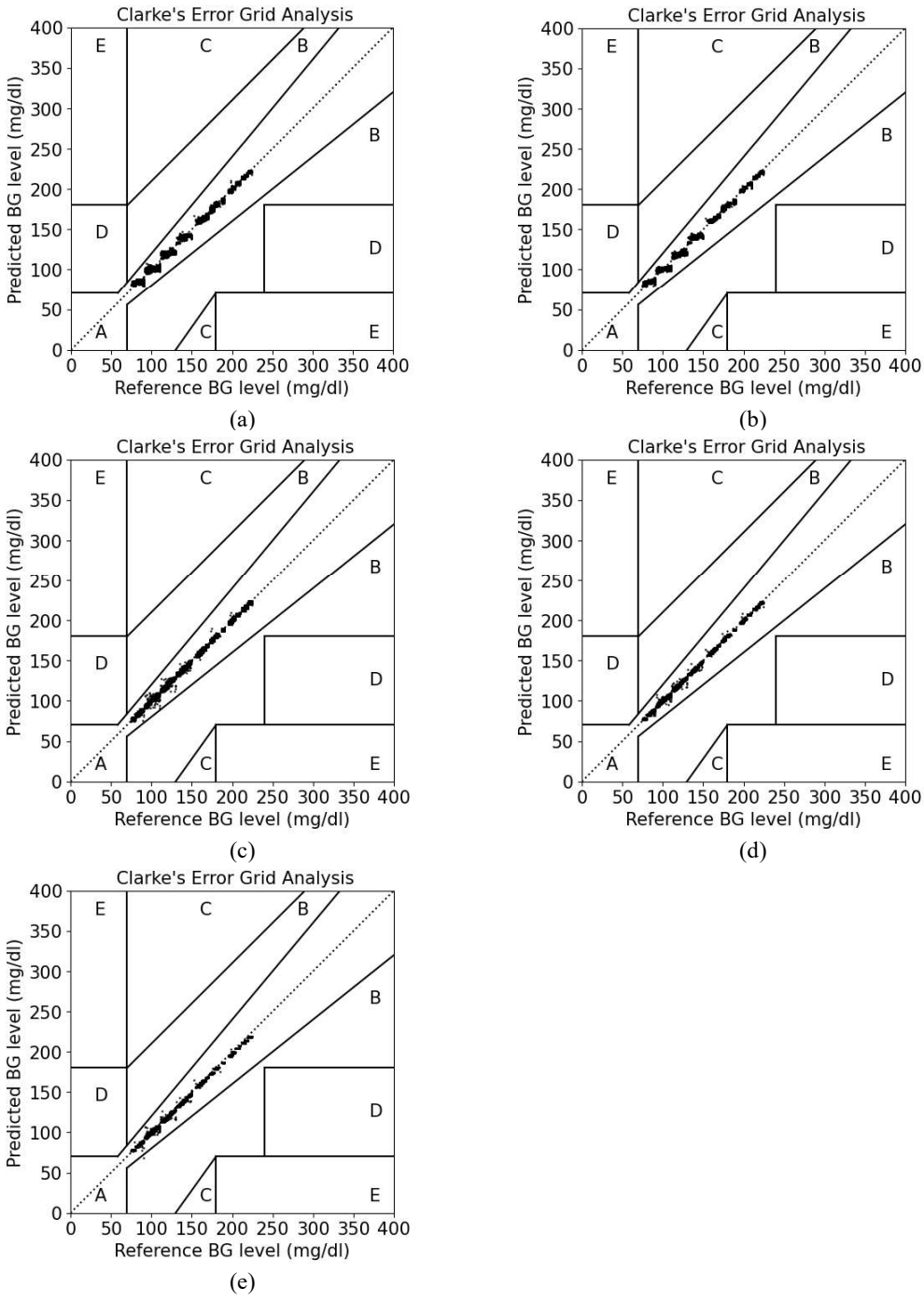

Figure 4.4: CEGA of Distribution Architecture with RF pre-classifier and various regression models (a) MLR (b) SVR (c) DT (d) RF (e) FCN

4.9 Performance analysis of Distributed Architecture with state-of-the-art non-invasive approaches

Table 4.12 presents the performance analysis of Distributed Architecture with state-of-the-art non-invasive approaches. The distributed nature of our architecture allows for localized

data preprocessing. On the contrary, traditional ML methods often fail to account for the physiological noise in human blood samples. With an MAD of 1.79 mg/dL, our model shows an average difference between the predicted glucose values and the actual laboratory reference of less than 2 units. Such a level of accuracy greatly reduces the noise from non-invasive sensors, resulting in high consistency and clinical reliability in the output. This distributed architecture is also effective, as the CEGA indicates that all model outputs are entirely in Zone A, the most accurate clinical result.

Table 4.12: Performance analysis and statistical evaluation of the proposed distributed architecture and state-of-the-art non-invasive approaches

Research works	mARD (%)	MAD (mg/dL)	RMSE (mg/dL)	CEG Analysis	Data records	Measurement sample
Dai et al. 2009 [8]	5.99	-	-	-	in-vivo	blood
Song et al. 2015 [9]	8.3	-	-	Zone A & B	Human	blood
Haxha et al. 2016 [17]	-	-	33.49	Zone A & B	Human	blood
Pai et al. 2018 [21]	3.09	11.5	15.65	Zone A & B	in-vivo	blood
Joshi et al. 2020 [12]	4.86	9.42	13.57	Zone A	Human	blood
Jain et al. 2020 [19]	6.65	12.67	21.95	Zone A & B	Human	blood
Joshi et al. 2022 [13]	5.34	8.3	12.7	Zone A	Human	Capillary & Serum
Sun et al. 2023 [11]	7.31	-	21.06	Zone A & B	Human	blood
Wei et al.2023 [14]		11.33		Zone A & B	Human	blood
Jain et al. 2024 [20]	12.5	-	-	Zone A & B	Human	blood
Proposed work	**1.51**	**1.79**	**6.08**	**Zone A**	**Human**	**blood**

In summary, the proposed distributed architecture achieves better measurement accuracy across all major criteria than earlier studies. This significant improvement can be attributed to the integrated design, in which the pre-classifier and regression models work in tandem to efficiently refine the raw data before producing the final estimate.

4.10 Summary

This chapter introduces an ML-based model of non-invasive BG estimation. This model uses data collected by a non-invasive single-sensor device, along with 12 physiological

features, to estimate BG levels. ML-based model enhances prediction performance through range-based data segmentation and efficient feature extraction. A data augmentation stage is included in the architecture to enhance the model's efficacy and robustness. One of the contributions is the lightweight distributed architecture, in which a pre-classifier determines the BG range, and a regression model is used for estimation. To evaluate the system, standard classification and regression measures, along with the CEGA, are used to ensure clinical accuracy. The proposed method demonstrates reliable performance and outperforms existing non-invasive methods, making it suitable for real-time BG monitoring. However, the BG estimation range is observed to 70-230 mg/dL using a single non-invasive sensor, compared with a three-sensor device.

Additionally, statistically defined limits are used to generate augmented samples, but these may not capture the full physiological range observed in a larger clinical population. Thus, slight errors can creep into the learned distributed architecture. Future studies could overcome this limitation by acquiring a larger, more varied experimental dataset from multiple clinical centres, thereby reducing reliance on data augmentation.

Chapter 5
Blood Glucose forecasting using various learning models

5.1 Introduction

The control of T1D Mellitus (T1DM) depends on proper estimation of BG levels. This chapter details our research on accurate forecasting of future glucose levels, enabling early detection of the risk of hypoglycaemia and hyperglycaemia, which is later used to develop better intelligent decision-support systems for insulin delivery. Achieving precise predictions requires thorough data preprocessing and the use of suitable time-series modelling, as BG measurements are sequential and can vary significantly.

In this chapter, a hybrid Deep Convolutional Recurrent Neural Network (DCRNet) model is outlined, in which the CNN captures local patterns and the LSTM models long-range temporal relationships for precise BG forecasting. To enhance model robustness and convergence, extensive data preprocessing is performed first, including time-series data preparation and standardization. Our results include experiments using both virtual and real patient data. Virtual patient data generated by the UVA/Padova T1D Mellitus simulator (UVA/Padova T1DM) [107], [108] is utilized to train and assess the proposed architecture, along with real patient data from the OhioT1DM dataset [109].

This chapter provides specifics on the architecture design, hyperparameter setup, and training process. To evaluate the performance of the proposed DCRNet, RMSE and Mean Absolute Error (MAE) metrics are used. CEGA is also performed to validate the clinical applicability of forecasting models. Additionally, the efficacy and robustness of the proposed hybrid model for BG forecasting are confirmed through statistical analysis and comparisons with state-of-the-art baseline models.

5.2 Dataset for BG forecasting

5.2.1 In-silico data

The UVA/Padova T1D Simulator [107], [108] is a physiologically realistic glucose/insulin model that captures glucose and insulin dynamics across a broad spectrum of meal and insulin scenarios that are clinically difficult, expensive and ethically problematic to replicate. It enables the creation of a variety of glucose profiles for developing and testing forecasting algorithms under controlled conditions. Eleven simulated subjects in the UVA/Padova T1DM simulator are selected to create a broad dataset for analysing BG forecasting.

The subjects are provided with four meals per day, including breakfast, lunch, snacks, and dinner, each having a baseline CHO value of 35 g, 45 g, 0 g, and 50 g, respectively [110]. To introduce some variation and capture real-world eating habits, the CHO content of each meal is increased by 10 g increments. Breakfast, lunch, snacks, and dinner are set at upper limits of 85 g, 105 g, 30 g, and 120 g, respectively [110]. Each scenario is associated with a time series of 1,440 BG points of one adult during the day. By systematically generating heterogeneous and homogeneous virtual patient data across all meals, 1,344 unique meal condensations are generated and modelled in 11 in silico adult subjects over 24 hours. In addition to BG values, data on corresponding CHO intake and insulin delivery are recorded, enabling the creation of powerful ML models.

Among the eleven subjects, eight are allocated to training and the remaining to testing, so that the models are not tested inappropriately. The importance of the induced scenarios is that they highlight changes in meal composition in the real world, which can vary from low- to high-CHO intake at different meal times. This systematic approach improves on limited or fixed-meal datasets, which expose the model to a wide range of physiological responses, thereby enabling greater generalization. The proposed scenarios introduce variety and exhaustive combinations of meals and are therefore well-suited to representing both normal and extreme conditions; thus, they are most suitable for deriving reliable, clinically pertinent BG prediction models.

5.2.2 Clinical data

To assess clinical applicability, the OhioT1DM (2020 version) [109] dataset is used to evaluate the efficacy of BG forecasting models, which contains CGM data over time from

patients with T1D living their daily lives. This dataset was generated from an 8-week record of 12 participants with T1D. The sample includes information on 5 females and 7 males aged 20-60 years. For 8 weeks, Medtronic Enlite CGM sensors and Medtronic 630G or 530G insulin pumps were used to collect data.

All participants provided data on daily events using a smartphone application and a fitness band. The data consist of insulin doses (both bolus and basal), CGM BG levels every 5 minutes, BG levels after self-monitoring with fingerstick, CHO amounts, sleep, exercise, stress, work, and disease. The dataset also contains heart rate, step count, Galvanic Skin Response, air temperature, and skin temperature, measured every 5-minute interval. The OhioT1DM dataset includes separate training and test records for 12 participants.

Detailed information on the number of training and test records is shown in Table 5.1 [109]. The models have been validated on this independent dataset, thereby demonstrating their ability to generalize to conditions not simulated.

Table 5.1: Detailed information regarding the training and test records of each participant [109]

Sr no.	Participant ID	Gender	Training samples	Test samples
1	540	Male	11947	2884
2	544	Male	10623	2704
3	552	Male	9080	2352
4	567	Female	10858	2377
5	584	Male	12150	2653
6	596	Male	10877	2731
7	559	Female	10796	2514
8	563	Male	12124	2570
9	570	Male	10982	2745
10	575	Female	11866	2590
11	588	Female	12640	2791
12	591	Female	10847	2760

5.3 Data preprocessing

5.3.1 Feature normalization

Time-series data is normalized and time-aligned during data preprocessing. This change stops higher-value input features from taking centre stage, since each feature is scaled to the identical numerical range.

Let:

$$\boldsymbol{X} = [\mathbf{x}_1, \mathbf{x}_2, \ldots, \mathbf{x}_T], \mathbf{x}_t \in \mathbb{R}^n \tag{5.1}$$

$\boldsymbol{X}$ is a multivariate time series, as defined by Equation 5.1, where n is the number of characteristics, and T is the time series length. All input variables (BG, insulin, and CHO consumption) are first scaled using Min-Max normalization (Equation 3.2).

5.3.2 Segmentation and Windowing

The normalized time-series data is converted into a representation of the targeted outputs and inputs. This data preparation involves creating multiple segments from the time-series data, each paired with its intended output. The 30 minutes of recent data (i.e., six previous samples) are utilized as input to the architecture for PHs of 15, 30, and 60 minutes. This is based on the continuous time series, which is sampled every 5 minutes. The value of BG at time t is referred as y_t, where t = the most recent time index. $\mathbf{X_t}$ represents the structure of a given training sample, as illustrated in Equation 5.2 [70].

$$\mathbf{X_t} = [\boldsymbol{x_{t-5}}, \boldsymbol{x_{t-10}}, \boldsymbol{x_{t-15}}, \boldsymbol{x_{t-20}}, \boldsymbol{x_{t-25}}, \boldsymbol{x_{t-30}}] \tag{5.2}$$

where $\boldsymbol{x_{t-i}} = [\mathrm{BG}_{t-i}, \mathrm{CHO}_{t-i}, \mathrm{BOLUS}_{t-i}]$ is the vector of input features at time $t - i$.

Targeted BG values for different PH are expressed in Equation 5.3 [51]:

$$y_{t+PH} = \mathrm{BG}_{t+PH} \tag{5.3}$$

Where $PH \in \{15,30,60\}$ minutes. y_{t+PH} and BG_{t+PH} are the forecasted BG value for PH.

In this way, the mapping of all PHs is learned by the architecture, which can be expressed as shown in Equation 5.4 [51]:

$$f: \mathbf{X}_t \rightarrow y_{t+h} \tag{5.4}$$

The dataset is segmented using a sliding-window approach with a stride of s =1 (overlapping windows) to ensure optimal utilization of the temporal data. The time-series dataset can be segmented and prepared for the proposed architecture using the sliding-window technique, as shown in Figure 5.1. For learning, this approach generates input data by aggregating 6 samples (window size, w = 6). From the time series data, the BG samples at the 3rd, 6th, or 12th positions are considered the targeted BG for PHs of 15, 30, or 60 minutes, respectively. In Figure 5.1, red boxes represent the most recent 30 minutes of input data used by the architecture to forecast BG levels for PH 15 and 30, shown as blue and green boxes, respectively. In this study, BG readings captured every 5 minutes are used for architecture training. Note that Figure 5.1 does not include the section for the 60-minute PH.

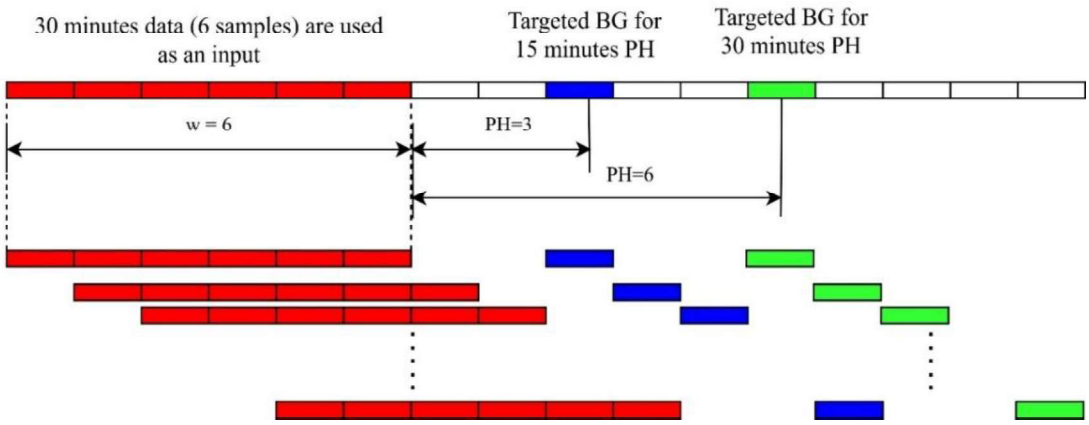

Figure 5.1: Segmentation of time-series data for constructing training and testing datasets corresponding to PH of 15 and 30 minutes

5.4 Proposed DCRNet architecture

For BG-level forecasting, a hybrid DL architecture, DCRNet, has been proposed. The proposed hybrid architecture combines Dilated Convolutional layers to analyze local patterns with an LSTM layer to capture global temporal relationships. DCRNet is evaluated using clinical data from the OhioT1DM dataset and in silico data generated by the UVA/Padova T1DM simulator. DCRNet comprises preprocessing and data preparation, as well as Dilated CNN (DCNN) and LSTM.

The detailed architecture of DCRNet is illustrated in Figure 5.2. G, I, and C depict BG, insulin, and CHO intake in the food. The time-series data is first temporally aligned and then scaled using min–max normalization. The normalized information is fed into the first

layer of DCNN. We have used a 3-layer DCNN. The output from the third layer of the DCNN is fed into an LSTM network, which in turn links to the two dense layers.

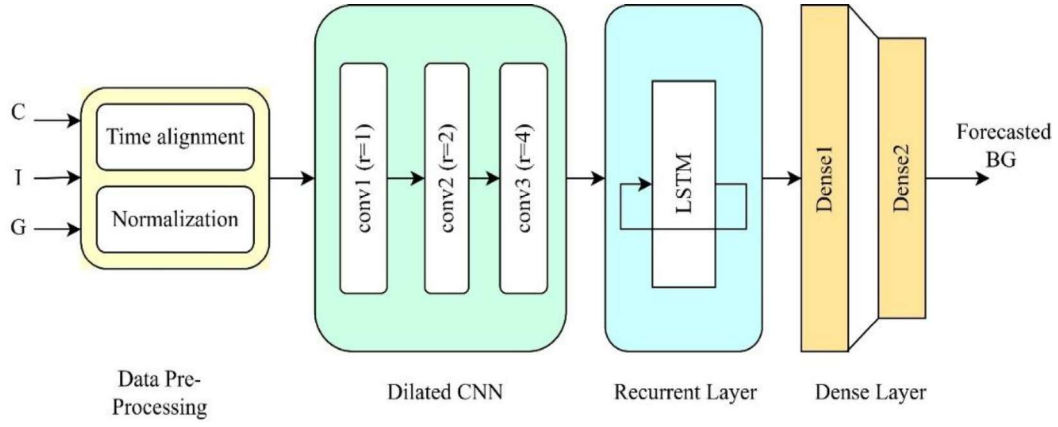

Figure 5.2: Proposed DCRNet architecture includes data preprocessing, three DCNN layers, LSTM layer, and two dense layers

5.4.1 Dilated CNN

In our proposed architecture, Dilated CNN (DCNN) is utilized as it offers a larger effective receptive field, enabling the model to learn more about temporal and spatial patterns in BG. At the same time, a conventional CNN is constrained by smaller receptive fields due to the kernel size and pooling. DCNNs offer deeper, stacked layers (or dilated convolutions) and can gradually increase the receptive field without substantial loss of resolution. This enables more thorough feature extraction from CGM data, thereby enhancing predictive accuracy for complex glucose dynamics. The feature extraction method for DCNN layers is described by Equation 5.5 [102].

$$\mathrm{h}_t^{(l)} = \emptyset\left(\sum_{k=0}^{K-1}\left(W_k^{(l)}\mathrm{W}_{l,k}\,\mathrm{X}_{t-r\cdot k}^{(l-1)} + b^{(l)}\right)\right) \tag{5.5}$$

where, $\mathrm{h}_t^{(l)}$ is the output feature map of the layer l, $W_k^{(l)}$and $b^{(l)}$ is the weights and biases of the kernel, $W_{l,k}$ is the weights of the convolution kernels, r is the dilation rate (1, 2, or 4), k is size of the kernel, and $\emptyset\,(\cdot)$ is the activation function ReLU.

$$\emptyset(x) = ReLU\,(x) = \max(0, x) \tag{5.6}$$

R is the effective receptive field of each layer, which increases with layer number (e.g., 1, 2, 4), as shown in Equation 5.7 [111].

$$R = 1 + (K-1) \cdot \left(\sum_{l=0}^{L-1} \prod_{j=0}^{l} r_j \right) \tag{5.7}$$

where r_j denotes an increasing dilation rate across layers, and K denotes a constant kernel size. Therefore, deeper, more dilated layers capture mid-range structures, whereas local filters in early layers capture fast changes (high-frequency). A small kernel, like a 3x3, is slid over the input in a typical convolution. Adding gaps (zeros) between kernel elements in a DCNN increases the receptive field without increasing computing cost. The dilation rate (r) determines the spacing of the gap. In standard convolution, the dilation rate is constant across layers, e.g., {1,1,1,1...}, whereas in DCNN it increases exponentially, e.g., {1,2,4,8,...}.

The 3 x 3 convolution operation, with dilation factors (r) of 1 and 2, are demonstrated in Figure 5.3 [53]. When the dilation rate (r) is set to 1, the dilated convolution reverts to a standard convolution, as shown in Figure 5.3. In Figure 5.3 (a), the receptive field is 3 × 3 (r = 1), whereas in Figure 5.3 (b), the receptive field expands to 5 × 5 (r = 2).

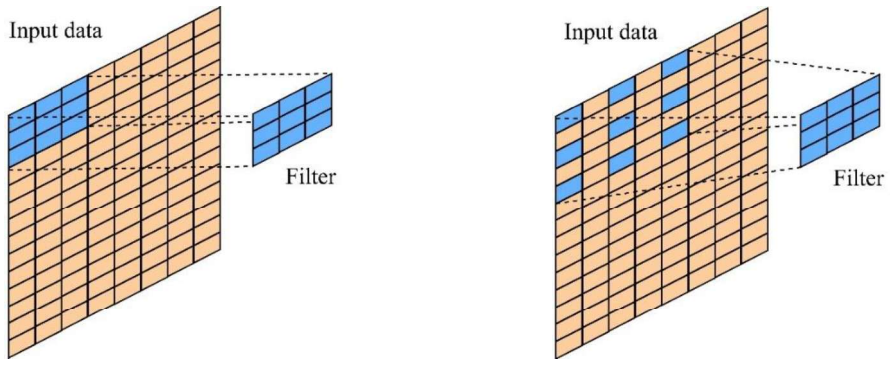

Figure 5.3: DCNN expansion of the receptive field (a) DCNN with r = 1 (b) DCNN with r = 2 [53]

5.4.2 Long Short-Term Memory

Dilated convolutions are effective at extracting local spatial-temporal context; however, they cannot directly replicate long-term sequential dynamics. The DCNN output is fed into an LSTM network to generate a sequence of features simulating global temporal dependencies. An LSTM has three key parts: the input gate, the forget gate, and the output gate. The amount of information stored in the LSTM cell depends on the input gate. The forget gate decides which information to forget, and the output gate integrates and retrieves

information from the input gate, the forget gate, and the present input. The transformed data from this process is then used as input for the following time step.

The LSTM architecture is depicted in Figure 5.4 [112]. $h_t^{(h)}$ represents the hidden state input. $i_t^{(h)}$ and $h_{t-1}^{(h)}$ combine in forget gate and produces f_t, and this result is passed through the sigmoid (σ) function. The forget gate controls which information in the LSTM cell is retained or discarded. The input gate utilizes g_t and $\overline{S_t}$ to generate new data that is stored in the LSTM cell. The new cell state, S_t, is created by adding the product of S_{t-1} and f_t to the product of g_t and $\overline{S_t}$. Finally, the hidden state, $h_t^{(h)}$, is calculated as y_t * $Tanh$ (S_t).

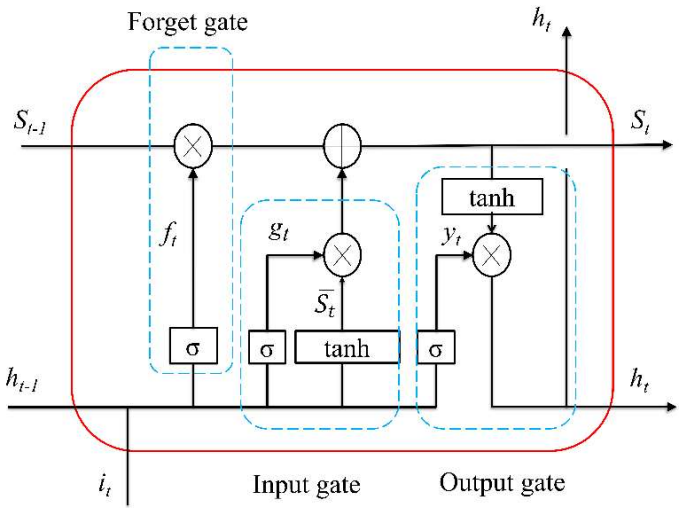

Figure 5.4: The architecture of LSTM for identifying long-range temporal dependencies in time-series data [112]

The LSTM receives the multi-dimensional feature map produced by the last layer of dilated convolutions, $\{h_t^{(L)}\}_{t=1}^{T}$. This level captures long-term relationships in the time series data. At each *t* time step, the LSTM cell's output is computed using Equations 5.8 to 5.13 [62].

$$S_t = g_t * \overline{S_t} + f_t * S_{t-1} \tag{5.8}$$

$$g_t = \sigma\left(W_h \left[h_{t-1}^{(h)} + i_t^{(h)}\right] + b_h\right) \tag{5.9}$$

$$f_t = \sigma\left(W_f \left[h_{t-1}^{(h)} + i_t^{(h)}\right] + b_f\right) \tag{5.10}$$

$$\overline{S_t} = \tanh\left(W_S \left[h_{t-1}^{(h)} + i_t^{(h)}\right] + b_c\right) \tag{5.11}$$

$$h_t^{(h)} = y_t * (\tanh S_t) \tag{5.12}$$

$$y_t = \sigma\left(W_y\left[h_{t-1}^{(h)} + i_t^{(h)}\right] + b_o\right) \tag{5.13}$$

Bias is represented by b_h, b_f, b_s, b_y; weights are represented by W_h, W_f, W_S, W_y; and the Hadamard product is represented by *. To combine features and produce task-specific output, the LSTM output is fed into dense layers.

5.4.3 Dense (Fully Connected) layer

Dense layers use temporal characteristics to produce a final representation suitable for the output task. These layers enable a nonlinear mapping of the LSTM feature space to the output space. Equations 5.14 [51] and 5.15 [51] represent the dense layer, z_n, and the output layer (last dense layer) for the regression task, $\hat{y}$, respectively.

$$z_n = \phi\left(W_n h_T^{(h)} + b_n\right) \tag{5.14}$$

$$\hat{y} = \psi(W_{n+1} z_{n+1} + b_{n+1}) \tag{5.15}$$

Where, $h_T^{(h)}$ denotes the combined LSTM and DCNN outputs, $\phi(\cdot)$ and $\psi(\cdot)$ are the ReLU and linear activation function, respectively, and $b_n, b_{n+1}, W_n, W_{n+1}$ are trainable biases/ weights.

The output of DCRNet, $\hat{y}$, is illustrated as Equation (5.16):

$$\hat{y} = f(X'; \Theta) = \psi(W_n\, \phi(W_{n+1}\, LSTM(Conv_{d_L}^{(L)} \circ \cdots \circ Conv_{d_1}^{(1)}(X')) + b_n) + b_{n+1}) \tag{5.16}$$

where X' represents the pre-processed multivariate sequence of input, and Θ is the trainable parameters.

5.4.4 Optimization and training

The model is optimized by tuning its parameters to achieve the lowest possible loss and better predictive performance. The aim is to identify the best parameter set $\Theta = \{W, b\}$ that maps the target outputs to the given input data.

In regression problems, the loss function is typically the MSE, as shown in Equation 5.17 [33]:

$$MSE = \frac{1}{M}\sum_{i=1}^{M}(y_i - \hat{y}_i)^2 \tag{5.17}$$

Where, y_i is the original target value for the i^{th} sample, $\hat{y}_i$ is the forecasted value for the i^{th} sample, and M denotes the sample size of the dataset.

The optimization is performed using the Adam optimizer, an adaptive method that dynamically adjusts the learning rate for each parameter during training. The formulas for the parameter update rule are Equations 5.18 through 5.21 [35]:

$$m_t = \beta_1 m_{t-1} + (1-\beta_1) g_t \tag{5.18}$$

$$v_t = \beta_2 v_{t-1} + (1-\beta_2) g_t^2 \tag{5.19}$$

$$\hat{m}_t = \frac{m_t}{1-\beta_1^t}, \hat{v}_t = \frac{v_t}{1-\beta_2^t} \tag{5.20}$$

$$\Theta_{t+1} = \Theta_t - \eta \frac{\hat{m}_t}{\sqrt{\hat{v}_t} + \epsilon} \tag{5.21}$$

where $g_t = \nabla_{\Theta_t} MSE$ is the gradient at iteration t, β_1, β_2, and ϵ are hyperparameters of Adam, and η is the learning rate. These equations are used to train the network from the beginning to convergence.

5.5 Modelling Local and Global Dependencies in Glucose Dynamics

A key benefit of the DCRNet architecture is that it combines the strength of DCNN and LSTM modules to model both short-term and long-term time dependencies effectively. Whereas local dependencies show short-term changes in glucose as a result of meals or insulin events, global dependencies show long-term changes as a result of physiological patterns. As seen in Equation 5.22, dilated convolutional layers extract local features using limited receptive fields focused on time t, producing localized feature maps $h_t^{(L)}$:

$$h_t^{(L)} = f_{CNN}(x_{t-r:t}) \tag{5.22}$$

where the effective temporal receptive field, represented by r, is modulated by the dilation rate r_l. These feature maps represent short-term relationships and measure multiscale

temporal variations in the input signal. Equation 5.23 illustrates how the LSTM simulates long-term dependencies by integrating the CNN feature sequence $\{h_1^{(L)}, \ldots, h_T^{(L)}\}$ across time.

$$z_t = f_{LSTM}(h_{1:t}^{(L)}) \tag{5.23}$$

Here, z_t represents the LSTM output, which retains information over distant time steps and captures the overall temporal context.

5.6 Complete architecture of DCRNet for BG forecasting

The overall process carried out by the algorithm, beginning with the input of multivariate features, and ending with the forecasting, is represented in Equation 5.24:

$$X_{1:t} \overset{f_{Pre}}{\rightarrow} X'_{1:t} \overset{f_{CNN}}{\rightarrow} H_{1:t}^{(L)} \overset{f_{LSTM}}{\rightarrow} L_{1:t} \overset{f_{Dense}}{\rightarrow} \hat{y}_t \tag{5.24}$$

The time-series input is used as a multivariate with n features (CHO intake, glucose, and insulin), is represented by $\mathrm{X}_{1:t} \in \mathbb{R}^{T \times n}$. The normalized input is denoted as $X'_{1:t}$.

Algorithm 5.1 Proposed DCRNet (DCNN-LSTM) Based BG Forecasting

Input:
Multivariate time-series data $\boldsymbol{X_{1:t}}$
Output:
Forecasted BG value $\boldsymbol{\hat{y}_t}$
Steps:
Initialize model parameters θ
Preprocessing
for each feature $\boldsymbol{x}$ in $\boldsymbol{X_{1:t}}$ **do**
  Compute $\boldsymbol{x\_min}$ and $\boldsymbol{x\_max}$
  Normalize, $\boldsymbol{x'} \leftarrow (\boldsymbol{x - x\_min}) / (\boldsymbol{x\_max - x\_min})$
end for
Normalize input data, $\boldsymbol{X'_{1:t}}$
Short-term Temporal Feature Extraction using DCNN
$\boldsymbol{H_{1:t}^{(L)}} \leftarrow$ CNN $(\boldsymbol{X'_{1:t}})$
Long-term Dependency Capture using LSTM
$\boldsymbol{L_{1:t}} \leftarrow$ LSTM $(\boldsymbol{H_{1:t}^{(L)}})$
$\boldsymbol{\hat{y}_t} \leftarrow$ Dense $(\boldsymbol{L_{1:t}})$
Model Training
while stopping criterion not met **do**
  Compute loss:
  Loss $\leftarrow (\boldsymbol{y_t - \hat{y}_t})^2$
Update θ using Adam optimizer
end while
return $\boldsymbol{\hat{y}_t}$

The result of the last layer of the DCNN is represented by $H_{1:t}^{(L)}$, while the output from the LSTM network is denoted as $L_{1:t}$. The final output of the proposed DCRNet is represented by $\hat{y}_t$. This illustration shows the hierarchical process for normalizing multivariate input data and predicting final glucose levels using a DCNN, LSTM, and dense layers. The proposed generalized BG forecasting, DCRNet, as previously described, is summarized as in Algorithm 5.1.

5.7 Architectural design for models used in BG forecasting

Algorithm 5.2 illustrates the DCRNet algorithm we implemented for BG forecasting. The proposed DCRNet uses insulin, meal CHO intake, and CGM readings as inputs to ensure a fair comparison with existing models. The recent six samples of CGM readings are used to forecast BG. First, the input sequence is normalized using Min-Max normalization to enhance training stability.

Algorithm 5.2 Our implemented DCRNet

Input:
Input sequence $\boldsymbol{X_{1:t}}$

Output:
Forecasted BG value $\boldsymbol{\hat{y}_t}$

1: Initialize training data $\boldsymbol{X_{1:t}}$
2: Calculate normalized input:
3: Compute $\boldsymbol{X\_min_{1:t}}$ and $\boldsymbol{X\_max_{1:t}}$ for input features
4: $\boldsymbol{X'_{1:t}} \leftarrow (\boldsymbol{X_{1:t}} - \boldsymbol{X\_min_{1:t}}) / (\boldsymbol{X\_max_{1:t}} - \boldsymbol{X\_min_{1:t}})$
5: Layer 1 = Dilated Conv1D ($\boldsymbol{X'_{1:t}}$, filters=8, $\boldsymbol{r}$ = 1)
6: Layer 2 = Dilated Conv1D (Layer 1, filters=16, $\boldsymbol{r}$ =2)
7: Layer 3 = Dilated Conv1D (Layer 2, filters=32, $\boldsymbol{r}$ =4)
8: $\boldsymbol{L_{1:t}}$ = LSTM (Layer 3, cells=64)
9: Dense 1 = Dense ($\boldsymbol{L_{1:t}}$, units=128)
10: Drop 1 = Dropout (Dense 1, rate=0.30)
11: Dense 2 = Dense (Drop 1, units=64)
12: Drop 2 = Dropout (Dense 2, rate=0.30)
13: $\boldsymbol{\hat{y}_t}$ = Dense (Drop 2, units=1) // Final regression output
14: Compute Loss = MSE ($\boldsymbol{\hat{y}_t}$, $\boldsymbol{y_t}$)
15. Apply Adam Optimizer to minimize Loss
16. Update network weights via backpropagation
17: **Return** $\boldsymbol{\hat{y}_t}$

In the first step, the input sequence is normalized to improve training stability using Min-Max normalization. The normalized data is then fed into 3 Dilated Conv1D layers with 8, 16, and 32 filters and dilation rates of 1, 2, and 4, respectively, to learn multi-scale temporal features. These learned features are then fed into an LSTM layer with 64 memory cells

designed to capture the long-term temporal relationships in the glucose sequence. The LSTM output is flattened and fed into two FC layers with 128 and 64 neurons, respectively, with 30% dropout after each dense layer to prevent overfitting. Lastly, there is a single-neuron output layer with a linear activation function that predicts the next BG reading. It is trained with the MSE loss function and the Adam optimizer, which helps the model learn efficiently and make accurate BG predictions.

In addition to the DCRNet, MLR, RF, DT, XGBoost, AdaBoost, FCN, CNN, DCNN, Simple RNN, and LSTM are implemented to enable better performance analysis. The corresponding hyperparameter configurations of the implemented models are provided in Table 5.2. No specific hyperparameter adjustment is necessary for the MLR model. The Gini index serves as the splitting criterion for the DT to assess the quality of the partition. Ten estimators and the Gini index are utilized for split evaluation in the RF model. To provide more precise and stable learning, XGBoost is configured with 100 estimators and a lower learning rate of 0.1, whereas the AdaBoost model uses a learning rate of 1 with 50 estimators.

The learning rate is a hyperparameter that controls the magnitude of parameter updates (weights) during each training iteration. It determines the step size used during the minimization of the loss function. The learning rate controls the trade-off between convergence speed and model accuracy. For all DL models, 0.001 is used as a learning rate.

Table 5.2: Hyperparameter configurations for MLR, RF, DT, XGBoost and AdaBoost

Hyperparameter	**Models**				
	MLR	**DT**	**RF**	**AdaBoost**	**XGBoost**
Gini index used	-	Yes	Yes	-	-
Learning rate	-	-	-	1	0.1
Estimators	-	-	10	50	100

Table 5.3 shows the layer-wise configuration of the FCN. It contains the layer name, the number of neurons (n), and the number of learnable parameters for each layer. The FCN takes in a sequence of 6-time steps and 3 features, and is initially trained with a dense layer of 10 neurons to represent the nonlinear transformation of the input features. Five more dense layers follow, each with 10 neurons, progressively extracting higher-level feature

representations. To avoid overfitting and increase the model's generalisation capability, dropout layers are alternatively placed after every 20% and 30% of the dense layer neurons. Finally, a single-neuron output layer with a linear activation function yields the predicted BG value. The total number of trainable parameters in the complete FCN architecture is 631, making it lightweight and computationally efficient.

Table 5.3: FCN architecture with layer-wise detailed configuration

Implementation of FCN		
Layer	**Neurons**	**Learnable parameters**
Dense 1	Time step: 6, neurons: 10	70
Drop Out 1	20%	-
Dense 2	10	110
Drop Out 2	30%	-
Dense 3	10	110
Drop Out 3	20%	-
Dense 4	10	110
Drop Out 4	30%	-
Dense 5	10	110
Drop Out 5	20%	-
Dense 6	10	110
Drop Out 6	30%	-
Output	1	11
	Total	631

Table 5.4 shows the layer-wise configuration of the CNN and the Simple RNN. It contains the layer name, number of filters (f), kernel size (k), input features (i), number of cells (c), number of neurons (n), and the number of learnable parameters for each layer. The CNN model consists of two Conv1D layers with 6 and 16 filters, respectively, and Max Pooling layers to reduce the number of features and computational complexity. An FCN with 128 and 64 neurons is used to extract features, which are then passed through a dropout layer to mitigate overfitting; the dropout rate is set to 30% after each dense layer. Finally, the output layer, consisting of a single neuron, predicts the BG level. This architecture has 10,747

learnable parameters. The Simple RNN model consists of two recurrent networks with 64 and 32 units, respectively, to capture temporal relationships in BG sequences. Learned features are passed through two dense layers, each with 16 and 8 neurons, respectively, with 20 % dropout after each layer. The model has 8,129 learnable parameters. The computation of learnable parameters in a Simple RNN layer is:

$$\text{Parameters of RNN layer} = ((c + i) \times o) + b_0 \tag{5.25}$$

Where, c = hidden cell, i = number of input features, and o = output of hidden cell.

Table 5.4: Layer-wise detailed configuration of CNN and Simple RNN architecture

Implementation of CNN and Simple RNN							
CNN				**Simple RNN**			
Layer	***f*/ *k*/ *i*/ *n***	**Output shape**	**Learnable Parameters**	**Layer**	***c*/ *i*/ *n***	**Output shape**	**Learnable Parameters**
Convolution 1	f= 6, k = 2, i =3	(6,6)	42	**Recurrent 1**	c = 64, i =3	(6,64)	4352
Pooling layer 1	Max pooling, size: 2	(3,6)	0	**Recurrent 2**	c = 32, i = 64	32	3104
Convolution 2	f= 16, k = 2, i =6	(3,16)	208	**Dense layer 1**	n = 16	16	528
Pooling layer 2	Max pooling, size: 2	(1,16)	0	**Drop out**	20%	16	0
Dense layer 1	n = 128	128	2176	**Dense layer 2**	n = 8	8	136
Drop out	30%	-	-	**Drop out**	20%	8	0
Dense layer 2	n = 64	64	8256	**Output**	n = 1	1	9
Drop out	30%	-	0	**-**	-	-	-
Output	n = 1	1	65	-	-	-	-
Total			10,747	**Total**			8,129

Table 5.5: Layer-wise detailed configuration of DCNN and LSTM architecture

Implementation of DCNN and LSTM							
DCNN				**LSTM**			
Layer	***f*/ *k*/ *i*/ *n* / *r***	**Output shape**	**Learnable Parameters**	**Layer**	***c*/ *i*/ *n***	**Output shape**	**Learnable Parameters**
Convolution 1	f= 8, k = 2, i =3, r = 1	(6, 8)	56	**LSTM 1**	c = 64, i = 3	(6, 64)	17408
Convolution 2	f= 16, k = 2, i =8, r = 2	(6, 16)	272	**LSTM 2**	c = 32, i = 64	(6, 32)	12416
Convolution 3	f= 32, k = 2, i =16, r = 2	(6, 32)	1056	**LSTM 3**	c = 16, i = 32	16	3136
Dense layer 1	n = 128	128	24704	**Dense layer 1**	n = 64	64	1088
Drop out	30%	-	-	**Drop out**	20%	-	-
Dense layer 2	n = 64	64	8256	**Dense layer 2**	n = 32	32	2080
Drop out	30%	-	-	**Drop out**	20%	-	-
Output	n = 1	1	65	**Dense layer 3**	n = 16	16	528
-	-	**-**	-	**Drop out**	20%	-	-
-	-	**-**	**-**	**Output**	n = 1	1	17
Total			34,409	**Total**			36,673

Table 5.5 shows the layer-wise detailed configuration of DCNN and LSTM. The DCNN is composed of three dilated Conv1D layers, with 8, 16, and 32 filters, a kernel size of 2, and dilated rates of 1, 2, and 4, respectively, to extract multi-scale temporal features from the input sequence. The extracted features are fed into two dense layers with 128 and 64 neurons, respectively, and 30% dropout is applied after each layer. The DCNN has 34,409

learnable parameters. The LSTM model consists of three stacked LSTM layers, each having 16, 32, and 64 memory units, which can represent both short-term and long-term temporal dependencies in the input sequence. The learned features are passed through three dense layers with 64, 32, and 16 neurons, respectively, and 20% dropout after each layer for better generalisation. The LSTM architecture has 36,673 learnable parameters. Table 5.6 shows the layer-wise detailed configuration of DCRNet and learnable parameters. In all implementations, the Adam optimizer is utilized, and ReLU is used as the activation function. The input dimension and the number of hidden units determine the number of learnable parameters in an LSTM layer. Due to four gating mechanisms, the parameter count is four times that of a standard recurrent layer, enabling the model to capture long-term temporal dependencies effectively.

Table 5.6: Layer-wise detailed configuration of DCRNet architecture

Implementation of DCRNet			
DCRNet			
Layer	f/ k/ i/ n / c/ r	**Output shape**	**Learnable Parameters**
Convolution 1	f= 8, k = 2, i =3, r = 1	(6, 8)	56
Convolution 2	f= 16, k = 2, i =8, r = 2	(6, 16)	272
Convolution 3	f= 32, k = 2, i =16, r = 2	(6, 32)	1,056
LSTM	c = 64, i =32	(6, 64)	24,832
Dense layer 1	n = 128	128	49,280
Drop out	30%	-	-
Dense layer 2	n = 64	64	8,256
Drop out	30%	-	-
Output	n = 1	1	65
Total			83,817

The computation of learnable parameters in a LSTM layer is:

$$\text{Learnable parameters of LSTM layer} = 4[((c + i) \times o) + b_0] \quad (5.26)$$

Where, c = hidden cell, i = number of input features, b_0 = bias, and o = output of hidden cell.

Figure 5.5 illustrates the layer-wise architecture of the DCRNet for BG forecasting, including the input-output shapes, dilation rates, filter sizes, activation functions, numbers of neurons, and dropout rates.

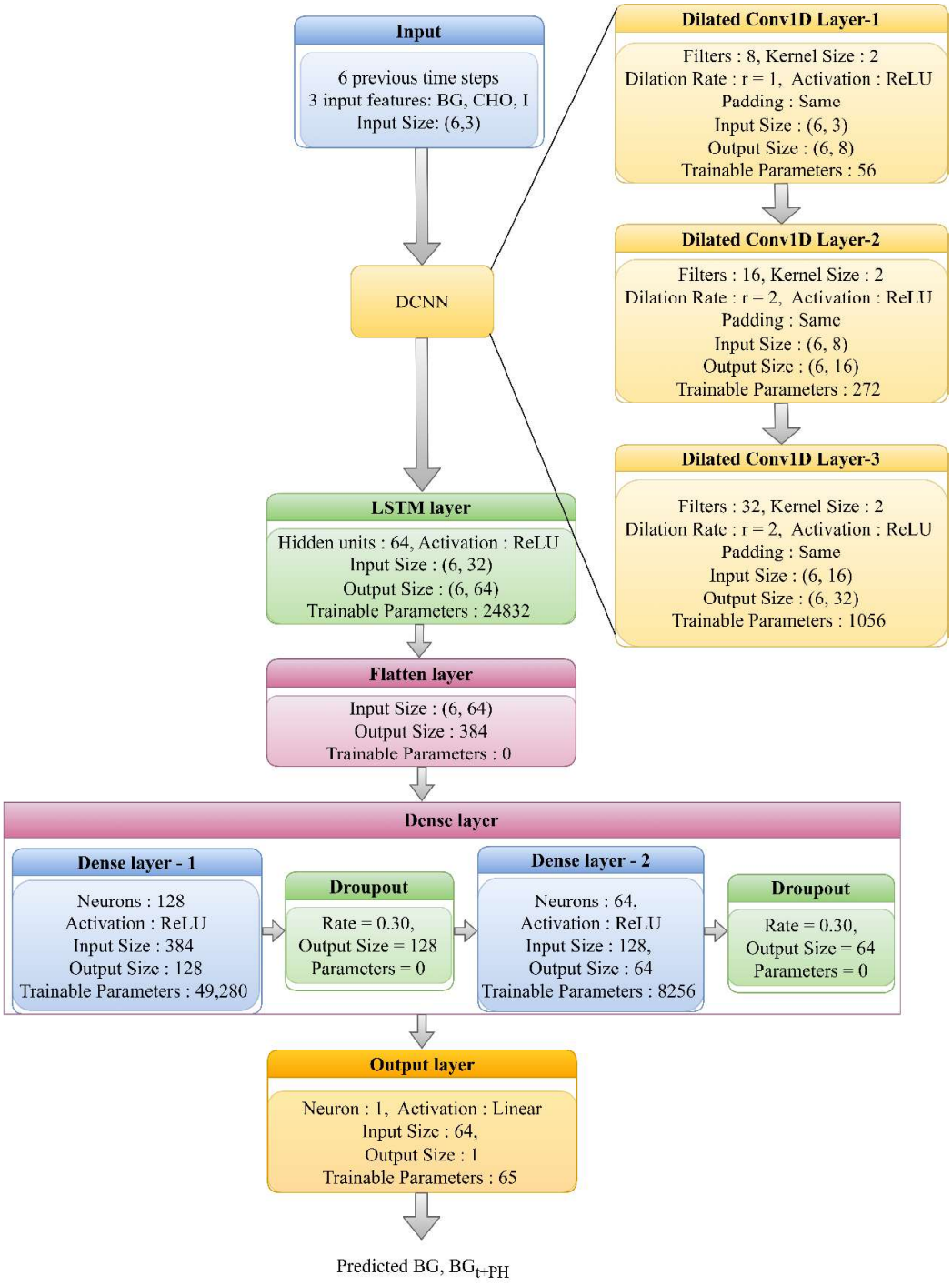

Figure 5.5: Layer-wise architecture of the DCRNet

5.8 Evaluation metrics

5.8.1 Root Mean Square Error

RMSE measures the difference between the actual and predicted BG values. RMSE is computed using Equation 3.3 [53].

5.8.2 Mean Absolute Error

The mean of the absolute errors between the predicted and actual observed outputs is measured by the Mean Absolute Error (MAE) metric. MAE is calculated using Equation 5.27 [33],

$$MAE = \frac{1}{m}\sum_{k=1}^{m}\left|F_k - \widehat{F_k}\right| \tag{5.27}$$

where, F_k = Targeted output, $\widehat{F_k}$ = Predicted output, m = Total prediction samples.

5.9 Performance evaluation of BG forecasting models on virtual dataset of UVA/Padova T1DM simulator

Table 5.7 shows the prediction performance of the proposed DCRNet models, along with conventional ML and DL models, at PHs of 15, 30, and 60 minutes, measured by RMSE (mg/dL) and MAE (mg/dL) on the virtual dataset. The reported metrics are calculated on the full test set to assess each model's general forecasting ability.

For the 15-minute PH, MLR has the best predictive capability, with an RMSE of 3.06 mg/dL and an MAE of 1.57 mg/dL, whereas AdaBoost has the highest prediction error, with an RMSE of 11.09 mg/dL and an MAE of 9.85 mg/dL. LSTM (RMSE: 7.37 mg/dL, MAE: 5.44 mg/dL) outperforms CNN and Simple RNN by better learning the temporal dependency of glucose sequences. The RMSE of 2.87 mg/dL and MAE of 2.11 mg/dL from the DCNN demonstrate its best performance among all existing models, with its dilated convolutions enabling it to learn multi-scale temporal features. The proposed DCRNet achieves an RMSE of 3.42 mg/dL and an MAE of 2.11 mg/dL, which are similar to those of DCNN and MLR. Though DCRNet is less effective than DCNN at this short prediction time, it offers better feature representation through its hybrid architecture and remains competitive in prediction accuracy.

Prediction errors from conventional ML models increase with the forecasting horizon for the 30-minute PH. The RMSE for MLR is 6.24 mg/dL, which is lower than that of other models. XGBoost, RF, and DT record RMSE values of 6.95 mg/dL, 7.16 mg/dL, and 8.19 mg/dL, respectively, which are higher than MLR. In terms of stand-alone DL models, the LSTM model (RMSE: 7.76 mg/dL, MAE: 5.29 mg/dL) is more effective than CNN (RMSE: 8.36 mg/dL) and Simple RNN (RMSE: 8.87 mg/dL), as it has a better ability to learn long-term temporal dynamics. The best stand-alone performance is still achieved by DCNN, with an RMSE of 5.54 mg/dL and an MAE of 3.19 mg/dL. The proposed DCRNet achieves an RMSE of 6.45 mg/dL and an MAE of 4.47 mg/dL, which are slightly higher than those of DCNN.

Table 5.7: Comparative performance analysis of BG forecasting models using in-silico subjects

Model	Metrics					
	RMSE (mg/dL)	MAE (mg/dL)	RMSE (mg/dL)	MAE (mg/dL)	RMSE (mg/dL)	MAE (mg/dL)
	PH=15 minutes		PH=30 minutes		PH=60 minutes	
MLR	3.06	1.57	6.24	4.01	17.55	12.25
DT	4.39	2.12	8.19	4.86	21.5	12.59
RF	3.84	1.76	7.16	4.26	19.19	11.29
AdaBoost	11.09	9.85	17.19	15.74	31.05	27.07
XGBoost	4.07	2.72	6.95	4.64	18.11	12.93
FCN	10.29	7.93	11.00	7.8	20.14	12.8
CNN	9.82	7.04	8.36	5.34	17.88	10.73
Simple RNN	7.25	6.21	8.87	6.77	23.27	17.24
LSTM	7.37	5.63	7.76	5.29	17.56	11.15
DCNN	2.87	2.11	5.54	3.19	17.88	11.72
DCRNet (proposed)	**3.42**	**2.11**	**6.45**	**4.47**	**17.73**	**11.78**

The performance difference between models becomes even more noticeable at the 60-minute PH. The RMSE measures prediction error, with a lower value indicating better performance. The prediction error has been measured using RMSE, with the lowest value for MLR at 17.55 mg/dL and the highest for AdaBoost at 31.05 mg/dL. However, the performance of FCN (RMSE: 20.14 mg/dL) and Simple RNN (RMSE: 23.27 mg/dL) drops

sharply as PH increases. In contrast, LSTM exhibits stable long-term forecasting performance, with an RMSE of 17.56 mg/dL and an MAE of 11.15 mg/dL, indicating effective memory-based sequence learning. The results for DCNN are RMSE 17.88mg/dL and MAE 11.72mg/dL, which demonstrate that spatial feature extraction alone is insufficient to capture long-term glucose dynamics. The proposed DCRNet achieves an RMSE of 17.73 mg/dL and an MAE of 11.78 mg/dL, indicating that it performs slightly better than the best standalone DL models and maintains the same performance across all PHs.

The results of the three DL architectures suggest that the LSTM model is successful in modelling long-term temporal dependence. In contrast, the other two models are less efficient at extracting local patterns of glucose variation. Due to the use of dilated convolutions, DCNN can learn local and multi-scale temporal features, yielding the smallest prediction errors at short and medium PHs. DCRNet fuses the benefits of both architectures, learning local temporal properties and learning long-term sequential properties simultaneously. Although the errors of DCNN are slightly lower than at the 15-minute PH, and the RMSE of LSTM is marginally better than DCNN at the 60-minute PH (17.56 mg/dL vs. 17.73 mg/dL), DCRNet provides consistent performance across all three PHs.

5.10 Performance evaluation of BG forecasting models on OhioT1DM real subjects' dataset

The prediction accuracy of conventional ML, DL, and the proposed DCRNet models for the OhioT1DM dataset is shown in Table 5.8, for PHs of 15, 30, and 60 minutes. To obtain subject-independent evaluation, all training samples from the 12 subjects were pooled to form a new training set, and the corresponding test samples were pooled to form a new test set. This evaluation strategy provides a more valid measure of the model's generalisation across a wide range of people.

Conventional ML models exhibit moderate predictive performance for 15-minute PH. The RMSE values obtained by MLR and RF are 13.10 and 18.64 mg/dL, respectively, while the RMSE value obtained by DT is 18.64 mg/dL. The ensemble models do not perform as well as the other models, with AdaBoost achieving the highest RMSE of 32.05 mg/dL, suggesting that the model is less effective at predicting BG levels. The standalone DL models perform best, with an RMSE of 12.80 mg/dL and an MAE of 8.13 mg/dL for the

DCNN model, whereas the LSTM model shows comparatively higher prediction errors. The proposed DCRNet achieves the lowest RMSE of 12.57 mg/dL and MAE of 7.90 mg/dL, thereby further enhancing prediction accuracy. The improvement over DCNN is small but shows that combining dilated convolution with LSTM enables better learning of local glucose changes and temporal dependencies, resulting in improved short-term forecasting performance.

Table 5.8: Comparative performance analysis of BG forecasting models using the OhioT1DM dataset

Model	Metrics					
	RMSE (mg/dL)	**MAE (mg/dL)**	**RMSE (mg/dL)**	**MAE (mg/dL)**	**RMSE (mg/dL)**	**MAE (mg/dL)**
	PH=15 minutes		**PH=30 minutes**		**PH=60 minutes**	
MLR	13.1	8.42	22.19	15.60	35.84	27.03
DT	18.64	11.68	31.14	21.33	49.31	36.25
RF	13.1	8.3	21.82	15.11	35.51	26.36
AdaBoost	32.05	24.85	37.5	29.71	44.75	36.08
XGBoost	13.38	8.72	22.24	15.7	35.36	26.53
FC	26.07	19.80	36.56	26.91	37.49	28.56
CNN	38.94	37.77	33.22	25.85	40.08	31.59
Simple RNN	16.6	11.94	23.6	16.88	40.16	29.87
LSTM	14.17	9.50	21.21	14.46	35.6	26.31
DCNN	12.80	8.13	20.83	14.28	34.30	25.36
DCRNet (proposed)	**12.57**	**7.9**	**20.72**	**14.13**	**34.41**	**25.50**

A longer forecasting interval increases prediction errors across all models for the 30-minute PH. The LSTM model with a standalone recurrent architecture achieves an RMSE of 21.21 mg/dL and an MAE of 14.46 mg/dL, surpassing the Simple RNN, which achieves an RMSE of 23.60 mg/dL and an MAE of 16.88 mg/dL. The superior performance of LSTM indicates its effectiveness in modelling the long-term temporal dependencies in glucose time-series data. Despite the promising results, the DCNN, with an RMSE of 20.83 mg/dL and an MAE of 14.28 mg/dL, still achieves a high level of prediction accuracy. As a result, the proposed DCRNet achieves the highest overall performance, with an RMSE of 20.72 mg/dL and an MAE of 14.13 mg/dL, outperforming all conventional ML and standalone DL models.

These findings demonstrate the efficacy of the hybrid architecture in capturing both glucose dynamics and long-term trends, thereby enhancing medium-term prediction accuracy.

The difficulty of prediction increases substantially for a 60-minute PH, and the performance of most conventional ML and DL models also drops substantially. Compared with conventional methods, standalone DL methods exhibit noticeable degradation, while the other methods (MLR, RF, DT, AdaBoost, and XGBoost) show significant prediction error. FC, CNN, Simple RNN, and LSTM achieve RMSE values of 37.49, 40.08, 40.16, and 35.60 mg/dL, respectively, with corresponding MAE values of 28.56, 31.59, 29.87, and 26.31 mg/dL. Although LSTM is more accurate than other standalone recurrent architectures at maintaining long-term temporal information, it remains less accurate than DCNN and DCRNet. The proposed DCRNet outperforms DCNN in terms of RMSE (25.50 mg/dL) and MAE (25.36 mg/dL), with differences of only 0.11 mg/dL and 0.14 mg/dL, respectively. The small difference indicates that the proposed hybrid model maintains prediction accuracy comparable to the best standalone model while remaining stable across forecasting horizons.

The three DL architectures are clearly complementary, as seen in their comparison. LSTM is well-suited to model long-term temporal dependencies; however, it is relatively ineffective at modelling local glucose variation patterns, leading to higher prediction errors, especially at shorter PHs. The use of dilated convolutions is effective at capturing local and multi-scale temporal features and works well across all three PHs, while also being implemented efficiently by DCNN. DCRNet combines the merits of DCNN and LSTM, learning discriminative local features and long-term sequential dependencies simultaneously. As a result, DCRNet achieves the best performance at 15-minute and 30-minute prediction time horizons and is very competitive at 60-minute, with a small margin over DCNN.

More impressively, the proposed hybrid architecture consistently outperforms the standalone LSTM in BG prediction error across all PHs on the real OhioT1DM dataset, demonstrating that incorporating DCNN feature extraction with recurrent temporal modelling significantly enhances BG forecasting in an end-to-end fashion, without requiring retraining across different PHs. This real-world dataset showed that the learned DCRNet could generalise well across subjects, extracting essential physiological and temporal glucose patterns, thereby making it a good candidate for practical continuous BG prediction applications. DCRNet facilitates predicting BG levels in individuals with T1D, enabling

timely interventions to regulate glucose and prevent complications associated with hyperglycaemia and hypoglycaemia.

The proposed DCRNet was trained and validated by two independent experiments. The model was trained and evaluated on the UVA/Padova simulator dataset for the first experiment, and the OhioT1DM real-world dataset for the second experiment. Therefore, the model is not a transfer learning model trained on simulated data and applied to clinical data. This comparison of results from the two datasets demonstrates the robustness of the proposed architecture in both controlled simulations and real clinical cases. Compared to simulated data, the glucose-insulin dynamics are more complex in the real world, as reflected in the OhioT1DM dataset, and this likely explains the relatively higher prediction error, which is attributable to physiological variability, sensor noise, missing measurements, more irregular daily activities, and patient-specific behavioural differences.

5.11 Clarke Error Grid Analysis for DCRNet

Multiple ML and DL models are tested in this study, including MLR, DT, RF, XGBoost, AdaBoost, FCN, CNN, and Simple RNN. However, only LSTM, DCNN, and the proposed DCRNet model are analysed using CEGA. The best overall forecasting performance, in terms of RMSE and MAE, across all PHs (15, 30, and 60 minutes) is obtained with these three architectures. However, these results do not provide the clinical applicability and safety of these models. CEGA assesses the clinical accuracy and safety of a prediction. It is used on the best models to determine whether they are clinically acceptable for insulin dose decisions.

Figure 5.6 illustrates the CEGA results of LSTM, DCNN, and DCRNet for PHs 15, 30 and 60 minutes. It can be seen that for the 15-minute PH, all three models are highly clinically accurate, with the majority of prediction points in Zone A. All models make almost all predictions within the clinically acceptable Zones A and B: 97.22% in Zone A and 2.36% in Zone B for DCRNet; 97.32% in Zone A and 2.27% in Zone B; 95.37% in Zone A and 4.05% in Zone B. DCRNet performed almost as well as DCNN, and much better than LSTM.

For PH 30-minute forecasting, it becomes more difficult, so the percentages in Zone A decreased across all models. The best precision is obtained by the proposed DCRNet, which yielded 88.97% predictions in Zone A and 9.34% in Zone B. Compared to these, DCNN recorded an 88.55% accuracy in Zone A and 9.49% in Zone B, while LSTM recorded a

higher drop with 82.57% in Zone A and 14.50% in Zone B. These results show that DCRNet maintains clinically accurate predictions, outperforming LSTM and performing slightly better than the standalone DCNN.

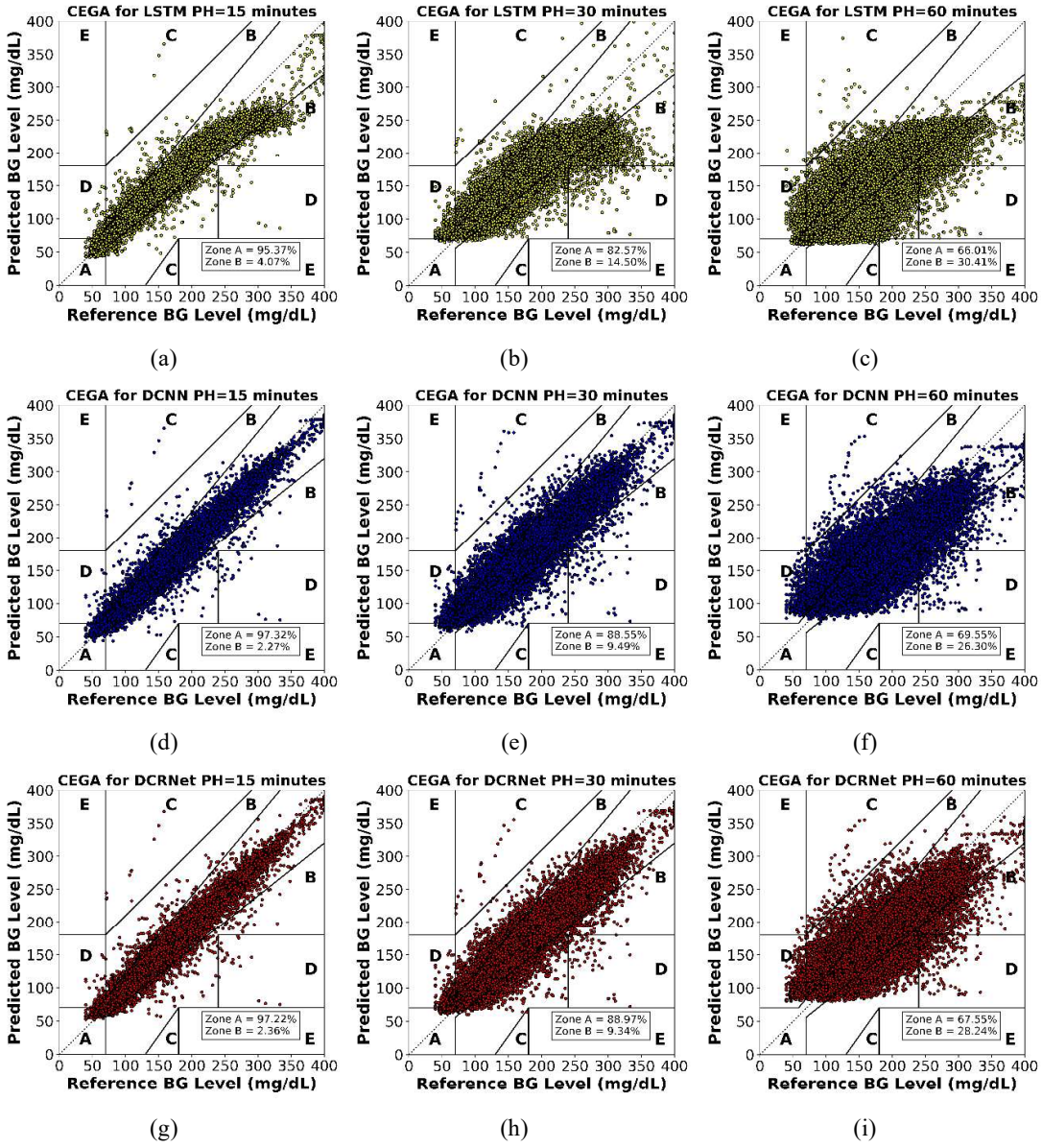

Figure 5.6: CEGA for (a) LSTM PH=15, (b) LSTM PH=30, (c) LSTM PH=60, (d) DCNN PH=15, (e) DCNN PH=30, (f) DCNN PH=60, (g) DCRNet PH=15, (h) DCRNet PH=30, (i) DCRNet PH=60

Prediction uncertainty increased further for the 60-minute PH, leading to additional decreases in Zone A's accuracy. However, the proposed DCRNet still outperforms LSTM and is competitive with DCNN, achieving 67.55% accuracy in Zone A and 30.24% in Zone B. For DCNN, the percentages are 69.55% and 26.30%; for LSTM, they are 66.01% and

31.41%. It is noteworthy that at all three PHs, virtually all prediction points (97% of predictions) fell within the clinically acceptable Zones A and B, and a small number of points fell within the clinically undesirable Zones C, D and E. It shows that the proposed DCRNet consistently produces clinically reliable glucose predictions suitable for insulin therapy support, and it has been proven to be an effective fusion of the temporal learning capability of LSTM with the local feature extraction ability of dilated convolutional layers.

5.12 Comparative analysis of DCRNet with existing models

Table 5.9 presents a comparative analysis of the DCRNet architecture against existing models for PHs at 15, 30, and 60 minutes, evaluated using RMSE (mg/dL) and MAE (mg/dL). To ensure a fair comparison, only studies that use 6 or 12 subjects from the OhioT1DM dataset and report results for 30- and 60-minute PHs are considered. The given approach is significantly more effective than state-of-the-art models, especially for predicting glucose levels for the short PH.

Table 5.9: Comparison of proposed DCRNet architecture and existing models for 15, 30 and 60 minutes PH

Research works	Input feature used	No. of subjects	PH=15		PH=30		PH=60	
			RMSE	MAE	RMSE	MAE	RMSE	MAE
Dudukchu et al. 2021 [54]	CGM	12	-	-	21.9	15.86	35.10	-
Dudukchu et al. 2021 [55]	CGM	12	-	-	21.54	15.39	-	-
Cioppa et al. 2023 [67]	CGM, insulin CHO intake	6	-	-	21.34	-	-	-
Giancotti et al. 2024 [60]	CGM	6	-	-	20.48	14.59	34.16	25.54
Nemat et al. 2024 [72]	CGM	12			20.21	14.36	34.66	25.89
Nemat et al. 2024 [72]	CGM, insulin CHO intake, Physical activity	12	-	-	20.76	14.56	34.85	25.60
Proposed DCRNet	**CGM, insulin CHO intake**	**12**	**12.57**	**7.9**	**20.72**	**14.13**	**34.41**	**25.50**

The proposed architecture demonstrates the ability to capture rapid glucose changes with impressively low error (RMSE=12.57 mg/dL, MAE=7.90 mg/dL) at a PH of 15 minutes, unlike previous research, which reported no results. Furthermore, for a 30-minute PH, the

proposed DCRNet achieves the lowest MAE (14.13 mg/dL) and a competitive RMSE (20.72 mg/dL), indicating improved short-term forecasting accuracy and enhanced overall predictive performance.

The decreases in RMSE and MAE are noteworthy compared with those reported by Dudukchu et al. [54] and Cioppa et al. [67]. Additionally, the performance is still in line with the best values reported by Nemat et al. [72] and Giancotti et al. [60]. The proposed architecture performs comparably to or slightly improves upon state-of-the-art approaches, suggesting steady, long-term predictive capability, and the discrepancies between the models at the 60-minute PH are negligible.

The study demonstrates that DCRNet maintains computational efficiency while outperforming recent hybrid models. The comparison highlights how effectively dilated convolutional layers capture features at multiple scales. It explains how LSTM is important for modelling long-term glucose patterns, as it improves performance across a range of PHs. These results demonstrate the proposed architecture's clinical usefulness and resilience in predicting BG. In conclusion, DCRNet can accurately predict BG for 15-, 30-, and 60-minute PHs in both virtual and real individuals. This facilitates the application of DCRNet in real-world settings where accurate forecasting of proactive diabetes treatment is required.

5.13 Statistical Analysis of proposed model and baseline and Its Significant Implications

For the 60-min PH, a statistical analysis comparing the baseline and the proposed DCRNet is performed (Table 5.10). The comparison verifies the model's performance by identifying computational challenges and the clinical use of BG forecasting models. The time a trained model takes to generate a response (prediction) to a given input sample is called inference latency. It represents the model's effectiveness in real-time and is commonly expressed in milliseconds. The model's bias is indicated by the mean prediction error, which is the average difference between the actual and predicted values. The t-statistic shows how far the sample results deviate from the "null hypothesis". The p-value shows the likelihood of obtaining the observed results assuming the null hypothesis is true. A low p-value (usually < 0.05) indicates that the outcome is statistically significant and not due to chance.

Except for DT ($p>0.005$), all implemented models had $p < 0.001$. The proposed DCRNet demonstrates computational efficiency and statistical robustness with an inference latency

of 0.054 ± 0.004 s, mean prediction error of 1.87 mg/dL ($t = 9.694$, $p < 0.001$), and 83,817 trainable parameters. Confidence tests revealed that DCRNet maintains a small but consistent variance (< 2 mg/dL), which is statistically visible but clinically inconsequential, whereas most baseline models showed considerable bias. CL insulin delivery's minimal latency (<0.02% of the 5-min sampling window) and low processing requirements validate its practicality for real-time operation.

Table 5.10: Comparative statistical analysis of the proposed and baseline models for 60-minute PH, emphasizing inference latency, mean prediction error, results of significance tests (t-statistic and p-value), and learnable parameters

Models	Inference (s)	Mean prediction error (mg/dL)	p-value	t-statistic	Learnable parameters
MLR	0.0001 ± 0.00002	0.86	< 0.001	4.372	19
DT	0.0007 ± 0.0002	0.43	> 0.05	1.57	9,85,271
RF	0.0041 ± 0.0004	0.73	< 0.001	3.643	3,50,45,656
AdaBoost	0.0036 ± 0.0006	15.576	< 0.001	66.132	750
XGBoost	0.0004 ±0.0001	1.08	< 0.001	5.454	1600
FCN	0.048 ±0.003	9.43	< 0.001	46.319	631
CNN	0.32 ±0.06	23.36	< 0.001	110.270	10,747
Simple RNN	0.3 ± 0.04	23.64	< 0.001	114.12	8,129
LSTM	0.3 ± 0.05	14.29	< 0.001	68.903	36,673
DCNN	0.049 ± 0.007	2.435	< 0.001	12.675	34,409
DCRNet (proposed)	**0.054 ± 0.004**	**1.87**	**< 0.001**	**9.694**	**83,817**

Furthermore, the model's convolutional and recurrent design inherently lowers the impact of transient sensor noise, and its sequence-based training makes it easier to adjust to patient-specific glucose dynamics. Besides statistically significant accuracy, these characteristics indicate that DCRNet is clinically and practically ready for implementation in wearable or embedded insulin administration systems. Deployment-wise, the DCRNet model offers a reasonable trade-off between accuracy and computational performance and can be used in CGM systems for real-time and embedded applications. The number of learnable parameters in the proposed DCRNet is relatively small at 83,817, compared to many modern

deep learning models. The lightweight Conv1D and LSTM layers are used to build a compact architecture that consumes less memory and computational overhead while maintaining accuracy. The offline training phase for DCRNet is time-consuming but only performed during model development. After that, only the inference stage is performed in real-time operation, which has much lower computational and memory requirements. Hence, the proposed DCRNet can be considered as a convenient and efficient algorithm for real-time blood glucose prediction. The proposed approach can forecast BG in real time and can be used in wearable or embedded devices, as it predicts each test sample in milliseconds during inference. These characteristics indicate that the proposed model can be implemented in practice on low-power hardware platforms used in CGM and CL insulin administration devices.

When it comes to missing sensor data, the proposed CGM system does its best to minimize its impact during BG measurement. The non-invasive device continuously collects the BG Data, and then a 1-minute average of the sensor data is calculated and fed to the proposed distributed architecture for BG estimation. This averaging process helps mitigate the effects of occasional missing or noisy sensor measurements, leading to a more consistent estimate of BG. The missing sensor data is therefore effectively addressed before the forecasting stage and has a negligible effect on the performance of the DCRNet, since the estimated current BG value is continuously fed into the DCRNet for BG forecasting. In addition, prediction accuracy can be further improved by incorporating periodic retraining or transfer learning across different physiological conditions. These aspects will be studied in future to improve the practicality of the proposed system.

5.14 Summary

The proposed DCRNet can accurately forecast both short- and long-term BG levels from CHO, glucose, and insulin data. By combining a DCNN for local feature extraction and an LSTM for capturing long-term temporal dependencies, the model balances short-term responsiveness with long-term stability, yielding higher predictive accuracy than current techniques. These results indicate that it can increase real-time glucose management and tailored therapies. Among those that are yet to be resolved is a generalization across a wide range of physiological conditions and demographics. However, challenges remain in ensuring robust generalization across diverse physiological conditions and patient populations. Further, DCRNet will be validated on larger, more heterogeneous datasets,

optimizing the architecture for real-time use, enabling low-cost computing through hardware-efficient implementations, and developing adaptive personalization techniques in future studies.

Chapter 6
Proposed intermittent insulin bolus therapy for T1D patients

6.1 Introduction

Effective glycaemic control remains an important part of the treatment of T1D, but it is still hard to obtain optimal control without elevating the risk of hypoglycaemia. Our research presents a new Intermittent Insulin Bolus (IIB) therapy that uses advanced DL to make proactive decisions. This component is the most innovative part of our proposed CGM system. The main part of this method is the DCRNet, a specially designed Deep Convolutional Recurrent Neural Network that predicts future BG levels. The approach calculates insulin doses based on forecasted BG values rather than current BG. The proposed therapy is assessed for clinical efficacy using evaluation metrics such as Time Above Range (TAR), Time Below Range (TBR), and Time in Range (TIR). Furthermore, the safety and stability of the control logic are evaluated using specialized risk indices and the Control-Variability Grid Analysis (CVGA) to maintain a balanced approach between patient safety and aggressive glucose correction.

6.2 Forecast -based Insulin bolus calculation

The current glucose measurement (G_t) is used in the traditional insulin dosage algorithm to calculate the bolus insulin. Equation 6.1 is used to determine the bolus insulin for mealtime (BI_S) using current glucose value [81].

$$BI_S = \frac{CHO}{CR} + \frac{G_t - G_T}{CF} \tag{6.1}$$

where CHO stands for the meal's carbohydrate content in grams (g), CR in gram/Unit (g/U) and CF in mg/dL per Unit (mg/dL/U) stand for the insulin-to- carbohydrate ratio and Correction Factor, respectively. CR and CF are the individuals' specific characteristics, and usually, doctors use a trial-and-error approach to adjust these two factors. The target BG level is shown by G_T (mg/dL), while the current BG level is indicated by G_t (mg/dL).

Reactive control often leads to postprandial hyperglycaemia or hypoglycaemia due to the inherent delay between insulin delivery and its peak metabolic effect, which typically occurs 45-75 minutes later. To minimize this delay, the proposed method substitutes the current glucose value in the insulin dosing formula with a 60-minute-ahead forecast of the glucose level. This approach enables prediction of glucose levels that coincide with peak insulin activity, facilitating anticipatory control. The future BG concentration predicted using DCRNet for 60-minute PH is used to calculate the insulin dose in the proposed IIB therapy. The forecasting model with shorter PHs can also be utilised in the proposed therapy to increase prediction accuracy, but this reduces the insulin intervention time. There is always a trade-off between prediction accuracy and PHs. However, as per glucose-insulin dynamics, a 60-minute PH is best suited for the proposed therapy. Equation 6.2 presents our proposed formula for calculating insulin boluses (MBI_S).

$$MBI_S = \frac{CHO}{CR} + \frac{\widehat{BG_{t+60}} - G_T}{CF} \tag{6.2}$$

Where, $\widehat{BG_{t+60}}$ represents output of forecasting model for PH=60 minutes.

The DCRNet was extensively tested on simulated and real data to improve safety prior to implementation in the therapeutic framework. However, sometimes prediction errors can lead to mis recommendation of insulin. So, the proposed therapy is a decision support tool and has only been tested in the UVA/Padova simulator. However, in real clinical use, additional safety features should be added, including prediction-confidence assessment, a dose constraint, and confirmation by the current CGM measurement prior to insulin delivery, to reduce the risk of unintended insulin dosing.

6.3 Simulation framework for IIB therapy and experimental design

A multi-factorial simulation environment is created to analyse the effectiveness and strength of the proposed forecast-based IIB therapy. The US Food and Drug Administration (FDA)-approved T1DM simulator is used in this research and involves 10 virtual adults. To precisely evaluate the proposed therapy under varied physiological demands and behavioural uncertainties, subjects are tested across combinations of CHO amounts and insulin-injection scenarios. A continuous period of 7 days is used in each simulation trajectory to capture both intra-day variability and inter-day glycaemic stability.

6.3.1 Mathematical Modelling of the Scenario Space

To make the experiment reproducible and specify it unambiguously, the simulation setup is represented as a discrete, multi-dimensional state space. The experiment can be characterized by the following tuple: (V, C, S, ε) where the elements refer to dimensions of the study.

6.3.1.1 Virtual subject set

The set of individuals that make up the population of virtual adult cohorts in the UVa/Padova simulator is finite:

$$V = \{ v_1, v_2, v_{3,} \dots \dots \dots ., v_{10}\} \tag{6.3}$$

6.3.1.2 Main Meal scenarios

Scheduled daily meals: [Breakfast, Lunch, Snack, Dinner] are represented by the meal vector. $M = \{M_1, M_2, M_3, M_4\}^T$, respectively. Each meal scenario's CHO intake is specified as a vector in grams. The set of all meal scenarios $C = \{c_1, c_2, c_3, c_4\}$ is defined by the following profiles:

- Low CHO (c_1): $[35, 45, 10, 50]^T$
- Moderate CHO (c_2): $[45, 65, 15, 70]^T$
- High CHO (c_3): $[55, 90, 15, 90]^T$
- Very High CHO (c_4): $[65, 100, 20, 100]^T$

Figure 6.1 illustrate the daily timeline of meal taken during a day.

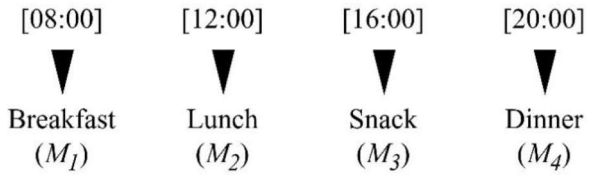

Figure 6.1: Daily timeline of meal taken during a day

6.3.1.3 Insulin insertion Sub-Scenarios

A control matrix of each sub-scenario is defined to evaluate the impact of insulin insertion before each meal. Let $\boldsymbol{S_n}$ be the vector for sub-scenario $n \in \{a, b, c, \ldots . j\}$, defined as:

$$\boldsymbol{S_n} = [\Delta t_1, \Delta t_2, \Delta t_3, \Delta t_4, M_{Extra}]^T \quad (6.4)$$

Where, $\Delta t_m \in \{0, 15, 30, No\ insulin\}$ indicates the time prior (in minutes) to the meal M_m at which the bolus is administered and $M_{Extra} \in \{0,20\}$ indicates the CHO intake (in grams) taken at 22:00 to avoid a hypoglycaemia event at midnight. Table 6.1 illustrates the complete set of insulin insertion sub-scenarios S_n. $\Delta t_1, \Delta t_2, \Delta t_3$, and Δt_4 represents the time of insulin taken by subjects before breakfast, lunch, snack, and dinner, respectively.

6.3.1.4 Total Scenario Space

The product of the meal scenarios and the timing sub-scenarios is the total set of scenarios considered for a given subject:

$$\varepsilon = C \times S_n \quad (6.5)$$

The total scenario space is 40 because it has 4 meal scenarios and 10 timing sub-scenarios. In turn, the 10 virtual subjects, with these 40 scenarios applied over the 7 days, yield 2,800 days of simulated clinical data.

Table 6.1: Illustration of different sub scenarios containing insulin insertion time before each meal

$\boldsymbol{S_n}$	Insulin taken time before meal (minutes)				
	$\boldsymbol{\Delta t_1}$	$\boldsymbol{\Delta t_2}$	$\boldsymbol{\Delta t_3}$	$\boldsymbol{\Delta t_4}$	$\boldsymbol{M_{Extra}}$
$\boldsymbol{S_a}$	0	0	0	0	0
$\boldsymbol{S_b}$	30	30	30	15	0
$\boldsymbol{S_c}$	15	15	15	15	0
$\boldsymbol{S_d}$	30	30	30	30	0
$\boldsymbol{S_e}$	30	30	30	30	20
$\boldsymbol{S_f}$	30	30	No insulin	30	0
$\boldsymbol{S_g}$	30	30	No insulin	30	20
$\boldsymbol{S_h}$	30	30	No insulin	15	20
$\boldsymbol{S_i}$	30	15	No insulin	15	20
$\boldsymbol{S_j}$	15	15	No insulin	15	20

6.3.1.5 Algorithm for simulation Setup for Forecast-Based IIB Therapy

To compute the BG trajectories in an orderly manner and assess the efficiency of the proposed IIB therapy, the simulation is implemented using the nested loop process outlined in Algorithm 6.1.

Algorithm 6.1 Simulation Setup for Forecast-Based IIB Therapy

Input:

- Set of $\boldsymbol{V}$ virtual subjects ($\boldsymbol{V = 10}$)
- Set of $\boldsymbol{C}$ main meal scenarios ($\boldsymbol{C = 4}$)
- Set of $\boldsymbol{S_n}$ timing sub-scenarios ($\boldsymbol{S_n = 10}$)
- Simulation duration, d (d = 7 days)

Output:

7-day BG traces

```
for each subject v in V do
    for each meal sub-scenario s in S_n do
        for each timing scenario c in C do
            Initialize the UVa/Padova simulator for 7 days
            Select subject v
            Set meal sizes according to vector c
            Set bolus MBI_S calculated using equation 6.2
        end for
    end for
end for
Return 7-day BG traces
```

6.4 Graphical User Interface for Meal Insulin Bolus calculation

A Graphical User Interface (GUI)- based bolus calculator has been developed to easily calculate the meal-time insulin bolus using the proposed DCRNet for PH=60 minutes. To determine the optimal insulin bolus, select a patient and enter the targeted BG level. For a healthy individual, an ideal target BG level is 110 mg/dL [1], which is why this benchmark is set. Next, enter six recent BG values along with CHO and insulin (Current Acting Insulin) values. Current acting insulin (CAI) is the portion of previously administered insulin that remains effective in the body. In just moments, this intuitive GUI will provide a precise bolus insulin dose tailored to the selected adult patient, ensuring effective, personalized care. In this experiment, it is considered that the previously administered insulin is not functioning in the body. Therefore, CAI is set to zero. Figure 6.2 shows the GUI-based bolus calculator, which demonstrates how to calculate the meal-time bolus for adult 1 and 8.

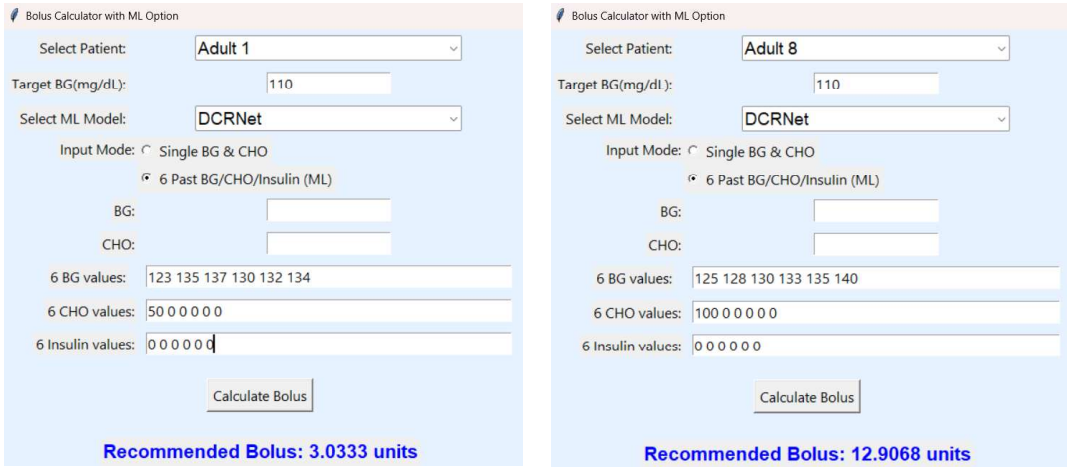

(a) **(b)**

Figure 6.2: Demonstration of GUI for calculating BG forecasting value for (a) Adult 1, and (b) Adult 8

6.5 Evaluation metrics of the proposed IIB therapy

Several glycaemic control metrics commonly used by the diabetes research community are applied to the proposed IIB therapy. The Following metrics are used to evaluate the proposed therapy:

6.5.1 Time in Range, Time Below Range and Time Above Range

Together with prediction accuracy measures (e.g., RMSE and MAE), clinical outcome measures are crucial for assessing the performance of an insulin therapy system. RMSE and MAE quantify numerical error in predicting BG but do not indicate whether BG remains within clinically safe limits. Thus, TIR, TAR and TBR [113] are used to evaluate glycaemic control and the safety of the proposed IIB therapy. These metrics provide a clinically meaningful assessment by measuring how much time BG stays within, above, or below the targeted range and are correlated with better diabetes control and lower risk of long-term complications.

- TIR, defined as $70 \leq BG \leq 180$ mg/dL (euglycemic range);
- TBR, defined as $BG < 70$ mg/dL, and
- TAR, defined as $BG > 180$ mg/dL

6.5.2 Low BG Index and High BG Index

Additionally, the risk of hypoglycaemia and hyperglycaemia are evaluated using the LBGI [114] and the HBGI [114], respectively. The following are the steps to compute LBGI and HBGI.

Step 1: Transform each Glucose (G) reading using following formula:

$$f(G) = 1.509 \times [\ln G^{1.084} - 5.381] \text{ if G is measured in mg/dL} \quad (6.6)$$

or

$$f(G) = 1.509 \times [\ln(18 \times G)^{1.084} - 5.381] \text{ if G is measured in mmol/L} \quad (6.7)$$

Step 2: Calculate the BG risk value using following formula:

$$r(G) = 10 \times [f(G)]^2 \quad (6.8)$$

Step 3: Separate into hypo- and hyperglycaemia components

Low risk component (LBGI):

$$rl(G) = \begin{cases} r(G), & if\ f(G) < 0 \\ 0, & otherwise \end{cases} \quad (6.9)$$

High risk component (HBGI):

$$rh(G) = \begin{cases} r(G), & if\ f(G) > 0 \\ 0, & otherwise \end{cases} \quad (6.10)$$

Step 4: Finally for *n* set of CGM readings $G_1, G_2, \ldots \ldots, G_n$, compute the LBGI as the average of *rl* (*G*) and the HBGI as the average of *rh* (*G*) from these readings:

$$LBGI = \frac{1}{n}\sum_{i=1}^{n} rl(G_i) \quad (6.11)$$

$$HBGI = \frac{1}{n}\sum_{i=1}^{n} rh(BG_i) \quad (6.12)$$

Step 5: After calculating LBGI and HBGI, categorize these values into three levels. Table 6.2 demonstrates the three risk levels for hypoglycaemia and hyperglycaemia event.

Table 6.2: Risk level for hypoglycaemia and hyperglycaemia event [113]

Risk level	Hypoglycaemia	Hyperglycaemia
Low	LBGI ≤ 2.5	HBGI ≤ 4.5
Moderate	2.5 < LBGI ≤ 5	4.5 < HBGI ≤ 9
High	LBGI > 5	HBGI> 9

6.5.3 BG Risk Index

BGRI [115], which combines the two contributions into a single risk score, is utilized to evaluate the overall quality of glycaemic control of suggested medication. For BGRI, follow the step 1 to 3 mention in 6.5.2. Further, calculates the BGRI as the daily average of the risk range.

$$BGRI = \frac{1}{M}\sum_{i=1}^{M} LBGI^i + HBGI^i \tag{6.13}$$

Where $LBGI_i = \max[rl(G_1{}^i), \ldots\ldots\ldots, rl(G_n{}^i)]$ and

$HBGI_i = \max\left[rh(G_1{}^i), \ldots\ldots\ldots, rh(G_n{}^i)\right]$ for day i; i = 1,2, …., M.

After that, the BGRI value classifies the BG control into three groups. Table 6.3 demonstrates the three risk levels for overall glycaemic control in terms of BGRI.

Table 6.3: Risk level for overall glycaemic control [115]

Risk level	overall glycaemic control
Low	BGRI < 20
Moderate	20 ≤ BGRI ≤ 40
High	BGRI > 40

6.5.4 Control-Variability grid analysis

A graphic representation of the lowest and maximum glucose levels in a real or virtual patient group is called a CVGA [116]. CVGA provides an immediate visual and quantitative insight into the overall quality of glycaemic control across the entire patient population, whether real or virtual. The CVGA determines whether the trend in control is safe and

desirable, and whether glucose levels are within the desired range. When assessing the effectiveness and safety of novel insulin dosing techniques, CVGA is a useful tool. CVGA is acquired as follows: Within the time period under consideration, a point with an X coordinate (minimum BG) and a Y coordinate (highest BG) is displayed for each participant (Figure 6.3). The most effective control is located in the lower-left corner of the X-axis, where it is inverted as it moves from 110 mg/dL (left) to 50 mg/dL (right). The general plot is a cloud of points representing multiple aspects of glycaemic control, scattered across the X-Y plane. To classify subjects, 9 rectangular areas are outlined in Figure 6.3.

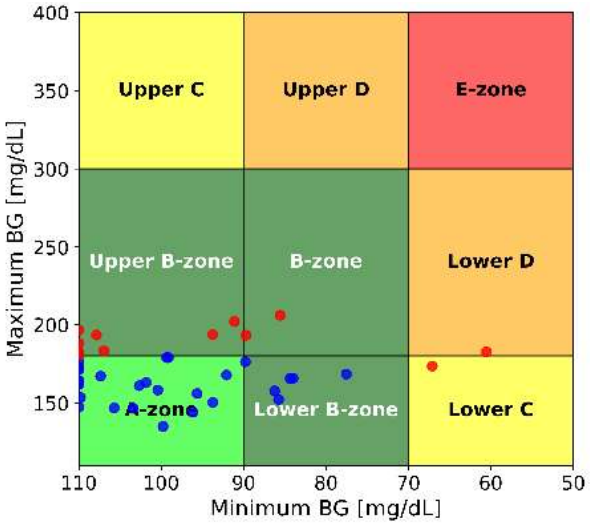

Figure 6.3: Visualization of control variability grid analysis

CVGA may be noise- and outlier-sensitive, as it depends on the maximum and minimum values of noisy samples. To mitigate this, it is advised to set the lower bound at 2.5% and the upper bound at 97.5% of the data distribution. This approach ensures that the Y–X coordinates correspond to a 95% confidence interval, reducing the impact of outliers.

Table 6.4 presents the Zone-wise details of CVGA, including the minimum and maximum BG ranges. Zone A, where the lowest BG is between 90 and 110 mg/dL and the highest BG is between 110 and 180 mg/dL, indicates accurate glucose control. Zone B represents clinically acceptable control with slight deviations, whereas the Lower B and Upper B zones show benign deviations toward hypoglycaemia and hyperglycaemia, respectively. Zone C indicate excessive therapeutic intervention when hyperglycaemia (Lower C) or hypoglycaemia (Upper C) are overcorrected. Zone D indicate inadequate therapeutic control due to either hyperglycaemia (Upper D) or hypoglycaemia (Lower D). Lastly, Zone E

represents impaired glucose regulation, where the greatest clinical risk is indicated by a minimum BG of less than 70 mg/dL and a maximum BG of more than 300 mg/dL. Therefore, improved glycaemic control and overall treatment performance are indicated by a higher percentage of observations in Zones A and B and few or no observations in Zones C, D, and E.

Table 6.4: Zone-wise details of CVGA, including the minimum and maximum BG ranges [116]

Zone	X (Min. BG mg/dL)	Y (Max. BG mg/dL)	Interpretation
A	90 – 110	110 – 180	Accurate control
Lower B	70 – 90	110 – 180	Benign deviation (toward hypoglycaemia)
B	70 – 90	180 – 300	Benign control deviation
Upper B	90 – 110	180 – 300	Benign deviation (toward hyperglycaemia)
Lower C	< 70	110 – 180	Overcorrection of hyperglycaemia
Upper C	90 – 110	> 300	Overcorrection of hypoglycaemia
Lower D	< 70	180 – 300	Failure to treat hypoglycaemia
Upper D	70 – 90	> 300	Failure to treat hyperglycaemia
E	< 70	> 300	Erroneous control

6.6 Performance analysis of IIB therapy using TIR, TBR and TAR

The optimal sub-scenario for adults is determined by conducting additional analysis of S_a-S_j to examine the 40 insulin scenarios and their effects on 10 adults. The percentage values for TIR, TBR, and TAR are provided for all 10 adults, organized by sub-scenario (S_a-S_j). Next, the average TIR, TBR, and TAR for each sub-scenario are calculated across all 10 subjects, and these results are analysed using the mean, median, and IQR for each sub-scenario, as illustrated in Table 6.5.

The mean provides an evaluation of the metric's centre tendency. It denotes the average performance of all 10 adults and indicates the expected outcome if the sub-scenarios are applied to a larger population. A high mean TIR indicates that the sub-scenario is effective for the group as a whole. The median provides a more robust metric, less affected by outliers, and reflects the typical adult response under a specific insulin sub-scenario. If the median significantly differs from the mean, only a few outlier patients are distorting your

results. The IQR shows the middle 50% of the data. A low IQR indicates that the insulin scenario yields consistent outcomes for all ten persons.

Table 6.5: Performance evaluation using TIR, TBR and TAR for Proposed IIB Therapy

S_n	TIR (%)			TBR (%)			TAR (%)		
	Mean	Median	IQR	Mean	Median	IQR	Mean	Median	IQR
S_a	93.04	93.46	5.32	3.80	0.70	7.53	3.15	2.39	4.36
S_b	97.24	97.74	4.16	1.92	0.00	3.84	0.84	0.27	1.67
S_c	97.72	98.16	4.09	0.67	0.00	0.00	1.61	0.51	3.38
S_d	98.66	99.25	0.94	0.95	0.05	0.60	0.39	0.00	0.38
S_e	98.41	99.21	2.33	0.79	0.05	0.59	0.80	0.00	1.58
S_f	98.86	99.21	1.93	0.20	0.00	0.03	0.94	0.00	1.79
S_g	98.50	99.97	2.01	0.01	0.00	0.00	1.49	0.00	2.01
S_h	97.87	98.58	2.25	0.01	0.00	0.00	2.12	1.39	2.26
S_i	97.60	98.31	3.05	0.17	0.00	0.00	2.23	0.99	3.00
S_j	97.76	98.46	2.83	0.20	0.00	0.00	2.04	0.83	2.69

These findings suggest that S_a is associated with less-than-ideal glycaemic control, characterized by prolonged periods outside the target range. Conversely, S_d-S_g consistently outperforms others. S_g and S_h have decreased hypoglycaemia with the lowest TBR (mean = 0.01%, median = 0%, and IQR = 0%), whereas S_f has the highest TIR (mean = 98.86%, median = 99.21%, and IQR = 1.93%). With the lowest TAR (mean = 0.39%, median = 0%, and IQR = 0.38%), S_d has controlled hyperglycaemia. These results imply that the proposed intermittent therapy can reduce glycaemic fluctuations while maintaining appropriate glucose levels, and optimal sub-scenarios are S_f and S_g.

6.7 Performance analysis of IIB therapy using LBGI, HBGI and BGRI

The analysis of LBGI, HBGI, and BGRI across 10 sub-scenarios (S_a-S_j) for 10 adults is presented in Table 6.6. A higher LBGI indicates a raised risk of hypoglycaemia, while a higher HBGI indicates a greater risk of hyperglycaemia. Additionally, a higher BGRI indicates a higher risk of glycaemic control issues.

As shown in Table 6.6, LBGI has the highest Mean and Median for S_a (Mean = 1.76, Median = 1.08), which suggests a greater risk of hypoglycaemia. In contrast, the values for S_h (Mean = 0.24, Median = 0.16) and S_g (Mean = 0.23, Median = 0.14) are the lowest for LBGI, implying a better defence against hypoglycaemia. Furthermore, S_a-S_d and S_f demonstrate

significant variability, as indicated by their interquartile ranges (IQRs), while S_e and S_g-S_j show less variability, suggesting more consistent responses in these scenarios.

Overall, LBGI remains below 2.5 across all sub-scenarios, indicating a relatively moderate burden of hypoglycaemia. HBGI results are slightly higher than the LBGI in the S_a-S_j subgroup. Specifically, S_a has the highest mean HBGI of 2.25 (Median = 2.15), suggesting a tendency toward hyperglycaemia. In contrast, S_d is associated with better glucose control and has the lowest risk of hyperglycaemia, with a mean HBGI of 1.08 (Median = 1.07). The S_g has a mean HBGI of 1.57 (Median = 1.3), and S_h has a mean of 1.58 (Median = 1.4), both indicating a lower risk of hyperglycaemia than S_d. Overall, values across all sub-scenarios remain below 4.5, indicating a relatively low burden of hyperglycaemia, although the trend for HBGI is less pronounced.

Table 6.6: Statistical analysis of IIB therapy using LBGI, HBGI and BGRI

S_n	LBGI			HBGI			BGRI		
	Mean	**Median**	**IQR**	**Mean**	**Median**	**IQR**	**Mean**	**Median**	**IQR**
S_a	1.76	1.08	2.02	2.25	2.15	1.16	14.6	13.92	5.7
S_b	1	0.53	1.69	1.28	1.24	0.82	9.28	9.18	4.51
S_c	0.75	0.51	0.85	1.6	1.6	1.1	9.21	9.11	3.31
S_d	0.8	0.45	1.1	1.08	1.07	0.7	9.67	9.35	4.94
S_e	0.72	0.56	0.7	1.4	1.11	0.76	10.54	9.71	3.18
S_f	0.46	0.28	0.79	1.27	1.2	0.69	7.49	7.26	2.89
S_g	0.23	0.14	0.45	1.57	1.3	0.9	7.48	6.36	3.35
S_h	0.24	0.16	0.46	1.58	1.4	0.73	9.22	8.52	3.61
S_i	0.35	0.29	0.61	1.6	1.61	0.62	9.52	8.89	4.84
S_j	0.4	0.34	0.71	1.64	1.69	0.57	9.68	8.84	5.01

The analysis of BGRI across the S_a-S_j reveals significant variations in both central tendency and dispersion. S_a displayed the highest BGRI values among all the groups, with a mean of 14.6 and a median of 13.92, accompanied by a substantial IQR of 5.7. In contrast, S_f and S_g report relatively low median values of 7.26 and 6.36, respectively, and their mean values are also the lowest at, 7.49 and 7.48. These findings suggest that the *Sf* and *Sg* exhibit more consistent, overall lower BGRI scores. Additionally, *Sf* and *Sg*, which balance both hypoglycaemia and hyperglycaemia, ultimately present the lowest overall glycaemic risk.

6.8 Performance analysis using CVGA

The CVGA is used to evaluate the overall accuracy and safety of glucose predictions for all combined sub-scenarios (S_a–S_j). Subject-level minimum and maximum glucose estimates (2.5th and 97.5th percentiles) for each S_a through S_j over the four main scenarios (c_1–c_4) are combined to construct CVGA graphs (one plot per sub-scenario). The CVGA plots display the relationship between each subject's minimum and maximum daily glucose levels using five clinical zones (A–E). Zone A represents clinically accurate glucose readings with minimal deviation from ideal management. Normal variations with no clinical importance are represented by zone B. Zones C–E show rising rates of clinical mistakes and potential harm.

Figure 6.4 presents the CVGA analysis of sub-scenarios (S_a–S_j) across ten adult cohorts. Adult BG levels are indicated as blue dots for values ranging between 70 and 180 mg/dL, while levels outside this range are depicted as red dots. Additionally, Table 6.5 displays the proportion of adults' BG traces categorized in zones A and B. Figure 6.4 illustrates that the majority of data points across all insulin scenarios for all 10 adult subjects' BG lie within Zones A and B, indicating extremely safe and dependable glucose regulation. Table 6.7 shows that across various insulin and meal scenarios, the overall accuracy of IIB therapy is remarkable, with 85% to 100% of BG values lying in Zone (A+B).

In particular, sub-scenarios S_f, S_g, and S_h produced all the data in Zone (A + B), exhibiting optimal glycaemic management and low variance. S_f has the highest percentage of precisely accurate glucose predictions, with 75% of BG values in Zone A and 100% lying in Zone (A+B), suggesting a better balance between insulin delivery and CHO intake. The modified insulin dosage in S_f reduces deviations from target ranges and encourages a steadier glucose profile. However, S_g also provides better glycaemic control, as 70% of BG values lie in Zone A and 100% lie in Zone (A+B).

The analysis shows that a more stable glucose profile and fewer deviations from the intended ranges are encouraged by the modified insulin timing in S_f and S_g. However, sub-scenario S_a shows somewhat higher variability, with 32.5% of BG values lying in Zone A and 85% in Zone (A+B), likely due to insulin overlap effects or variations in meal timing. Overall, the results indicate that the proposed IIB therapy provides better and safer glycaemic control, with sub-scenarios S_f and S_g outperforming the other scenarios.

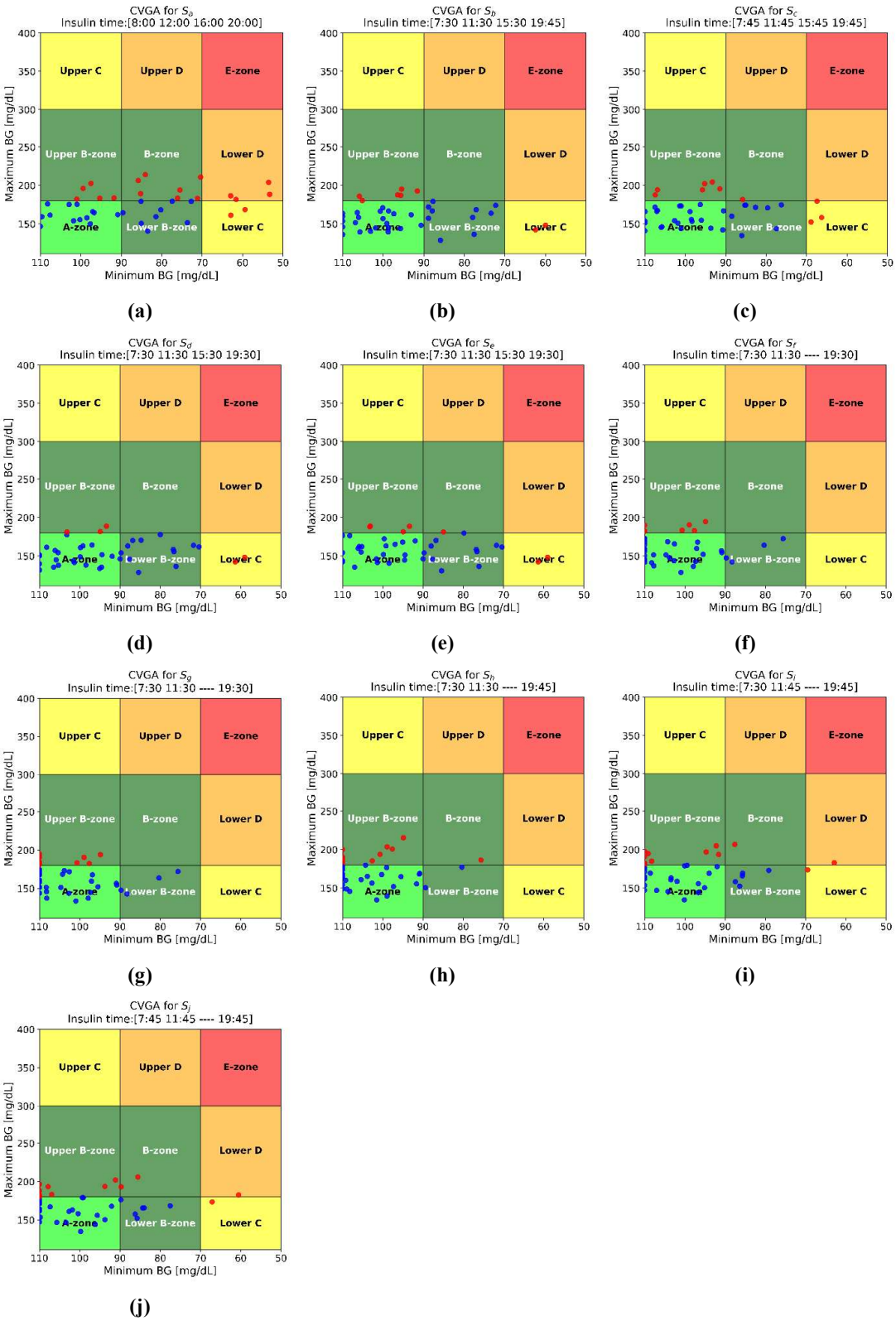

Figure 6.4: Performance analysis using CVGA for sub-scenarios (S_a–S_j) across a 10-adult cohort

Table 6.7: The percentage value of adults lies in zone A and Zone B in CVGA

S_I	Zone A (%)	Zone B (%)	Zone (A + B) (%)
S_a	32.5	52.5	85
S_b	55	40	95
S_c	55	37.5	92.5
S_d	60	35	95
S_e	57.5	37.5	95
S_f	75	25	100
S_g	70	30	100
S_h	65	35	100
S_i	55	40	95
S_j	52.5	42.5	95

6.9 Summary

The results demonstrate that the proposed IIB therapy effectively controls BG levels by administering three insulin doses daily: one at breakfast, one at lunch, and one at dinner, skipping the snack-time insulin (S_f). One extra meal can also be planned for the night, after dinner around 22:00, to avoid hypoglycaemia events at midnight (S_g). This therapy reduces the risk of hypoglycaemia and hyperglycaemia while increasing the duration spent within the target glucose range (70–180 mg/dL). In CVGA analysis, scenarios S_f and S_g achieve 100% clinical precision, near-ideal glucose management, and minimal glycaemic fluctuation. These results indicate that using BG forecasting to calculate insulin bolus doses can greatly enhance glucose control and lower the risk of hypoglycaemia in T1D.

For individuals with T1D, the proposed therapy based on MDI is a straightforward and user-friendly substitute for automated insulin delivery systems, such as artificial pancreases. It does not require body-mounted devices or insulin pumping. Altogether, the findings suggest that this solution can be a significant, patient-centred, data-driven change in personalized insulin delivery; however, further confirmation in real-world settings and larger population-based studies is also essential. The accuracy of IIB therapy relies on the performance of DCRNet for PH=60. The forecasting model with shorter PHs can also be utilised in the proposed therapy to increase prediction accuracy, but this reduces the insulin intervention time. In future work, the evaluation of IIB therapy across different PHs will be conducted.

Chapter 7
Proposed Continuous Blood Glucose Monitoring System

7.1 Introduction

The treatment of T1D requires a systematic model that integrates predictive analytics with real-time data collection. To shift towards proactive rather than reactive glucose management, the chapter introduces a multi-component Continuous Blood Glucose Monitoring system. The architecture incorporates four basic functional blocks: CGM Data Generation, BG Measurement, BG Forecasting, and Intermittent Insulin Bolus (IIB) Therapy. The system can provide a complete framework for controlling BG levels by using sensor data and exogenous variables. It provides an ML-based forecasting engine at the heart of this system that predicts BG levels 60 minutes ahead, enabling optimal timing and dosing of insulin boluses.

7.2 Continuous Blood Glucose Monitoring System

The proposed Continuous Blood Glucose Monitoring system comprises four components. They are CGM data generation, BG measurement, BG forecasting, and IIB therapy. The proposed CGM system is illustrated in Figure 7.1. CGM data collection involves attaching a non-invasive CGM sensor to the subject, which continuously measures BG at regular intervals (5 minutes). Sensor data, along with other personalized data (age, gender, height, Dia. BP, Sys. BP, heart rate, weight, diabetes history, duration of diabetes, sleep duration, sleep quality, daily walking steps), are pre-processed and fed into an ML model as input features to estimate the current BG level (G_t) precisely.

The most recent n BG samples ($n = 6$) and CHO are used to forecast BG levels. The goal of the BG forecasting architecture is to forecast BG levels one hour in advance, which can assist in planning future glucose management strategies. IIB therapy uses the BG level forecast for 1 hour later (BG_{t+60}), as it is crucial for calculating bolus insulin (BI_S). This calculation helps determine how much insulin to take before each meal, rather than relying

solely on current BG readings (G_t). After calculating the optimal bolus, the next step is to decide the timing of insulin administration for each meal. This approach effectively regulates postprandial BG levels and ensures optimal glycaemic control throughout the day. Overall, this system enhances diabetes management and improves overall glycaemic control, helping individuals confidently manage their BG levels.

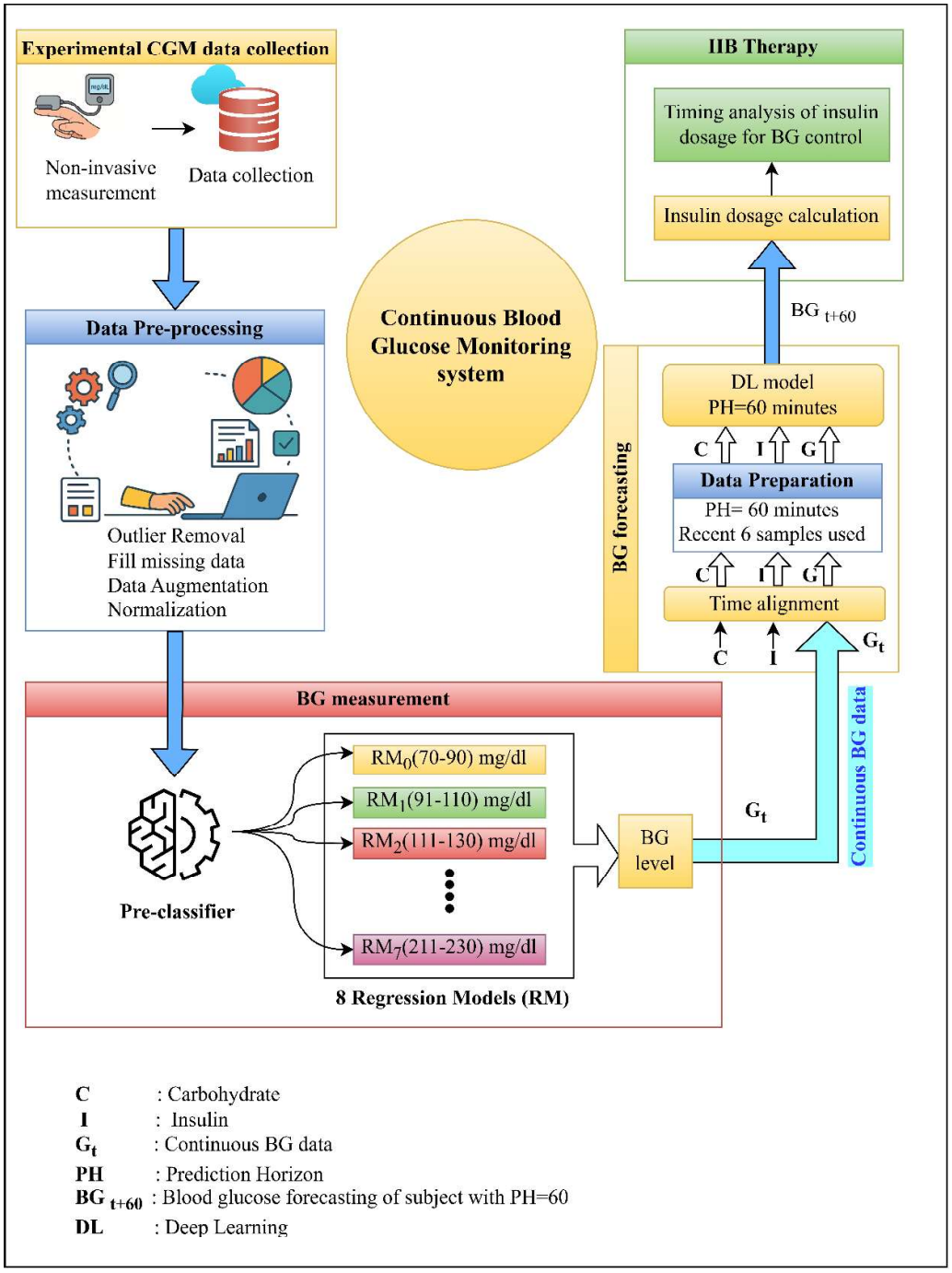

Figure 7.1: Proposed Continuous Blood Glucose Monitoring system

A 60-minute PH was chosen for this study because it provides sufficient lead time for proactive insulin dosage calculation while maintaining a respectable level of predictive accuracy. For this PH alone, the proposed IIB therapy is created and assessed. This study did not examine the effects of longer PHs (e.g., 90 or 120 minutes) on forecasting accuracy and therapy effectiveness, but this remains a crucial area for future research, as longer horizons are typically associated with greater prediction uncertainty, even though they may allow for earlier intervention.

By combining an IIB therapeutic framework with a DCRNet-based BG forecasting model, the proposed approach is different from commercially available CGM systems. The proposed approach forecasts BG levels for 60 minutes and uses these predictions to suggest proactive insulin dosing, whereas traditional CGM systems primarily provide real-time glucose measurements. However, the proposed system is evaluated only in a simulated environment; clinical validation is necessary before actual implementation.

7.3 Advantages of the Proposed Continuous Blood Glucose Monitoring System

This Continuous Blood Glucose Monitoring system is an integrated system with various technological and therapeutic benefits compared to conventional monitoring methods. These benefits include:

- Non-Invasive Integration: The system utilizes non-invasive sensors, reducing physical strain on the patient while maintaining a high sampling frequency of every 5 minutes.
- Multivariate Input: Unlike univariate models, this system uses multiple input features (sensors and personalized data) for BG estimation and forecasting, yielding more accurate, personalized predictions.
- Proactive Glycaemic Control: Instead of merely reacting to current BG fluctuations (G_t), the system forecasts BG levels one hour in advance (BG_{t+60}), allowing for preventive changes.
- Optimized Postprandial Regulation: The technology significantly reduces post-meal glucose spikes by accurately timing insulin delivery and estimating the ideal dosage.

7.4 Summary

In summary, the proposed system bridges the gap between insulin intake and glucose monitoring by introducing a predictive feedback loop. The architecture enables the IIB therapy component to calculate mealtime bolus insulin more accurately using 60-minute forecasted BG values. These ML predictions, coupled with clinical therapeutic logic, will minimize the risk of long-term diabetic complications and improve the user's quality of life by maintaining glucose levels within the target range.

Chapter 8
Conclusions and Scope of Future Work

8.1 Conclusions

This research effectively addresses the limitations of invasive Continuous Blood Glucose Monitoring systems and current static insulin dosage techniques. It establishes a strong foundation for accurately measuring real-time BG by integrating an innovative, non-invasive single-sensor device with an advanced ML-based Distributed Architecture. BG forecasting is effectively performed using DCRNet in the proposed system.

The core contribution of this research is the development of the IIB therapy, which utilizes forecasted glucose data to optimize insulin delivery. This predictive approach demonstrated exceptional clinical efficacy, achieving 99% of BG levels within the euglycemic range and ensuring patient safety, as all BG levels fell within zones A and B in the CVGA analysis.

Ultimately, this thesis proposes an effective, comprehensive, non-invasive CGM system for T1D that emphasizes glycaemic stability and reduces the need for a continuously attached insulin pump by recommending only three bolus insulin doses (excluding snacks) each day, each taken at least 30 minutes before each meal. This thesis also offers a cost-effective, patient-friendly alternative to traditional AP systems, significantly improving the quality of life for individuals with T1D.

8.2 Scope of Future Work

To transfer the proposed CGM system, DCRNet forecasting model, and IIB therapy to a real-world setting, future research will focus on testing them in a larger, more diverse clinical sample. Future research will also determine the system's capacity to record live behavioural variables related to exercise, stress, and unplanned CHO intake. Currently, the proposed framework relies on accurate sensor readings. To increase the system's robustness and dependability in real-time applications, further research will focus on integrating sensor fault detection, and signal quality assessment.

More importantly, to ensure patient safety against forecasting errors, future research will involve real-time uncertainty estimation and the development of robust physiological safety

barriers for insulin delivery. Lastly, the implementation studies will involve real-time investigations of model compression mechanisms, including pruning and quantization, to reduce the computational latency of wearable edge devices.

The ethical and legal prerequisites for the clinical implementation of the proposed AI-based CGM system will be the main focus of future research for actual implementation. These include conducting extensive clinical validation, ensuring patient data privacy and security, enhancing the transparency and reliability of AI-based recommendations, and obtaining the required regulatory clearances prior to practical implementation.

References

[1] "IDF Diabetes atlas 11th Edition," 2025.

[2] S. Vashist, "Continuous Glucose Monitoring Systems: A Review," *Diagnostics*, vol. 3, no. 4, pp. 385–412, 2013, doi: 10.3390/diagnostics3040385.

[3] A. Facchinetti, "Continuous glucose monitoring sensors: Past, present and future algorithmic challenges," *Sensors (Switzerland)*, vol. 16, no. 12, pp. 1–12, 2016, doi: 10.3390/s16122093.

[4] G. Cappon, G. Acciaroli, M. Vettoretti, A. Facchinetti, and G. Sparacino, "Wearable continuous glucose monitoring sensors: A revolution in diabetes treatment," *Electronics (Switzerland)*, vol. 6, no. 3, Sep. 2017, doi: 10.3390/electronics6030065.

[5] A. K. Singh and S. K. Jha, "Fabrication and validation of a handheld noninvasive, optical biosensor for self-monitoring of glucose using saliva," *IEEE Sens. J.*, vol. 19, no. 18, pp. 8332–8339, 2019.

[6] S. Malik, R. Khadgawat, S. Anand, and S. Gupta, "Non-invasive detection of fasting blood glucose level via electrochemical measurement of saliva," *Springerplus*, vol. 5, no. 1, Dec. 2016, doi: 10.1186/s40064-016-2339-6.

[7] M. S. Prasad *et al.*, "Polypyrrole Supported with Copper Nanoparticles Modified Alkali Anodized Steel Electrode for Probing of Glucose in Real Samples," *IEEE Sens. J.*, vol. 18, no. 13, pp. 5203–5212, Jul. 2018, doi: 10.1109/JSEN.2018.2829982.

[8] T. Dai and A. Adler, "In vivo blood characterization from bioimpedance spectroscopy of blood pooling," *IEEE Trans. Instrum. Meas.*, vol. 58, no. 11, pp. 3831–3838, 2009, doi: 10.1109/TIM.2009.2020836.

[9] K. Song, U. Ha, S. Park, J. Bae, and H. J. Yoo, "An Impedance and Multi-Wavelength Near-Infrared Spectroscopy IC for Non-Invasive Blood Glucose Estimation," *IEEE J. Solid-State Circuits*, vol. 50, no. 4, pp. 1025–1037, Apr. 2015, doi: 10.1109/JSSC.2014.2384037.

[10] O. Cherkasova, M. Nazarov, and A. Shkurinov, "Noninvasive blood glucose monitoring in the terahertz frequency range," *Opt. Quantum Electron.*, vol. 48, no. 3, Mar. 2016, doi: 10.1007/s11082-016-0490-5.

[11] Y. Sun *et al.*, "Random Forest Analysis of Combined Millimeter-Wave and Near-Infrared Sensing for Noninvasive Glucose Detection," *IEEE Sens. J.*, vol. 23, no. 17, pp. 20294–20309, Sep. 2023, doi: 10.1109/JSEN.2023.3293248.

[12] A. M. Joshi, P. Jain, S. P. Mohanty, and N. Agrawal, "IGLU 2.0: A New Wearable for Accurate Non-Invasive Continuous Serum Glucose Measurement in IoMT Framework," *IEEE Transactions on Consumer Electronics*, vol. 66, no. 4, pp. 327–335, 2020, doi: 10.1109/TCE.2020.3011966.

[13] A. M. Joshi, P. Jain, and S. P. Mohanty, "IGLU 3.0: A Secure Noninvasive Glucometer and Automatic Insulin Delivery System in IoMT," *IEEE Transactions on Consumer Electronics*, vol. 68, no. 1, pp. 14–22, Feb. 2022, doi: 10.1109/TCE.2022.3145055.

[14] Yiting Wei, Jiaxin Liu, Lingyue Hu, Bingo Wing-Kuen Ling, and Qing Liu, "Time frequency analysis-based averaging and fusion of features for wearable non-invasive blood glucose estimation," *IEEE Transactions on Consumer Electronics*, vol. 69, no. 3, pp. 510–521, 2023, doi: 10.1109/TCE.2023.3278540.

[15] W.-C. Shih, K. L. Bechtel, and M. V. Rebec, "Noninvasive glucose sensing by transcutaneous Raman spectroscopy," *J. Biomed. Opt.*, vol. 20, no. 5, p. 051036, Feb. 2015, doi: 10.1117/1.jbo.20.5.051036.

[16] H. Ali, F. Bensaali, and F. Jaber, "Novel Approach to Non-Invasive Blood Glucose Monitoring Based on Transmittance and Refraction of Visible Laser Light," *IEEE Access*, vol. 5, pp. 9163–9174, 2017, doi: 10.1109/ACCESS.2017.2707384.

[17] S. Haxha and J. Jhoja, "Optical Based Noninvasive Glucose Monitoring Sensor Prototype," *IEEE Photonics J.*, vol. 8, no. 6, Dec. 2016, doi: 10.1109/JPHOT.2016.2616491.

[18] P. Jain, R. Maddila, and A. M. Joshi, "A precise non-invasive blood glucose measurement system using NIR spectroscopy and Huber's regression model," *Opt. Quantum Electron.*, vol. 51, no. 2, Feb. 2019, doi: 10.1007/s11082-019-1766-3.

[19] P. Jain, A. M. Joshi, and S. P. Mohanty, "iGLU: An Intelligent Device for Accurate Noninvasive Blood Glucose-Level Monitoring in Smart Healthcare," *IEEE Consumer Electronics Magazine*, vol. 9, no. 1, pp. 35–42, 2020, doi: 10.1109/MCE.2019.2940855.

[20] P. Jain, A. M. Joshi, and S. P. Mohanty, "iGLU 4.0: Intelligent Non-invasive Glucose Measurement and Its Control with Physiological Parameters," *SN Comput. Sci.*, vol. 5, no. 4, Apr. 2024, doi: 10.1007/s42979-024-02727-2.

[21] P. P. Pai, A. De, and S. Banerjee, "Accuracy enhancement for noninvasive glucose estimation using dual-wavelength photoacoustic measurements and kernel-based calibration," *IEEE Trans. Instrum. Meas.*, vol. 67, no. 1, pp. 126–135, Jan. 2018, doi: 10.1109/TIM.2017.2761237.

[22] C. W. Pirnstill, B. H. Malik, V. C. Gresham, and G. L. Coté, "In Vivo Glucose Monitoring Using Dual-Wavelength Polarimetry to Overcome Corneal Birefringence in the Presence of Motion," *Diabetes Technol. Ther.*, vol. 14, no. 9, pp. 819–827, Sep. 2012, doi: 10.1089/dia.2012.0070.

[23] S. Habbu, M. Dale, and R. Ghongade, "Estimation of blood glucose by non-invasive method using photoplethysmography," *Sādhanā*, vol. 44, no. 6, p. 135, Jun. 2019, doi: 10.1007/s12046-019-1118-9.

[24] E. Monte-Moreno, "Non-invasive estimate of blood glucose and blood pressure from a photoplethysmograph by means of machine learning techniques," *Artif. Intell. Med.*, vol. 53, no. 2, pp. 127–138, Oct. 2011, doi: 10.1016/j.artmed.2011.05.001.

[25] P. Mohammadi, A. Mohammadi, and A. Kara, "Dual-Frequency Microwave Resonator for Noninvasive Detection of Aqueous Glucose," *IEEE Sens. J.*, vol. 23, no. 18, pp. 21246–21253, Sep. 2023, doi: 10.1109/JSEN.2023.3303170.

[26] S. J. J. Kirubakaran, M. A. Bennet, and N. R. Shanker, "Antiallergic Abdominal Belt for Human Glucose Level Measurement Using Microwave Active Sensor Antenna," *IEEE Sens. J.*, vol. 23, no. 14, pp. 16227–16237, Jul. 2023, doi: 10.1109/JSEN.2023.3280031.

[27] M. Althobaiti and I. Al-Naib, "Optimization of Dual-Channel Near-Infrared Non-Invasive Glucose Level Measurement Sensors Based on Monte-Carlo Simulations," *IEEE Photonics J.*, vol. 13, no. 3, Jun. 2021, doi: 10.1109/JPHOT.2021.3079408.

[28] S. Dutt, S. Chandranouli, and A. kumar Das, *Machine Learning*. Pearson, 2019.

[29] E. I. Georga *et al.*, "Multivariate prediction of subcutaneous glucose concentration in type 1 diabetes patients based on support vector regression," *IEEE J. Biomed. Health Inform.*, vol. 17, no. 1, pp. 71–81, 2013, doi: 10.1109/TITB.2012.2219876.

[30] J. H. Cho and P. U. Kurup, "Decision tree approach for classification and dimensionality reduction of electronic nose data," *Sens. Actuators B Chem.*, vol. 160, no. 1, pp. 542–548, Dec. 2011, doi: 10.1016/j.snb.2011.08.027.

[31] E. I. Georga, V. C. Protopappas, D. Polyzos, and D. I. Fotiadis, *A Predictive Model of Subcutaneous Glucose Concentration in Type 1 Diabetes Based on Random Forests*. 2012. doi: 10.0/Linux-x86_64.

[32] Q. Wang, W. Cao, J. Guo, J. Ren, Y. Cheng, and D. N. Davis, "DMP_MI: An effective diabetes mellitus classification algorithm on imbalanced data with missing values," *IEEE Access*, vol. 7, pp. 102232–102238, 2019, doi: 10.1109/ACCESS.2019.2929866.

[33] M. Zhang, K. B. Flores, and H. T. Tran, "Deep learning and regression approaches to forecasting blood glucose levels for type 1 diabetes," *Biomed. Signal Process. Control*, vol. 69, Aug. 2021, doi: 10.1016/j.bspc.2021.102923.

[34] A. J. Smola and B. Scholkopf, "A tutorial on support vector regression," *Stat. Comput.*, vol. 14, no. 3, pp. 199–222, Aug. 2004.

[35] A. Ghosh, A. Sufian, F. Sultana, A. Chakrabarti, and D. De, "Fundamental concepts of convolutional neural network," in *Recent Trends and Advances in Artificial Intelligence and Internet of Things. Intelligent Systems Reference Library*, vol. 172, Springer, Cham, 2020, pp. 519–567. doi: 10.1007/978-3-030-32644-9_36.

[36] A. Zaitcev, M. R. Eissa, Z. Hui, T. Good, J. Elliott, and M. Benaissa, "A Deep Neural Network Application for Improved Prediction of HbA 1c in Type 1 Diabetes," *IEEE J. Biomed. Health Inform.*, vol. 24, no. 10, pp. 2932–2941, 2020, doi: 10.1109/JBHI.2020.2967546.

[37] S. M. Lundberg and S. I. Lee, "A unified approach to interpreting model predictions," *Adv. Neural Inf. Process. Syst.*, vol. 30, pp. 1–10, 2017.

[38] M. Du, N. Liu, and X. Hu, "Techniques for Interpretable Machine Learning".

[39] D. Dave, H. Naik, S. Singhal, and P. Patel, "Explainable AI meets Healthcare: A Study on Heart Disease Dataset," pp. 1–23, 2020, [Online]. Available: http://arxiv.org/abs/2011.03195

[40] J. Peng *et al.*, "An Explainable Artificial Intelligence Framework for the Deterioration Risk Prediction of Hepatitis Patients," *J. Med. Syst.*, vol. 45, no. 5, 2021, doi: 10.1007/s10916-021-01736-5.

[41] Y. Du, A. R. Rafferty, F. M. McAuliffe, L. Wei, and C. Mooney, "An explainable machine learning-based clinical decision support system for prediction of gestational diabetes mellitus," *Sci. Rep.*, vol. 12, no. 1, pp. 1–14, 2022, doi: 10.1038/s41598-022-05112-2.

[42] M. T. Ribeiro, S. Singh, and C. Guestrin, "'Why Should I Trust You?' Explaining the Predictions of Any Classifier," *NAACL-HLT 2016 - 2016 Conference of the North American Chapter of the Association for Computational Linguistics: Human Language Technologies, Proceedings of the Demonstrations Session*, pp. 97–101, 2016, doi: 10.18653/v1/n16-3020.

[43] C. Toffanin, L. Magni, and C. Cobelli, "Artificial Pancreas: In Silico Study Shows No Need of Meal Announcement and Improved Time in Range of Glucose with Intraperitoneal vs. Subcutaneous Insulin Delivery," *IEEE Trans. Med. Robot. Bionics*, vol. 3, no. 2, pp. 306–314, May 2021, doi: 10.1109/TMRB.2021.3075775.

[44] M. N. Pelkey, M. E. Boyle, A. Long, J. C. Castro, C. B. Cook, and B. Thompson, "Hybrid Closed-Loop Insulin Pump Technology Can Be Safely Used in the Inpatient Setting," *Endocrine Practice*, vol. 29, no. 1, pp. 24–28, Jan. 2023, doi: 10.1016/j.eprac.2022.11.006.

[45] M. Nwokolo and R. Hovorka, "The Artificial Pancreas and Type 1 Diabetes," *J. Clin. Endocrinol. Metab.*, vol. 108, no. 7, pp. 1614–1623, Jun. 2023, doi: 10.1210/clinem/dgad068.

[46] D. Pollakova, A. Lauria Pantano, U. Di Folco, M. R. Nardone, and C. Tubili, "Advanced hybrid closed loop (artificial pancreas) and carbohydrate count in type 1 diabetes," *Med. J. Nutrition Metab.*, vol. 17, no. 3, pp. 219–227, Sep. 2024, doi: 10.3233/MNM-230125.

[47] B. M. Ahmed, M. E. Ali, M. M. Masud, M. R. Azad, and M. Naznin, "After-meal blood glucose level prediction for type-2 diabetic patients," *Heliyon*, vol. 10, no. 7, Apr. 2024, doi: 10.1016/j.heliyon.2024.e28855.

[48] C. Ji, T. Jiang, L. Liu, J. Zhang, and L. You, "Continuous glucose monitoring combined with artificial intelligence: redefining the pathway for prediabetes management," *Front. Endocrinol. (Lausanne).*, vol. 16, 2025, doi: 10.3389/fendo.2025.1571362.

[49] S. J. Kim, J. S. Moon, and S. Y. Jung, "Long-term blood glucose prediction using deep learning-based noise reduction," *ICT Express*, Aug. 2025, doi: 10.1016/j.icte.2025.05.009.

[50] U. Krishnamoorthy, V. Karthika, M. K. Mathumitha, H. Panchal, V. K. S. Jatti, and A. Kumar, "Learned prediction of cholesterol and glucose using ARIMA and LSTM models – A comparison," *Results in Control and Optimization*, vol. 14, Mar. 2024, doi: 10.1016/j.rico.2023.100362.

[51] G. Alfian *et al.*, "Blood glucose prediction model for type 1 diabetes based on artificial neural network with time-domain features," *Biocybern. Biomed. Eng.*, vol. 40, no. 4, pp. 1586–1599, Oct. 2020, doi: 10.1016/j.bbe.2020.10.004.

[52] J. Martinsson, A. Schliep, B. Eliasson, and O. Mogren, "Blood Glucose Prediction with Variance Estimation Using Recurrent Neural Networks," *J. Healthc. Inform. Res.*, vol. 4, no. 1, pp. 1–18, Mar. 2020, doi: 10.1007/s41666-019-00059-y.

[53] Li Kezhi and Liu C., T. Zhu, P. Herrero, and P. Georgiou, "GluNet: A Deep Learning Framework for Accurate Glucose Forecasting," *IEEE J. Biomed. Health Inform.*, vol. 24, no. 2, pp. 414–423, Feb. 2020, doi: 10.1109/JBHI.2019.2931842.

[54] H. V. Dudukcu, M. Taskiran, and T. Yildirim, "Blood glucose prediction with deep neural networks using weighted decision level fusion," *Biocybern. Biomed. Eng.*, vol. 41, no. 3, pp. 1208–1223, Jul. 2021, doi: 10.1016/j.bbe.2021.08.007.

[55] H. V. Dudukcu, M. Taskiran, and T. Yildirim, "Consolidated or individual training: Which one is better for blood glucose prediction?," in *2021 International Conference on INnovations in Intelligent SysTems and Applications (INISTA)*, IEEE, Aug. 2021, pp. 1–6. doi: 10.1109/INISTA52262.2021.9548612.

[56] X. Xiong, X. L. Yang, Y. Cai, Y. Xue, J. F. He, and H. Su, "Exploring the potential of deep learning models integrating transformer and LSTM in predicting blood glucose levels for T1D patients," *Digit. Health*, vol. 11, Jan. 2025, doi: 10.1177/20552076251328980.

[57] M. F. Rabby, Y. Tu, M. I. Hossen, I. Lee, A. S. Maida, and X. Hei, "Stacked LSTM based deep recurrent neural network with kalman smoothing for blood glucose prediction," *BMC Med. Inform. Decis. Mak.*, vol. 21, no. 1, Dec. 2021, doi: 10.1186/s12911-021-01462-5.

[58] H. Butt, I. Khosa, and M. A. Iftikhar, "Feature Transformation for Efficient Blood Glucose Prediction in Type 1 Diabetes Mellitus Patients," *Diagnostics*, vol. 13, no. 3, p. 340, Jan. 2023, doi: 10.3390/diagnostics13030340.

[59] M. He, W. Gu, Y. Kong, L. Zhang, C. J. Spanos, and K. M. Mosalam, "CausalBG: Causal Recurrent Neural Network for the Blood Glucose Inference with IoT Platform," *IEEE Internet Things J.*, vol. 7, no. 1, pp. 598–610, 2020, doi: 10.1109/JIOT.2019.2946693.

[60] R. Giancotti *et al.*, "Forecasting glucose values for patients with type 1 diabetes using heart rate data," *Comput. Methods Programs Biomed.*, vol. 257, Dec. 2024, doi: 10.1016/j.cmpb.2024.108438.

[61] X. Huang *et al.*, "Comparison of feature learning methods for non-invasive interstitial glucose prediction using wearable sensors in healthy cohorts: a pilot study," *Intelligent Medicine*, vol. 4, no. 4, pp. 226–238, Nov. 2024, doi: 10.1016/j.imed.2024.05.002.

[62] W. Wang, M. Tong, and M. Yu, "Blood Glucose Prediction with VMD and LSTM Optimized by Improved Particle Swarm Optimization," *IEEE Access*, vol. 8, pp. 217908–217916, 2020, doi: 10.1109/ACCESS.2020.3041355.

[63] K. Li, J. Daniels, C. Liu, P. Herrero, and P. Georgiou, "Convolutional Recurrent Neural Networks for Glucose Prediction," *IEEE J. Biomed. Health Inform.*, vol. 24, no. 2, pp. 603–613, 2020, doi: 10.1109/JBHI.2019.2908488.

[64] M. Jaloli and M. Cescon, "Long-Term Prediction of Blood Glucose Levels in Type 1 Diabetes Using a CNN-LSTM-Based Deep Neural Network," *J. Diabetes Sci. Technol.*, vol. 17, no. 6, pp. 1590–1601, Nov. 2023, doi: 10.1177/19322968221092785.

[65] R. I. Alkanhel *et al.*, "Hybrid CNN-GRU Model for Real-Time Blood Glucose Forecasting: Enhancing IoT-Based Diabetes Management with AI," *Sensors*, vol. 24, no. 23, Dec. 2024, doi: 10.3390/s24237670.

[66] V. B. Liu, L. Y. Sue, O. M. Padilla, and Y. Wu, "Optimizing blood glucose predictions in type 1 diabetes patients using a stacking ensemble approach," *Endocrine and Metabolic Science*, vol. 18, Jun. 2025, doi: 10.1016/j.endmts.2025.100253.

[67] A. Della Cioppa, I. De Falco, T. Koutny, U. Scafuri, M. Ubl, and E. Tarantino, "Reducing high-risk glucose forecasting errors by evolving interpretable models for Type 1 diabetes," *Appl. Soft Comput.*, vol. 134, Feb. 2023, doi: 10.1016/j.asoc.2023.110012.

[68] S.-M. Lee, D.-Y. Kim, and J. Woo, "Glucose Transformer: Forecasting Glucose Level and Events of Hyperglycemia and Hypoglycemia," *IEEE J. Biomed. Health Inform.*, vol. 27, no. 3, pp. 1600–1611, Mar. 2023, doi: 10.1109/JBHI.2023.3236822.

[69] M. A. Karagoz, M. D. Breton, and A. El Fathi, "A Comparative study of transformer-based models for multi-horizon blood glucose prediction," in *IFAC-PapersOnLine*, Elsevier B.V., May 2025, pp. 83–88. doi: 10.1016/j.ifacol.2025.06.027.

[70] P. Domanski, A. Ray, K. Lafata, F. Firouzi, K. Chakrabarty, and D. Pflüger, "Advancing blood glucose prediction with neural architecture search and deep reinforcement learning for type 1 diabetics," *Biocybern. Biomed. Eng.*, vol. 44, no. 3, pp. 481–500, Jul. 2024, doi: 10.1016/j.bbe.2024.07.006.

[71] Y. Shen and S. Kleinberg, "Personalized Blood Glucose Forecasting From Limited CGM Data Using Incrementally Retrained LSTM," *IEEE Trans. Biomed. Eng.*, vol. 72, no. 4, pp. 1266–1277, Apr. 2025, doi: 10.1109/TBME.2024.3494732.

[72] H. Nemat, H. Khadem, J. Elliott, and M. Benaissa, "Data-driven blood glucose level prediction in type 1 diabetes: a comprehensive comparative analysis," *Sci. Rep.*, vol. 14, no. 1, Dec. 2024, doi: 10.1038/s41598-024-70277-x.

[73] A. Neumann, Y. Zghal, M. A. Cremona, A. Hajji, M. Morin, and M. Rekik, "A data-driven personalized approach to predict blood glucose levels in type-1 diabetes patients exercising in free-living conditions," *Comput. Biol. Med.*, vol. 190, May 2025, doi: 10.1016/j.compbiomed.2025.110015.

[74] F. J. Lara-Abelenda, D. Chushig-Muzo, P. Peiro-Corbacho, A. M. Wägner, C. Granja, and C. Soguero-Ruiz, "Personalized glucose forecasting for people with type 1 diabetes using large language models," *Comput. Methods Programs Biomed.*, vol. 265, Jun. 2025, doi: 10.1016/j.cmpb.2025.108737.

[75] D. C. Klonoff *et al.*, "A Glycemia Risk Index (GRI) of Hypoglycemia and Hyperglycemia for Continuous Glucose Monitoring Validated by Clinician Ratings," *J. Diabetes Sci. Technol.*, vol. 17, no. 5, pp. 1226–1242, Sep. 2023, doi: 10.1177/19322968221085273.

[76] S. J. Moon, I. Jung, and C. Y. Park, "Current advances of artificial pancreas systems: A comprehensive review of the clinical evidence," Nov. 01, 2021, *Korean Diabetes Association*. doi: 10.4093/dmj.2021.0177.

[77] S. A. Brown *et al.*, "Multicenter trial of a tubeless, on-body automated insulin delivery system with customizable glycemic targets in pediatric and adult participants with type 1 diabetes," *Diabetes Care*, vol. 44, no. 7, pp. 1630–1640, 2021, doi: 10.2337/dc21-0172.

[78] G. P. Forlenza *et al.*, "Real-World Evidence of Omnipod® 5 Automated Insulin Delivery System Use in 69,902 People with Type 1 Diabetes," *Diabetes Technol. Ther.*, vol. 26, no. 8, pp. 514–525, Aug. 2024, doi: 10.1089/dia.2023.0578.

[79] J. L. Sherr *et al.*, "Safety and Glycemic Outcomes With a Tubeless Automated Insulin Delivery System in Very Young Children With Type 1 Diabetes: A Single-Arm Multicenter Clinical Trial," *Diabetes Care*, vol. 45, no. 8, pp. 1907–1910, Aug. 2022, doi: 10.2337/dc21-2359.

[80] R. Holt, C. Cockram, A. Flyvbjerg, and B. Goldstein, *Text book of Diadetes:forth edition*. 2010. doi: 10.1002/9781444324808.ch2.

[81] S. Schmidt and K. Norgaard, "Bolus calculators," *J. Diabetes Sci. Technol.*, vol. 8, no. 5, pp. 1035–1041, Jan. 2014, doi: 10.1177/1932296814532906.

[82] G. Stoet and R. I. Holt, "Characteristics of people with optimally-managed type 1 diabetes," *Diabetes Epidemiology and Management*, vol. 12, Oct. 2023, doi: 10.1016/j.deman.2023.100153.

[83] J. MacLeod, G. H. Im, M. Smith, and R. A. Vigersky, "Shining the Spotlight on Multiple Daily Insulin Therapy: Real-World Evidence of the InPen Smart Insulin Pen," *Diabetes Technol. Ther.*, vol. 26, no. 1, pp. 33–39, Jan. 2024, doi: 10.1089/dia.2023.0365.

[84] A. Mirzaee, M. Dehghani, and M. Mohammadi, "Optimal impulsive blood glucose control through multiple injections," *Chaos Solitons Fractals*, vol. 152, p. 111326, Nov. 2021, doi: 10.1016/j.chaos.2021.111326.

[85] G. Noaro, G. Cappon, M. Vettoretti, G. Sparacino, S. Del Favero, and A. Facchinetti, "Machine-Learning Based Model to Improve Insulin Bolus Calculation in Type 1 Diabetes Therapy," *IEEE Trans. Biomed. Eng.*, vol. 68, no. 1, pp. 247–255, Jan. 2021, doi: 10.1109/TBME.2020.3004031.

[86] J. Moreno-Fernandez, J. Sastre, P. Pinés, D. Calderon-Vicente, J. Gargallo, and J.-R. Muñoz-Rodriguez, "To evaluate the use and clinical effect of intermittently scanned continuous glucose monitoring in adults with type 1 diabetes: Results of a multicentre study," *Endocrinología, Diabetes y Nutrición (English ed.)*, vol. 70, no. 4, pp. 270–276, Apr. 2023, doi: 10.1016/j.endien.2023.03.013.

[87] T. R. Gilbert, A. Noar, O. Blalock, and W. H. Polonsky, "Change in Hemoglobin A1c and Quality of Life with Real-Time Continuous Glucose Monitoring Use by People with Insulin-Treated Diabetes in the Landmark Study," *Diabetes Technol. Ther.*, vol. 23, no. S1, p. S-35-S-39, Mar. 2021, doi: 10.1089/dia.2020.0666.

[88] R. W. Beck *et al.*, "Effect of initiating use of an insulin pump in adults with type 1 diabetes using multiple daily insulin injections and continuous glucose monitoring (DIAMOND): a multicentre, randomised controlled trial," *Lancet Diabetes Endocrinol.*, vol. 5, no. 9, pp. 700–708, Sep. 2017, doi: 10.1016/S2213-8587(17)30217-6.

[89] S. Gerber, G. P. S. Kwong, and J. Ho, "Assessment of insulin dose changes in pediatric patients with type 1 diabetes mellitus starting on continuous subcutaneous insulin infusion," *J. Clin. Transl. Endocrinol.*, vol. 37, Sep. 2024, doi: 10.1016/j.jcte.2024.100363.

[90] E. Putula, P. Hannula, H. Huhtala, and S. Metso, "Glycaemic control in insulin deficient patients using different insulin delivery and glucose sensoring devices: Cross-sectional real-life study," *Diabetes Epidemiology and Management*, vol. 7, Jul. 2022, doi: 10.1016/j.deman.2022.100072.

[91] F. León-Vargas, J. A. Arango Oviedo, and H. J. Luna Wandurraga, "Two Decades of Research in Artificial Pancreas: Insights from a Bibliometric Analysis," *J. Diabetes Sci. Technol.*, vol. 16, no. 2, pp. 434–445, Mar. 2022, doi: 10.1177/19322968211005500.

[92] J. Garcia-Tirado *et al.*, "Advanced Closed-Loop Control System Improves Postprandial Glycemic Control Compared With a Hybrid Closed-Loop System Following Unannounced Meal," *Diabetes Care*, vol. 44, no. 10, pp. 2379–2387, Oct. 2021, doi: 10.2337/DC21-0932.

[93] B. Matejko *et al.*, "Transitioning of People With Type 1 Diabetes From Multiple Daily Injections and Self-Monitoring of Blood Glucose Directly to MiniMed 780G Advanced Hybrid Closed-Loop System: A Two-Center, Randomized, Controlled Study," *Diabetes Care*, vol. 45, no. 11, pp. 2628–2635, Nov. 2022, doi: 10.2337/dc22-0470.

[94] B. Matejko *et al.*, "Excellence in the management of Advanced Hybrid Closed-Loop Systems: Lessons from the Polish cohort," *Diabetes Res. Clin. Pract.*, vol. 216, Oct. 2024, doi: 10.1016/j.diabres.2024.111832.

[95] C. J. Levy *et al.*, "Beneficial Effects of Control-IQ Automated Insulin Delivery in Basal-Bolus and Basal-Only Insulin Users With Type 2 Diabetes," *Clinical Diabetes*, vol. 42, no. 1, pp. 116–124, Jan. 2024, doi: 10.2337/cd23-0025.

[96] R. W. Beck *et al.*, "A Meta-Analysis of Randomized Trial Outcomes for the t:slim X2 Insulin Pump with Control-IQ Technology in Youth and Adults from Age 2 to 72," *Diabetes Technol. Ther.*, vol. 25, no. 5, pp. 329–342, May 2023, doi: 10.1089/dia.2022.0558.

[97] T. M. Peters and A. Haidar, "Dual-hormone artificial pancreas: benefits and limitations compared with single-hormone systems," *Diabetic Medicine*, vol. 35, no. 4, pp. 450–459, Apr. 2018, doi: 10.1111/dme.13581.

[98] E. Estremera, A. Beneyto, A. Cabrera, I. Contreras, and J. Vehí, "Intermittent closed-loop blood glucose control for people with type 1 diabetes on multiple daily injections," *Comput. Methods Programs Biomed.*, vol. 236, Jun. 2023, doi: 10.1016/j.cmpb.2023.107568.

[99] G. Papa, R. Cannarella, R. A. Condorelli, C. Finocchiaro, A. E. Calogero, and S. La Vignera, "Glycometabolic outcomes in adult type 1 diabetic patients switching to closed-loop systems," *Diabetes Res. Clin. Pract.*, vol. 204, Oct. 2023, doi: 10.1016/j.diabres.2023.110907.

[100] S. Barkhordari, S. S. Samandari, M. Abdouss, and M. Pourmadadi, "Recent advances and perspectives in novel insulin release systems," *J. Drug Deliv. Sci. Technol.*, vol. 104, p. 106500, Feb. 2025, doi: 10.1016/J.JDDST.2024.106500.

[101] D. Dermawan and M. A. Kenichi Purbayanto, "An overview of advancements in closed-loop artificial pancreas system," Nov. 01, 2022, *Elsevier Ltd*. doi: 10.1016/j.heliyon.2022.e11648.

[102] A. K. Singh and D. Koundal, "A Temporal Convolutional Network for modeling raw 3D sequences and air-writing recognition," *Decision Analytics Journal*, vol. 10, Mar. 2024, doi: 10.1016/j.dajour.2023.100373.

[103] H. P. Vinutha, B. Poornima, and B. M. Sagar, "Detection of outliers using interquartile range technique from intrusion dataset," *Advances in Intelligent Systems and Computing*, vol. 701, pp. 511–518, 2018, doi: 10.1007/978-981-10-7563-6_53.

[104] K. Benkert, E. Gabriel, and M. M. Resch, "Outlier detection in performance data of parallel applications," *IPDPS Miami 2008 - Proceedings of the 22nd IEEE International Parallel and Distributed Processing Symposium, Program and CD-ROM*, 2008, doi: 10.1109/IPDPS.2008.4536463.

[105] T. Dave, M. Joshi, and U. Pandya, "Distributed Model Architecture for Cuff-Less Blood Pressure Measurement System," *SN Comput. Sci.*, vol. 3, no. 6, p. 503, Oct. 2022, doi: 10.1007/s42979-022-01391-8.

[106] W. L. Clarke, D. Cox, L. A. Gonder-Frederick, W. Carter, and S. L. Pohl, "Evaluating clinical accuracy of systems for self-monitoring of blood glucose," *Diabetes Care*, vol. 10, no. 5, pp. 622–628, 1987, doi: 10.2337/diacare.10.5.622.

[107] D. M. Chiara, F. Micheletto, D. Lv, M. Breton, B. Kovatchev, and C. Cobelli, "The UVA/PADOVA type 1 diabetes simulator: New features," *J. Diabetes Sci. Technol.*, vol. 8, no. 1, pp. 26–34, 2014, doi: 10.1177/1932296813514502.

[108] R. Visentin *et al.*, "The UVA/Padova Type 1 Diabetes Simulator Goes From Single Meal to Single Day," *J. Diabetes Sci. Technol.*, vol. 12, no. 2, pp. 273–281, Mar. 2018, doi: 10.1177/1932296818757747.

[109] M. Cindy and B. Razvan, "The ohioT1DM dataset for blood glucose level prediction: Update 2020," *CEUR Workshop Proc.*, vol. 2675, pp. 71–74, 2020, [Online]. Available: http://smarthealth.cs.ohio.edu/bglp/OhioT1DM-dataset-paper.pdf

[110] A. S. Brazeau *et al.*, "Carbohydrate counting accuracy and blood glucose variability in adults with type 1 diabetes," *Diabetes Res. Clin. Pract.*, vol. 99, no. 1, pp. 19–23, Jan. 2013, doi: 10.1016/j.diabres.2012.10.024.

[111] C. Xu, X. Wang, and S. Zhang, "Dilated convolution capsule network for apple leaf disease identification," *Front. Plant Sci.*, vol. 13, Nov. 2022, doi: 10.3389/fpls.2022.1002312.

[112] Al. Alessandro, P. Irene, T. Stefano, P. Enrico, and A. Andrea, "A Multi-Patient Data-Driven Approach to Blood Glucose Prediction," *IEEE Access*, vol. 7, pp. 69311–69325, 2019, doi: 10.1109/ACCESS.2019.2919184.

[113] W. Clarke and B. Kovatchev, "Statistical Tools to Analyze Continuous Glucose Monitor Data," *Dabetes Technology & Therapeutics*, vol. 11, pp. 45–53, Sep. 2009, doi: 10.1089/dia.2008.0138.

[114] B. P. Kovatchev, M. Straume, D. J. Cox, and L. S. Farhy, "Risk analysis of blood glucose data: A quantitative approach to optimizing the control of Insulin Dependent Diabetes," *Journal of Theoretical Medicine*, vol. 3, no. 1, pp. 1–10, Jan. 2000, doi: 10.1080/10273660008833060.

[115] B. P. Kovatchev, E. Otto, D. Cox, L. Gonder-Frederick, and W. Clarke, "Evaluation of a new measure of blood glucose variability in diabetes," *Diabetes Care*, vol. 29, no. 11, pp. 2433–2438, Nov. 2006, doi: 10.2337/dc06-1085.

[116] L. Magni *et al.*, "Evaluating the Efficacy of Closed-Loop Glucose Regulation via Control-Variability Grid Analysis," *J. Diabetes Sci. Technol.*, vol. 2, no. 4, pp. 630–635, Jul. 2008, doi: 10.1177/193229680800200414.

List of Publications

[1] **Ketan Lad**, Maulin Joshi, and Amit Joshi, "Optical Sensor Based Continuous Blood Glucose Estimation Using Lightweight Distributed Architecture," SN Computer Science, vol. 5, no. 8, Dec. 2024, https://doi.org/10.1007/s42979-024-03318-x.

[2] **Ketan Lad** and Maulin Joshi, "DCRNet: Hybrid Deep Learning Architecture for Forecasting of Blood Glucose," Journal of Electronics, Electromedical Engineering, and Medical Informatics, vol. 8, no. 1, pp. 53–68, Dec. 2025, https://doi.org/10.35882/jeeemi.v8i1.1245.

[3] **Ketan Lad** and Maulin Joshi (2023). Continuous Blood Glucose Monitoring Using Explainable AI Techniques. In M. S. Raval, M. Roy, T. Kaya, & R. Kapdi (Eds.), Explainable AI in Healthcare. Chapman and Hall/CRC. https://doi.org/10.1201/9781003333425.

[4] **Ketan Lad** and Maulin Joshi, "An intermittent insulin bolus therapy for improvement of personalized Type 1 diabetes management". (Manuscript is under review)

Annexure A

Sample Consent and data collection form

Svaarogyam	CONSENT FORM	Date: 24.08.2022
		Approved by: R&D Team Version: 1

Consent Form

Thank you for your interest in participating in our research and development work to create a non-invasive glucometer. We are a registered startup based in Jaipur called Svaarogyam Medical Devices supported, funded by DST Nidhi Prayas and MIIC, MNIT Jaipur. Please read through this consent form and sign your name at the bottom if you agree to participate in the research and development work.

Voluntary participation:
Participation in this research is voluntary. You can withdraw your consent to participate at any time.

Information collection and usage:
We will take notes and record **your age, weight, HbA1C, Diabetes type (Type1/ Type 2/ Gestational/ Auto-immune), duration of diabetes, insulin dosage, glucose values, patient history, height, cholesterol/blood pressure/heart disease/other diseases, family history, smoking/alcohol/sleeplessness and physical activity.** This shall be done along with your serum glucose reading. Recordings are kept confidential and will not be shared outside of our research team. However, your name and other personal identification information will remain anonymous unless explicit permission is received beforehand.

Should you have any questions about the details of this research, please contact **us** at **svaarogyam@gmail.com.**

Consent:
By signing this document, you agree that you have read and understood the information provided above and you give your consent to participate in this research study.

Participant's Name _____

Participant's Signature: _____

Date _____

Svaarogyam Medical Devices, MIIC, MNIT Campus, Jaipur, Rajasthan-302017
✆+91-9549654259 ✉ svaarogyam@gmail.com

Data collection form for research for Diabetic

*The purpose of this data collection is to analyse the different parameters which affect the blood glucose level in diabetic people. This data will be used only for research. No personal information of patient will be revealed in this research at any stage.

Patient ID: **Date:**

Gender (tick applicable)	1) Male	2) Female		
Age (years)				
Weight (Kgs)				
Height (cm)				
Fasting Blood glucose (before breakfast)				
Postprandial plasma glucose (2 hours after eating)				
BG level				
Insulin bolus dosage (if any)				
Medicine to control BG level				
Meal (Carbohydrate)				
Blood pressure:	Systolic:		Diastolic:	
Cholesterol:	HDL:		LDL:	
Body temperature				
SPo2				
Duration of diabetes (years)				
Heart rate				
History of diabetes in family	a) father	b) mother	c) father heredity	d) mother heredity
Sleep time				
Sleep quality				
Smoking habit	a) current	b) former	c) no habit	

Alcohol consumption	a) regularly	b) occasionally	c) no
Walking	step count_____ time: _____		
Daily Physical Exercise	a) regular Duration:_____minutes	b) irregular	
Other diseases			

Researchers:	**Venue:**
Prof. Ketan K. Lad Research Scholar, Gujarat Technological University, Chandkheda, Ahmedabad	Dr. Anish Diwanji Shreenath clinical laboratory, A-115, Aditya chambers, station road, Valsad, Gujarat-396001

Patient Name:

Signature